Development of Biomimetic Functional Materials by Wettability Control

August 2017

TENJIMBAYASHI, Mizuki

A Thesis for the Degree of Ph.D. in Engineering

Development of Biomimetic Functional Materials by Wettability Control

August 2017

Graduate School of Science and Technology
Keio University

TENJIMBAYASHI, Mizuki

Development of Biomimetic Functional Materials by Wettability Control

by TENJIMBAYASHI, Mizuki

Abstract

There is a long history of obtaining inspiration from nature for the design of purposeful materials and systems. With recent advances in nanotechnology, biomimicry has been gaining increasing attention as a way to achieve such multifunctional materials. Bioinspired techniques for the control of surface wettability especially have potential applications ranging from industrial coatings to biomedical materials. For instance, the outstanding properties of the lotus leaf, moth eye, spider web, legs of water striders, gecko, cactus spine, and desert beetle offer remarkably effective ways to design functional materials with special wettability for self-cleaning, anti-fouling, biofouling resistance surface, anti-icing coating, oil purification, and microfluidic systems. The advancement of these types of biomimetic materials with special types of wettability relies on discoveries of new mechanisms, advances in processing, and/or adding multifunctionality such as transparency and durability for practical use.

In this work, bioinspired functional materials are designed for the control of surface wettability. Each chapter in this thesis is structured by first overviewing previous studies which investigate how natural systems achieve function, and then biomimetic materials specifically replicating those functions are designed and developed.

Lotus leaves provided inspiration for the design of functional anti-wetting materials: highly mechanically durable superhydrophobic coating, and potassium ion sensor in blood with anti-blood adhesion properties. Spider's webs offered the idea of designing a self-supporting nanofiber sheet with selective wettability of hydrophobicity and oleophilicity at the same time for versatile oil-water separation. Inspired by the pitcher plant, which has a "slippery" wetting surface: a surface with π interaction based liquid adsorption, smoothness and hydrophobicity (SPLASH) is proposed as an anti-fouling surface with transparency and mechanical durability. Finally, inspired by the anisotropic wetting properties of cactus spines, hydrophobic patterned surfaces with different liquid adhesion properties were designed to control droplet motion. This technique was then applied to micro-fluidic devices. These efforts to develop biomimetic functional materials with controlled wettability can help future scientific development and expand into new industrial applications.

Acknowledgements

This work is supported by many people and funding. Firstly, I would like to express my sincere gratitude to my supervisor Prof. Shiratori for the continuous support of my Ph.D. study and related research, for his passion and extensive knowledge. His guidance helped me in all the time of research and motivated me of studying in Ph.D. course. I’m sure that he has been the best advisor and mentor for my Ph.D. study.

I sincerely thank Prof. Citterio, Prof. Imai, and Prof. Asakura for their peer reviewing and valuable comments to this study.

I gratefully acknowledge Prof. Ariga and the members in International Center for Materials Nanoarchitectonics (MANA), National Institute for Materials Science (NIMS) for their kind support to my study and daily life.

My Ph.D. study was supported by predoctoral fellowship (DC1) from Japan Society of Promotion of Science (JSPS) and funded by JSPS KAKENHI JP16J06070.

I’m deeply grateful to my essential members in Prof. Shiratori laboratory for their kind help and daily life. The Ph.D. life in this laboratory is my precious memory thanks to them.

Finally, I would like to express my great appreciation to my family for their love and support.

Table of Contents

Appendix

List of Figures

KCl added, blood with 5 mM KCl added, and blood with 10 mM KCl added. (B) Response curve of blood with potassium addition for the standard addition method.

Figure 2-17. Color value change with potassium addition to human blood obtained by *in-situ* measurement using color difference meter. Linear response was obtained for the potassium ion determination as well as the response by UV-vis spectra.

Figure 3-1. Schematic illustration of strategy for enhancing selective wettability. The control of surface-liquid interaction and surface roughness can contact liquid A with *Cassie-Baxter* state and liquid B with *Wenzel* state at the same time.

Figure 3-2. Schematic illustration of liquid wetting behaviors on a porous material. (A) Liquid fail to penetrate into the porous material with the robustness factor $A^{*} \gg 1$. Here, *R* is a cylinder radius and 2D is an inter-cylinder space. (B) Liquid penetrate the porous material with $A^{*} \leq 1$. (C) Liquid I fail to penetrate the porous material due to the existence of liquid II with *Young-Laplace* pressure $\Delta p > 0$. Here, R' is a radius of a curvature of liquid I at inter-cylinder space.

Figure 3-3. Biomimetics of *Uloborus walckenaerius* spider web to design an attachable self-standing NF-S. (A) Schematic image of the predation mechanism of *Uloborus walckenaerius*. (B) Photo-image and (C) SEM image of an attachable self-standing NF-S. (D) Attachment of a NF-S to a Kimtowel and (E) its magnified image. (F, G) Attachment of a NF-S block to (F) a finger and (G) an insect.

Figure 3-4. Schematic images of the designing procedure. i. The design of the NF-S using an electrospinning method. ii. Peeling the NFs-S from the aluminum foil, which allows the NF-S to become self-standing and negatively charged. iii. The self-standing NF-S was attached to a melamine sponge for oil absorption, to the tip of PVC tube for oil-water separation by filtration, and to a container for oil collection.

Figure 3-5. Cross-sectional SEM images of the NF-S. The thickness of the NF-S is 135 μm.

Figure 3-6. (A) The NF-S strength and elastic properties. (B) Distribution of fiber diameter in the NF-S. (C) BET fit for the N_2 adsorption isotherm of the NF-S.

Figure 3-7. (A) Elemental composition and (B) elemental distribution of carbon, nitrogen, oxygen, fluorine, and overall distribution of the NF-S.

Figure 3-8. Wetting behaviors of water and oils on the NF-S. (A) Schematic illustrations of a water droplet on: (i) the NF-S; (ii) a toluene-infused NF-S; and (iii) hexadecane-infused NF-S; and (iv) a toluene droplet and (v) a hexadecane droplet on the NF-S. (B) Water contact angle on (i)-(iii). (C) Oil contact angles of (iv) and (v). (D) The contact angles and surface tensions (20 °C) for an ethanol-water mixture. [42] The limit for wetting or repelling is at a surface tension in the range of 36.09-38.56 mN m^{-1}.

Figure 3-9. Dynamic wetting behaviors water and oil on the NF-S. (A) Time-lapsed images (i)-(iv) and (B)-(D) selected magnified images.

Figure 3-10. Application of the NF-S to oil absorbent. (A) A photo-image of an uncoated melamine sponge (sponge) and the NF-S attached melamine sponge (sponge + NF-S) with a schematic image of the magnified oil absorbents. (B) A photo-image of the samples in a beaker half-fulfilled with dyed water. (C) Photo-images of the sponge + NF-S being used in separating oil in processes (i)-(iii). (D) Mass change of toluene inside the sponge with cycles of absorption and squeezing. (E) Absorption capacities for the oil-water mixtures with different types of oil. (F) Cyclical pressing measurements for the sponge + NF-S.

Figure 3-11. Dynamic wetting behaviors water and oil on the NF-S. (A) Time-lapsed images (i)-(iv) and (B)-(D) selected magnified images.

Figure 3-12. Application of 2D oil-water separation. (A) Oil-water separation filter. Photo-images show the separation of toluene from the toluene-water mixture in processes (i)-(iii). (B) A photo-image of toluene and water after separation. (C) Separation efficiency and (D) separation flux of oil-water mixtures with different types of oil. (E, F) Separation flux of the toluene-water mixture with different NF-S thicknesses (E) and pore diameters (F) adjusted by folding and extending the NF-S. (G, H) Photo-images and (I, J) microscopic images of the emulsified toluene-water mixture before (G, I) and after separation (H, J).

Figure 3-13. Application of an oil collector. Photo-images of toluene collection in a container from a toluene-water mixture in processes (i)-(iii).

Figure 3-14. Effect of PVDF-HFP: Et-CA ratio on (A) extension ratio, (B) water contact angle, and (C, D) fiber diameter with the SEM images (D). (E) Atomic ratio of fluorine per nitrogen for each ratio of PVDF-HFP with Et-CA. (F) Elemental distribution of fluorine and nitrogen in the fibers with respect to the ratio of PVDF-HFP to Et-CA.

Figure 3-15. Electrospinning device for large-scale fabrication of NF-Ss. The slider moves in the direction of the arrow and the drum roller rotates to design uniform and large-scale NF-Ss

Figure 4-1. Schematic illustrations showing the fabrication of a SLIPS reproduced with permission. Copyright 2011, Nature Publishing Group [1].

Figure 4-2. Schematic illustration which explains criteria for thermodynamically stable SLIPS formation. When configuration 1, and 2 are more stable than configuration A, SLIPS is stably let liquid A slide on the surface.

Figure 4-3. Wide-range x-ray photoelectron spectroscopy (XPS) analysis of the SiO_2-Ph and SiO_2-C_{10} showing the O_{1s}, C_{1s}, and Si_{2p} spectra employing an MgKα laser.

Figure 4-4. AFM images of (A) SiO_2-Ph and (B) SiO_2-C_{10} coated glass substrate.

Figure 4-5. (A) Photographic images of various liquids dropped on the surface of SiO_2–Ph or SiO_2–C_{10}. These liquids are castedusing micropipette (10 μL). (B) Check of LL wetting on SiO_2–Ph compared with SiO_2–C_{10} (without π electrons). Sliding angle (SA) of various liquids measured on each surface. These liquids are casted on the surface using micropipette (10 μL). When the test liquid is adsorbed, the liquid does not slide. (C) Static contact angle (SCA) of various liquids measured on each surface.

Figure 4-6. (A) Preparation procedure of the patternable LL formation. Patterned mask substrate (green) (1) is modified with SiO_2–C_{10} (red) to give (2). SiO_2–Ph precursor solution is then cast on the surface after the mask is removed (3) and the SiO_2–C_{10} area (blue) repels this liquid (4) to give the patterned surface (5). Dyed acetone as LL is cast on the patterned surface. (B) LL is formed in the shape of KEIO the scale bar is 10 mm. (C) Preparation procedure of the programmed LL transportation. Movement of LL on the patterned surface by the pinning effect. (1) SiO_2–C_{10} precursor solution (blue) is cast on the substrate and the (2) SiO_2–Ph precursor solution (red) is cast using a micropipette during the SiO_2–C_{10} modification to program the way to transport (3). The LL (dyed acetone in this case) navigates along the blue dots by Marangoni F_m with gravity F_g forces, resulting movement of a LL droplet on the programmed surface. (D) The LL slides along the direction of the blue dotted arrow.

Figure 4-7. π-interacted liquid wetting analysis. (A) CH-π interactions between decyltrimethoxysilane (DTMS) as LL and SiO_2–Ph as BL. (B, C) Time-lapsed DTMS (10 μL) wetting behaviour on (B) SiO_2–C_{10} and (C) SiO_2–Ph. The scale bar is 5 mm. Because of the CH/pi interaction between LL and SiO_2-Ph BL, DTMS showed the extreme superoleophilicity (static contact angle SCA<1°) on SiO_2–Ph coated glass (25 mm × 25 mm) after 30 s. (D) Spreading width W of DTMS droplet wetting on SiO_2–Ph (Red) and SiO_2–C_{10} (Blue) per time t. (E) Approximation of droplet spreading with the law of $W^2(W^4-W_{impact}^4) \sim \gamma_L \cos\theta_{adv}(\tau-\tau_{impact})$.

Figure 4-8. π-interacted liquid wetting analysis on different 3 functionalized smooth surfaces. (A) Images of LL wetting behaviour on the BLs of SiO_2-OH, SiO_2-C_{10}, and SiO_2-Ph. (B)-(D) The wetting behaviour of water droplet on DTMS cast BLs of (B), SiO_2-OH, (C), SiO_2-C_{10}, (D), and SiO_2-Ph.

Figure 4-9. Photo image and schematic illustration showing the condition of water droplet casting on smooth BL with PFPE LL.

Figure 4-10. (A) Schematic illustration of procedure for designing SPLASH, and (B) Check of LL (DTMS) thickness formed on smooth base layer with shearing stress by a spin coater.

Figure 4-11. Hydrophobicity of the SPLASH. (A) Static contact angle (SCA) and (B) sliding angle of water droplet on each layered coating. Their values change after attaching SiO_2-Ph as the BL and DTMS as the LL. (C, D) Wetting image of (C) advancing contact angle (θ_{adv}) and (D) receding contact angle (θ_{rec}) measurement of water droplet. The calculated contact angle hysteresis ($\Delta\theta$) was 0.75°, that is extremely low values realized by fluidity of LL not resisted by the roughness of BL. (E) Photo-images of self-cleaning procedure of the SPLASH. Sands covering the SPLASH are cleaned by water droplet. (F) Various liquids with high temperature, chemical complexity, different states, and biomedia sliding on the SPLASH tilting 15°. (G) Images of glass (left) and coated glass (right) after dipping in blood. (H) High-speed camera images of ice cream, which is a complex with water/salt and solid/liquid, on BL+LL tilting 15°. (I) Various fluidic foods (soy sauce, ketchup, honey, coffee, mayonnaise, curry, carbonara sauce) slide on a SPLASH when a LL of silicone oil KF-54 is chosen. Soy sauce, ketchup, honey, coffee, mayonnaise, curry and carbonara sauce from supermarket.

Figure 4-12. Time-lapsed images that compare water sliding behavior on rough BL+DTMS and smooth BL+DTMS.

Figure 4-13. An analysis of water droplet sliding behaviour on the SPLASH. (A) The sliding length L of various volume water droplet per time τ on the SPLASH tilting 6° following the linear approximation with the law of $L = v\tau$ $(\tau < 1)$. (B) The sliding velocities v of various volume V of water droplet on the SPLASH tilting 6°. This graph revealed even 1 μL of water droplet slides on the SPLASH. (C, D) Photo images of (C) control and compared to (D) the SPLASH after misty water spraying test. Misty water was sprayed several times to them with same conditions. The scale bars are 20 mm. (E-H) Magnified images and schemes of water mist sprayed several times on the SPLASH tilting 75°. The water droplets circled in yellow coalescence into the droplet circled in red in an interval of 20 ms. The misty water droplets were removed by two steps of (E, F) and (G, H) process. (E, F) Microsized water droplets (yellow circles) coalesce into the large droplet and then the droplet slides (red circle). (G, H) Large water droplet moves absorbing microdroplets. The blue dotted area is the passage of the large droplet. No droplets remain in the blue dotted area.

Figure 4-14. Optical properties of the hydrophobic-liquid-adsorbed smooth surface. (A–D) Transparency of the SPLASH. (A) Photograph of the BL-coated glass substrate and (B) photograph of dyed water sliding on the BL with LL coating. (C) Total transmittance (TT), parallel transmittance (PT), haze (HAZE), and diffusion (DIF) of each surface. PT means the degree that light passes through a sample within a small range of angles (<15°). The HAZE value is given by haze (%) = DIF/TT × 100. (D) Solar cell application of the

SPLASH. Photocurrent density (J_{sc}) versus voltage (V_{oc}) for solar cells tilting 30°, one covered with a glass substrate, and one covered with SPLASH. Inserted table is a summary of the photovoltaic performance of solar cells under various conditions. (E-H) Assessment of the optical properties with the smooth BL [the same coating as the BL in (C)] and rough BL with DTMS as the LL. (E, F) The SEM images of smooth BL (E, the scale bar is 10 μm) and rough BL (F, the scale bar is 0.5 μm) by self-assembly of SiO_2 nanoparticles. (G), Optical values of PT and DIF for the smooth BL, smooth BL with LL, smooth BL with LL with time (30 min) to decrease LL thickness, rough BL, rough BL with LL, and rough BL with LL with time. (H), Schematic illustrations of the surface scattering change in the surface structure on the smooth BL and the rough BL with LL thickness. Smooth BL with LL shows stable transmittance with LL decrease whereas rough BL with LL increase light scattering with LL decrease.

Figure 4-15. Assessment of SPLASH stability. (A) Sliding angle of deionized water after adding shearing stress from 0 to 6000 rpm by a spin coater for 30 s. (B) Long-term storage of glass slides covered with the SPLASH under air conditions (20°C, blue dots) and under water (red dots). Even though DTMS can possibly react on water or evaporate under air condition, the 0.08 $\mu L\ cm^{-2}$ of DTMS casted SiO_2–Ph on glass slides (25 mm × 25 mm) kept the sliding angle low (<5°) for about 2 weeks under both conditions. Although the sliding angle decreased after long time, re-cast of LL have regenerated the sliding property. (C) Stability of the SPLASH against various pH conditions of water droplet ranging from 1.82 to 13.88. The sliding properties was stable in pH conditions ranging 1.82-13.06. In the case of pH 13.88, the water droplet was soaked into the SPLASH. (D-F) Flexibility of the SPLASH coated on PET film. (D) Photographs of the flexible SPLASH and (E) Schematic illustrations of water slides on the bent surface. Even though the thickness of the LL decrease, the hydrophobicity of the SPLASH does not change. That’s because of the smoothness of the BL. (F) Quantification of the flexible SPLASH hydrophobic property by changing the ratio of H/L. (G, H) Self-healing property of SPLASH. (G) Photographs of the cut SPLASH maintaining the hydrophobicity and (H) schematic illustrations showing why the SPLASH retains the hydrophobicity after cutting. (I, J) Mechanical durability against cotton abrasion. (I) Photographs of the SPLASH after cotton abrasion showing that the hydrophobicity is retained and (J) schematic illustrations showing why the SPLASH retains the hydrophobicity after cotton abrasion.

Figure 5-1. Schematic illustration of anisotropic wetting approaches. (A) surface chemistry driven force ($F_{\mathrm{chemistry}}$) and (B) morphology driven force ($F_{\mathrm{morphology}}$) work toward droplets on surfaces, respectively. The scheme is reproduced with the permissions. Copyright 2015, American Chemical Society [11].

Figure 5-2. Schematic illustration of droplet motion is restricted by (A) morphological or (B) chemical heterogeneity of the surface. (A) When a droplet comes on the slope surface, it cannot wet the slope area until its advancing contact angle gets larger than sum of slope angle and static contact angle. (B) When a droplet comes on the surface 1, it cannot wet the surface 2 till its advancing contact angle on the surface 1 becomes higher than its static contact angle on the surface 2.

Figure 5-3. Schematic illustration of 'omniphobicity'-based patterning to obtain an anisotropic wetting surface.

Figure 5-4. (A) Schematic images of the C_{10}/Ph patterned surface. The height gap is thought to be controlled by the surface energies of the precursor solution and omniphobic area. (B) Thickness of the C_{10} and Ph coating on the C_{10}/Ph patterned surface using a Dektak profilometer over a scanning area of 0.5 mm employing 3000 plots per modified area. (C) Surface uniformity and height distribution measured by Laser microscopy.

Figure 5-5. (A) Dynamic contact angles (DCAs) and sliding angles (SAs) of 10 μL water droplets with photographic images. These values were measured by a tilted plate method together with resistance force for a moving contact line. (B) Water SA on a 2 mm wide Ph- tethered path (yellow line in scheme) and C_{10}- tethered remaining area, rotating the sliding direction from 0–90°. When the rotating angle (φ) is 0° (or 90°), droplet transportation on the Ph- tethered path follows a parallel (or perpendicular) direction. (C) Droplet motion control on Ph-/C_{10}- patterned surface. (D) Photo image of a 20 μL water droplet on a Ph-/C_{10}- patterned surface measured using a digital microscope.

Figure 5-6. Change to the water droplet mass as a function of transportation time measured using an electronic balance with 0.1 mg accuracy at 28.3 °C, 49% relative humidity.

Figure 5-7. Total force, F_{total}, analysis between the water droplet and the C_{10}- and Ph- tethered border area (see scheme in (A)). (B) graph showing total liquid droplet force as a function of volume when the head of a droplet overlaps, dx, on the border oriented perpendicular to the trajectory tilting at 24° with photographic images in (C). When V is greater (less) than 80 μL as in (D), F_{total} on the border becomes positive (negative) and the droplets larger than 80 μL overlap beyond the border as in (E), whereas droplet sizes under this threshold level stop on the border. (F)-(I) Driven force analysis between the water droplet and the C_{10}- and Ph- tethered border area as a function of liquid droplet volume when a tip of a droplet overlaps, dx, on the border oriented perpendicular to the trajectory tilting at 24°.

Figure 5-8. (A) Study of various volume water droplet sliding on patterned surfaces with the width of the Ph- tethered area ranging between 1–3 mm. When the volume of the droplet is <40 μL, the SA of the micro-droplet can be controlled by the width of the Ph-tethered area. (B) Reaction procedure on V shape patterned surfaces. Based on its volume, a reactant is transported in a downward motion, is captured, and not until coalescing with another reactant is the downward motion continued under the conditions of: V_1, $V_2 < V_{critical}$ and $V_1 + V_2 > V_{critical}$. (C-D) Time-elapsed photo images of a micro-reactor application under acidic and basic conditions: (C) Bromophenol blue (BPB) protonation by hydrochloric acid aqueous solution with a pH value of 2.13 (V = 25 μL, TA = 40°, φ = 18°, path width = 1 mm (right), 2 mm (left)) and (D) Thymol blue (TB) deprotonation by sodium hydroxide aqueous solution with a pH value of 13.06 (V = 35 μL, TA = 60°, φ = 18°, path width = 1 mm (right), 2 mm (left)). (E-F) Surface durability under acidic or basic conditions of the (E) C_{10}- and (F) Ph- tethered area. SAs of 10 μL aqueous droplets as a function of pH are measured on each surface after contacting for 0, 1 or 60 minutes. When the surfaces are applied to a micro-reactor, the liquid-solid contact time must be <1 min. Thus, the surfaces are sufficiently durable for the application.

Figure 5-9. (A) EDX spectra and (B) Elemental contamination presented by normalized atomic ratios of a dynamically hydrophobic patterned surface (blue) and a dynamically hydrophilic surface (-OH tethered surface, red) after casting aqueous droplets of BPB (i), TB (ii), HCl (iii) and NaOH (iv), respectively. Because of the volatility of aqueous HCl, the chloride peaks were not observed after aqueous HCl contamination. Although sodium peaks were observed on both surfaces, the peaks were derived from Na_2O in the substrate.

Figure 5-10. (A) Wide-range x-ray photoelectron spectroscopy (XPS) analysis of the C_6-coatings showing the O_{1s}, C_{1s}, and Si_{2p} spectra employing an MgKα laser (see **Figure 4-2** in Chapter 4 for XPS analysis of the Ph-, C_{10}- area). (B) FTIR attenuated total reflection spectra of C_{10} (blue), C_6 (Black), and Ph (red) modified Si-wafer surfaces. The peak shifts * and ** (circled yellow) are based on the C_{10} spectra.

Figure 5-11. Solvent droplets motion control. (A-D) Dynamic contact angles and (E-H) static CAs of various liquids on various functional tethered smooth surfaces. Based on this study, we adapted C_6-/C_{10}- patterning for solvent manipulation. (I–K) Time-elapsed photo images of omniphobic liquid manipulation by replacing the Ph- tethered area with a C_6- tethered area to realize diagonal sliding of (I) acetone, (J) toluene, and (K) hexadecane (V = 10 μL, TA = 8°, φ = 20°, path width = 1 mm).

Figure 5-12. SAs of 10 μL aqueous droplets as a function of aqueous liquid viscosity adjusted by mixing sodium alginate with water.

Figure 5-13. Optical analysis of (A) uncoated area, (B) C_{10}- tethered area, (C) Ph-tethered area, and (D) the interfacial border on the patterned smooth surface measured by total transmittance (TT), parallel transmittance (PT), haze (HAZE), and diffusion (DIF).

PT means the degree of light that passes through a sample within a small angle range (<15°). The HAZE value is given by haze (%) = DIF/TT × 100.

Figure 5-14. (A) Mechanical durability analysis measured by abrasion time versus SA of a 10 μL water droplet. (B-C) Flexibility of the patterned smooth surface coated on a polyethylene terephthalate (PET) film. (B) Quantification of bending resistance measured by bending times versus SA of a 10 μL water droplet. (C) Photographic images indicating that the water droplet can diagonally slide on the bent patterned smooth surface while the water droplet can perpendicularly slide on the C_{10}- tethered area.

Figure 6-1. Summary of conclusion. The inserted pictures are reproduced with the permissions. Copyright 2015, American Chemical Society. Copyright 2015, American Chemical Society. Copyright 2016, American Chemical Society. Copyright 2014, American Chemical Society.

List of Tables

List of abbreviations

A

AAS/AES: atomic absorption/emission spectroscopy

B

BL: base layer
BPB: bromophenol blue

C

CA: contact angle
CE: capillary electrophoresis
CNTs: carbon nanotube

D

DCA: dynamic contact angle
DIF: diffusion
DOS: bis(2-ethylhexyl)Sebacate
DTMS: decyltimethoxysilane

E

EDX: energy-dispersive X-ray spectrometry
ET: etching time
Et-CA: ethyl-alpha-cyanoacrylate

G

GD-OES: glow discharge optical emission spectroscopy

H

HAZE: haze

I

IPA: isopropanol
ISEs: ion selective electrodes

K

KD-M13: bis[(benzo-15-crown-5)-4-ylmethyl]pimelate

L

LL: liquid layer

N

NaTFPB: tetrakis[3,5-bis(trifluoromethyl)phenyl]borate sodium salt
NF-S: nanofiber sheet
NPs: nanoparticles

P

PET: polyethylene terephthalate
PFPE: perfluoropolyether
PT: parallel transmittance
PTES: phenyltriethoxysilane
PVC: poly(vinyl chloride)
PVDF-HFP: poly(vinylidene fluoride-*co*-hexafluoropropylene)

S

SA: sliding angle
SCA: static contact angle
SD: spraying distance
SEM: scanning electron microscopy
SLIPS: slippery liquid infused porous surface
SPLASH: surface with π-interacted liquid adsorption, smoothness, and hydrophobicity

T

TB: thymol blue
TEOS: tetraetoxysilane
THF: tetrahydrofuran
TMOS: tetramethoxysilane
TT: total transmittance

W

We: weber number

WT: wetting threshold

X

XPS: x-ray photoelectron spectroscopy

Chapter 1 Introduction

1.1 Background

Biology has provided materials engineers with a number of jumping off points for discovering new materials, and scientists are continuously amazed by the sophistication, uniqueness, and efficiency found in natural materials and systems. [1-5] Nature is indeed a great teacher of materials science and its associated fields such as physics, chemistry, biology, and engineering. [6] Recent developments in nanoscience and (super)molecular engineering have allowed for the establishment of a discipline called ‘biomimetic’ or ‘biomimicry’. [7-9] When the number of international research journals including the keyword of ‘biomimetic’ or ‘biomimicry’ is searched using Elsevier's ‘Scopus’, [10] the largest abstract and citation database of peer-reviewed literature, at least 28662 peer-reviewed papers can be found to have been published. Moreover, the number of publications including these keywords have been increasing from year to year (see **Figure 1-1**). Here, the top 3 journals with the highest publications of biomimetics are ‘Journal of the American Chemical Society (796)’, ‘Biomaterials (609)’, and ‘Angewandte Chemie International Edition (432)’ (see **Figure 1-2** for the top 50 journals and their publication numbers). These 3 journals receive strong attention in materials science due to their high citation by the Thomson Reuters Impact Factor and Google Scholar h-5 index. [11-13]

Therefore, again, it is of current importance for the design of state of the art materials inspired by nature.

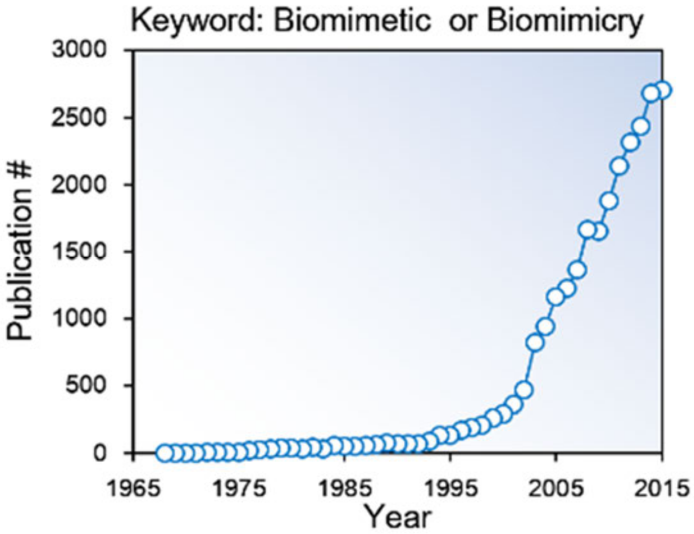

Figure 1-1. Number of peer-reviewed publications including the keyword of biomimetic or biomimicry per year. This output is derived from Elsevier's Scopus. [10]

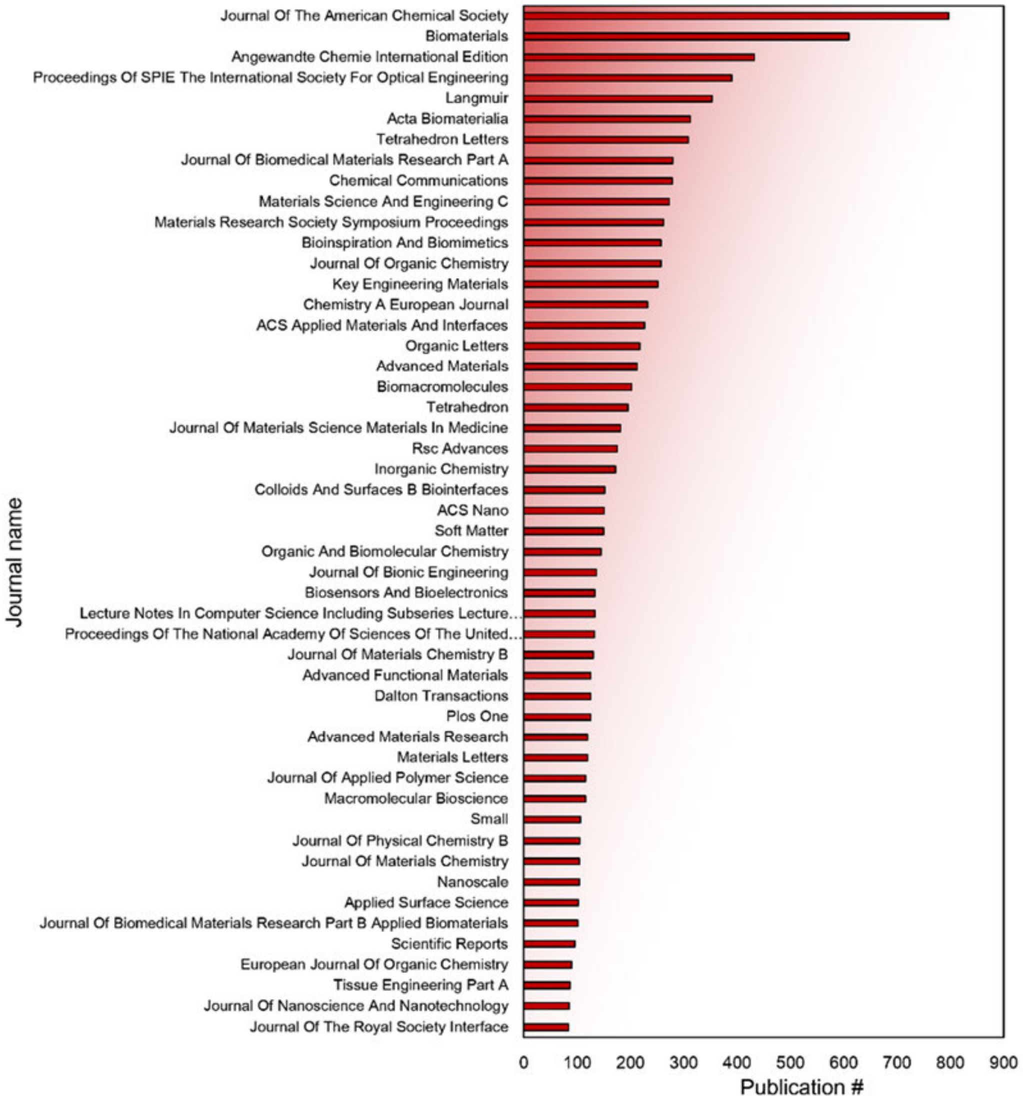

Figure 1-2. Top 50 journals with the number of peer-reviewed publications including the keyword of biomimetic or biomimicry. This output is derived from Elsevier's Scopus. [10]

In the long history of biomimicry, bioinspired materials with special wettability are one of the most studied fields. [14] For instance, the outstanding properties of lotus leave, [15] moth eye, [16] spider web, [17-19] the leg of water strider, [20] gecko, [21] cactus spine, [22] pitcher plant surface, [23-24] plant stoma, [25] buprestidae antenna, [26] desert beetle, [27] and lose petal [28] among other things [29-36] offer remarkably effective ways to design materials with special wettability or systems for various applications. The aim of this thesis work was to design and develop bioinspired materials [37-40] with unique wetting properties by the control of interfacial interactions, nanostructure, and surface chemistry. It is also aimed to give new insight into the biomimetic special wettable materials for the development of whole materials science.

The thesis is organized into 6 chapters including a background chapter (Chapter 1), discussion chapters of bioinspired materials with special wettability (Chapter 2-5), and a summary chapter (Chapter 6) as summarized in **Figure 1-3**.

Chapter 2 describes a way to design anti-wetting materials inspired by the lotus *Nymphaea* leaf's properties. The two strategies of designing (i) a superhydrophobic coating which overcomes the crucial weakness of mechanical instability, and (ii) a biomedical sensor with hydrophobic property, are introduced. [41-42]

Chapter 3 describes a way to design selective-wetting materials biologically inspired by the predation mechanism of the spider *Uloborus walckenaerius*. The spider web-like nanofibrous material described in this work shows antiwetting behavior with respect to water while being penetrated by oil. This selective wetting material is applied to an oil-water separation system. [43]

Chapter 4 describes a way to design "slippery-wetting" materials inspired by the pitcher plant *Nepenthes rafflesiana Jack* which uses such a surface to make insects slide down its leaves into its digestive juices. The immobilization of hydrophobic liquid on a controlled surface enables the design of slippery interfaces, which was then applied for functional anti-wetting coating materials in this work. [44]

Chapter 5 describes a way to design anisotropic-wetting materials learned by water harvesting method of a cactus *Cactaceae*. Water droplets can be driven from tip to base of the spine regardless of orientation on the cactus plant. Here, the anisotropic wetting coating materials which controls droplet motion are realized by patterning of dynamically hydrophobic and statically hydrophobic/hydrophilic patterning, which is applied for micro-fluidic system. [45]

Chapter 6 summarizes the results of this study and a future prospect of biomimetic materials with special wettability.

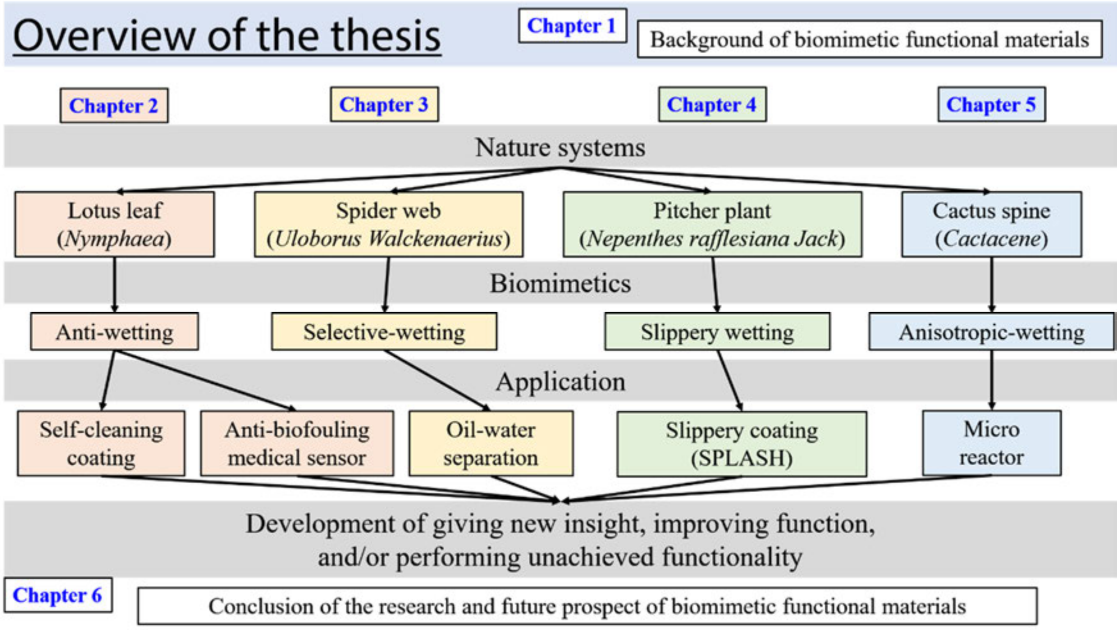

Figure 1-3. Overview of the thesis. This thesis is composed of background chapter, discussion chapters of biomimetic special wettable materials, and their summary chapter.

References

[1-1] Sanchez, C., Arribart, H., & Guille, M. M. G. (2005). Biomimetism and bioinspiration as tools for the design of innovative materials and systems. Nature materials, 4(4), 277-288.

[1-2] Zan, G., & Wu, Q. (2016). Biomimetic and bioinspired synthesis of nanomaterials/nanostructures. Advanced Materials, 28(11), 2099-2147.

[1-3] Sarikaya, M., Tamerler, C., Jen, A. K. Y., Schulten, K., & Baneyx, F. (2003). Molecular biomimetics: nanotechnology through biology. Nature materials, 2(9), 577-585.

[1-4] Fratzl, P. (2007). Biomimetic materials research: what can we really learn from nature's structural materials? Journal of the Royal Society Interface, 4(15), 637-642.

[1-5] Patek, S. N. (2014). Biomimetics and evolution. Science, 345(6203), 1448-1449.

[1-6] Bhushan, B. (2009). Biomimetics: lessons from nature–an overview. Phil. Trans. R. Soc. A, 367, 1445-1486.

[1-7] Pohl, G., & Nachtigall, W. (2015). Biomimetics for Architecture & Design: Nature-Analogies-Technology. Springer.

[1-8] Hubbell, J. A. (1995). Biomaterials in tissue engineering. Nature Biotechnology, 13(6), 565-576.

[1-9] Milwich, M., Speck, T., Speck, O., Stegmaier, T., & Planck, H. (2006). Biomimetics and technical textiles: solving engineering problems with the help of nature's wisdom. American Journal of Botany, 93(10), 1455-1465.

[1-10] Elsevier. (1995). Scopus. Retrieved from https://www.scopus.com/.

[1-11] Clarivate Analytics. (1900). Web of Science. Retrieved from http://ip-science.thomsonreuters.jp/products/web-of-science/.

[1-12] Google. (2004, November, 20). Google Scholar. Retrieved from https://scholar.google.co.jp/.

[1-13] Falagas, M. E., Pitsouni, E. I., Malietzis, G. A., & Pappas, G. (2008). Comparison of PubMed, Scopus, web of science, and Google scholar: strengths and weaknesses. The FASEB journal, 22(2), 338-342.

[1-14] Tian, Y., Su, B., & Jiang, L. (2014). Interfacial material system exhibiting superwettability. Advanced Materials, 26(40), 6872-6897.

[1-15] Feng, L., Li, S., Li, Y., Li, H., Zhang, L., Zhai, J., ... & Zhu, D. (2002). Super-hydrophobic surfaces: from natural to artificial. Advanced materials, 14(24), 1857-1860.

[1-16] Clapham, P. B., & Hutley, M. C. (1973). Reduction of lens reflexion by the

“Moth Eye” principle. Nature, 244(5414), 281-282.

[1-17] Zheng, Y., Bai, H., Huang, Z., Tian, X., Nie, F. Q., Zhao, Y., ... & Jiang, L. (2010). Directional water collection on wetted spider silk. Nature, 463(7281), 640-643.

[1-18] Helmer, M. (2010). Biomaterials: dew catchers. Nature, 463(7281), 618-618.

[1-19] Hagn, F., Eisoldt, L., Hardy, J. G., Vendrely, C., Coles, M., Scheibel, T., & Kessler, H. (2010). A conserved spider silk domain acts as a molecular switch that controls fibre assembly. Nature, 465(7295), 239-242.

[1-20] Hu, D. L., Chan, B., & Bush, J. W. (2003). The hydrodynamics of water strider locomotion. Nature, 424(6949), 663-666.

[1-21] Autumn, K., Liang, Y. A., Hsieh, S. T., Zesch, W., Chan, W. P., Kenny, T. W., ... & Full, R. J. (2000). Adhesive force of a single gecko foot-hair. Nature, 405(6787), 681-685.

[1-22] Park, K. C., Kim, P., Grinthal, A., He, N., Fox, D., Weaver, J. C., & Aizenberg, J. (2016). Condensation on slippery asymmetric bumps. Nature, 531 (7592), 78–82.

[1-23] Wong, T. S., Kang, S. H., Tang, S. K., Smythe, E. J., Hatton, B. D., Grinthal, A., & Aizenberg, J. (2011). Bioinspired self-repairing slippery surfaces with pressure-stable omniphobicity. Nature, 477(7365), 443-447.

[1-24] Chen, H., Zhang, P., Zhang, L., Liu, H., Jiang, Y., Zhang, D., ... & Jiang, L. (2016). Continuous directional water transport on the peristome surface of Nepenthes alata. Nature, 532(7597), 85-89.

[1-25] Hou, X., Hu, Y., Grinthal, A., Khan, M., & Aizenberg, J. (2015). Liquid-based gating mechanism with tunable multiphase selectivity and antifouling behaviour. Nature, 519(7541), 70-73.

[1-26] Schütz, S., Weissbecker, B., Hummel, H. E., Apel, K. H., Schmitz, H., & Bleckmann, H. (1999). Insect antenna as a smoke detector. Nature, 398(6725), 298-299.

[1-27] Parker, A. R., & Lawrence, C. R. (2001). Water capture by a desert beetle. Nature, 414(6859), 33-34.

[1-28] Bhushan, B., & Her, E. K. (2010). Fabrication of superhydrophobic surfaces with high and low adhesion inspired from rose petal. Langmuir, 26(11), 8207-8217.

[1-29] Li, L., Connors, M. J., Kolle, M., England, G. T., Speiser, D. I., Xiao, X., ... & Ortiz, C. (2015). Multifunctionality of chiton biomineralized armor with an integrated visual system. Science, 350(6263), 952-956.

[1-30] Gladman, A. S., Matsumoto, E. A., Nuzzo, R. G., Mahadevan, L., & Lewis, J. A. (2016). Biomimetic 4D printing. Nature materials.

[1-31] Jin, H. J., & Kaplan, D. L. (2003). Mechanism of silk processing in insects and

spiders. Nature, 424(6952), 1057-1061.

[1-32] Sarikaya, M., Tamerler, C., Jen, A. K. Y., Schulten, K., & Baneyx, F. (2003). Molecular biomimetics: nanotechnology through biology. Nature materials, 2(9), 577-585.

[1-33] Koch, K., Bhushan, B., Ensikat, H. J., & Barthlott, W. (2009). Self-healing of voids in the wax coating on plant surfaces. Philosophical Transactions of the Royal Society of London A: Mathematical, Physical and Engineering Sciences, 367(1894), 1673-1688.

[1-34] Tang, Z., Kotov, N. A., Magonov, S., & Ozturk, B. (2003). Nanostructured artificial nacre. Nature materials, 2(6), 413-418.

[1-35] Munch, E., Launey, M. E., Alsem, D. H., Saiz, E., Tomsia, A. P., & Ritchie, R. O. (2008). Tough, bio-inspired hybrid materials. Science, 322(5907), 1516-1520.

[1-36] Ball, P. (1999). Engineering shark skin and other solutions. Nature, 400(6744), 507-509.

[1-37] Yamamoto, M., Nishikawa, N., Mayama, H., Nonomura, Y., Yokojima, S., Nakamura, S., & Uchida, K. (2015). Theoretical explanation of the lotus effect: superhydrophobic property changes by removal of nanostructures from the surface of a lotus leaf. Langmuir, 31(26), 7355-7363.

[1-38] Singh, N., Mondal, D., Sharma, M., Devkar, R. V., Dubey, S., & Prasad, K. (2015). Sustainable Processing and Synthesis of Nontoxic and Antibacterial Magnetic Nanocomposite from Spider Silk in Neoteric Solvents. ACS Sustainable Chemistry & Engineering, 3(10), 2575-2581.

[1-39] Lee, L., Zhang, Y., Ozar, B., Sensen, C. W., & Schriemer, D. C. (2016). Carnivorous nutrition in pitcher plants (Nepenthes spp.) via an unusual complement of endogenous enzymes. Journal of proteome research, 15(9), 3108-3117.

[1-40] Ju, J., Zheng, Y., & Jiang, L. (2014). Bioinspired one-dimensional materials for directional liquid transport. Accounts of chemical research, 47(8), 2342-2352.

[1-41] Tenjimbayashi, M., & Shiratori, S. (2014). Highly durable superhydrophobic coatings with gradient density by movable spray method. Journal of Applied Physics, 116(11), 114310.

[1-42] Tenjimbayashi, M., Komatsu, H., Akamatsu, M., Nakanishi, W., Suzuki, K., Hill, J. P., ... & Ariga, K. (2016). Determination of blood potassium using a fouling-resistant PVDF–HFP-based optode. RSC Advances, 6(17), 14261-14265.

[1-43] Tenjimbayashi, M., Sasaki, K., Matsubayashi, T., Abe, J., Manabe, K., Nishioka, S., & Shiratori, S. (2016). A biologically inspired attachable, self-standing nanofibrous membrane for versatile use in oil–water separation. Nanoscale, 8(21),

10922-10927.

[1-44] Tenjimbayashi, M., Togasawa, R., Manabe, K., Matsubayashi, T., Moriya, T., Komine, M., & Shiratori, S. (2016). Liquid-Infused Smooth Coating with Transparency, Super-Durability, and Extraordinary Hydrophobicity. Advanced Functional Materials, 26(37), 6693-6702.

[1-45] Tenjimbayashi, M., Higashi, M., Yamazaki, T., Takenaka, I., Matsubayashi, T., Moriya, T., Komine, M., Yoshikawa, R., Manabe, K., & Shiratori, S. (2017). Droplet Motion Control on Dynamically Hydrophobic Patterned Surfaces as Multifunctional Liquid Manipulators. ACS Applied Materials & Interfaces, 9(12), 10371-10377.

Chapter 2 Anti-wetting materials inspired by lotus *Nymphaea* leaf property

This chapter is based on [Tenjimbayashi, M., & Shiratori, S. (2014). Highly durable superhydrophobic coatings with gradient density by movable spray method. Journal of Applied Physics, 116(11), 114310.] and [Tenjimbayashi, M., Komatsu, H., Akamatsu, M., Nakanishi, W., Suzuki, K., Hill, J. P., ... & Ariga, K. (2016). Determination of blood potassium using a fouling-resistant PVDF–HFP-based optode. RSC Advances, 6(17), 14261-14265.]

2.1 Anti-wetting property

In this chapter, lotus leaf inspired anti-wetting surfaces are introduced. A lotus leaf has nano-micro dual scale structure and it is covered with hydrophobic wax, that performs excellent water repellency of water contact angle > 150° and low water contact angle hysteresis. [1] Such water-repellent property is called superhydrophobicity [2] having a wide range of potential applications such as self-cleaning, [3-5] anti-fouling, [6, 7] contamination-free coating, [8, 9] drag reduction, [10, 11] anti-icing, [12-14] anti-bacterial, [15, 16] and corrosion prevention. [17]

Superhydrophobic surfaces must have both the special textured structure that traps an air layer and the low surface energy. [18] The effect of surface energy on wettability is deliberated by Thomas Young that the liquid contact angle θ_Y on solid surface is derived by $\gamma_{SV} = \gamma_{SL} + \gamma_{LV} \cos\theta_Y$ where γ_{SV} is solid-vapor interfacial energy, γ_{SL} is solid-liquid interfacial energy, and γ_{LV} is liquid-vapor interfacial energy. [19] The Young's equation indicates that the low surface energy of the solid and the high solid-liquid interfacial tension (low interaction between them) are crucial for enhancing the surface hydrophobicity. However, the control of these interfacial tensions is not enough for the surface to achieve superhydrophobicity. Hence, another factor enhancing their hydrophobicity is required. The effect of surface roughness on wettability is discussed by Wenzel, Cassie and Baxter state. [20-21] Wenzel state describes the homogeneous wetting model on the rough surface, and the liquid contact angle θ_W is defined as $cos\,\theta_W = r\,cos\,\theta_Y$, where r is roughness enhanced surface area, indicating that the hydrophobic properties are emphasized by surface roughness. However, Wenzel model cannot really be well fitted by measured contact angles when the Yong angle is 52°<θ_Y< 90° due to the pinning of droplet. [22] Instead of that, the roughness effect on the wettability is explained using Kang-Jacobi equation. [23] On the other hand, Cassie-Baxter state is used when dealing with a heterogeneous surface, and the liquid contact angle θ_{CB} is defined as $\gamma_{LV}\,cos\,\theta_{CB} = \sum_{i=1}^{N} f_i({\gamma^i}_{SV} - {\gamma^i}_{SL})\ b.c. \sum_{i=1}^{N} f_i = 1$, where f_i is surface fraction of component i. Notice that the textured surfaces are composed of air layer and the solid, θ_{CB} yields to $cos\,\theta_{CB} = -f_{air} + f_{solid}\,cos\,{\theta^*}_W$, where ${\theta^*}_W$ is Wenzel angle of liquid-solid contact area, signifying the liquid contact angle can drastically increases by trapping an air layer on the solid surface. Considering the two models, there is the transition threshold of critical contact angle θ_C between Wenzel and Cassie-Baxter angle which is defined as $cos\,\theta_C = (\phi - 1)/(r - \phi)$, where ϕ is the fraction of liquid-solid contact area. [24] In this state, the equilibrium liquid contact angle θ_T is defined as $cos\,\theta_T = \phi\,cos\,\theta_C + (1 - \phi)$. Therefore, in any state, the rougher the hydrophobic surface is, the more hydrophobic it gets.

From these theoretical progresses, a methodology of superhydrophobic surfaces has been well-researched for recent 25 years, due to their potential applications above. [25-40] However, superhydrophobic surfaces still have challenges in terms of coating process [41], and mechanical durability [38] since the well-organized textured surfaces are usually fragile and difficult to design easily. Thus, in section 2.2, the facile way to design mechanically durable superhydrophobic coating is introduced. [42]

Moreover, since the concept of superhydrophobic surfaces reduce the liquid-solid interaction, it seems difficult to apply (super)hydrophobic coating as an antifouling function to liquid-solid interaction based sensor. Thus, in section 2.3, the hydrophobic optical electrode (optode) which determinates ion concentration in a liquid as well as anti-fouling property is shown as a rarely reported example of a combination of "sensor technology" and "antifouling coating technology". Introduction of the antifouling feature to optode sensing improves the potential applicability of the technique and, in this case, will permit development of portable blood sensing monitoring devices for easy use in the field with the added advantage of fouling-resistance for more reliable serial usage. [43]

2.2 Design of Mechanically Durable Superhydrophobic Coating

2.2.1 Introduction

Superhydrophobic surface is expected to be applied in various applications; however, it has crucial defect in terms of durability, and large scale fabrication. [38] Previously, many researchers aimed to design mechanically durable superhydrophobic surfaces *via* scalable approaches. For instance, Jung and Bhushan [44] sprayed a carbon nanotubes (CNTs)/epoxy resin mixture on the substrates. The coated surface performed superhydrophobicity against the high-pressure water jet due to uniform distribution and strong bonding of CNTs on flat epoxy resin. Zhu et al. [45] reported fluorinated metal/polymer composite structure designed by one-step immersion method. The products coated on a copper plate showed stability against several times finger touch (in general ~8 kPa) because the fluorinated metal existed not only the surface but also the exposed area after abrasion. These approaches offered an idea of mixing adhesive resin with hydrophobic nanomaterials to design simple and robust superhydrophobic surfaces. However, the challenge of designing mechanically super-durable (>50 kPa abrasion resistance) superhydrophobic surface by a facile way is remaining, and such a durable surface has never been reported at least until 2014 as far as our group had investigated.

Here, the strategy to design super-durable superhydrophobic coating by one-step spray method is introduced. [42] Our approach is not just the formation of the hydrophobic nanoparticles (NPs)/adhesive resin composite structure, but the designing NPs/resin surface-depth-direction gradient density structure (i.e. the coating-air interface is filled with NPs, gradually the resin ratio increases as getting the depth, and the coating-substrate interface is filled with the resin) by proposed one-step spraying method. We discovered hydrophobic silica NPs and ethyl-alpha-cyanoacrylate (Et-CA) (resin) mixture was able to tune the NPs/Resin volume ratio on the coating by the spraying distance (SD). Using this character, we propose the ‘movable spraying method’ to fabricate the robust hydrophobic coating with gradient density (hydrophobic NPs and Et-CA) by continuous increase of SD. This method is 1 step spraying method and easily coat-able on complex shape and large area substrates.

In this section, we investigated the influence of SD on the mechanical durability and wettability of the coating. Then, the gradient structure by movable spray method was evaluated. Finally, superhydrophobic structures with different structure by NPs or NPs/Resin composite (see **Figure 2-1**) were compared.

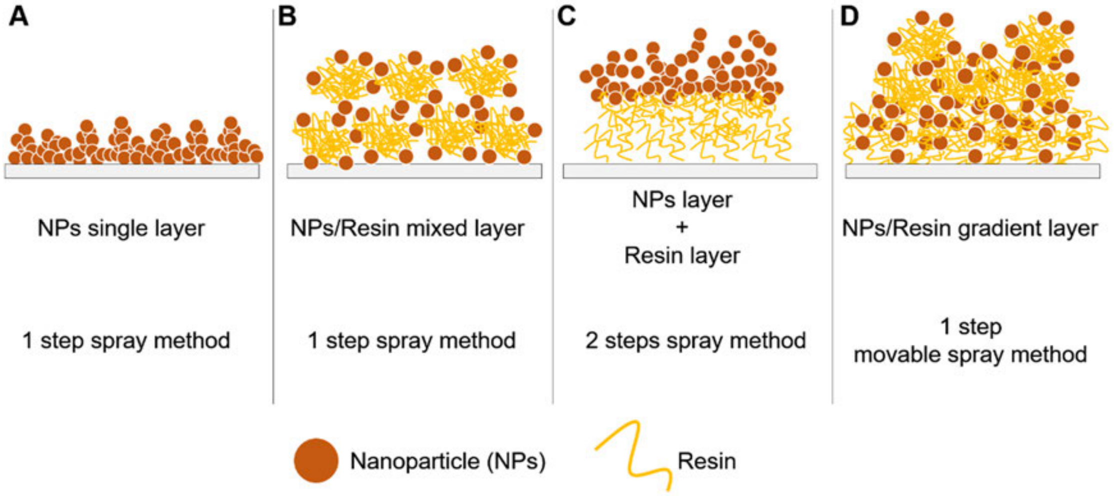

Figure 2-1. Schematic illustrations of superhydrophobic structures with different structure by NPs or NPs/Resin composite, which are (A) single layer NPs coating by a single step spray method, (B) NPs/Resin composite coating by spraying NPs/Resin mixture, (C) NPs and resin double layer coating by double steps spray method, and (D) the NPs/Resin gradient coating by single step movable spray method, respectively.

2.2.2 Experimental

Cocktail preparation. 3.7 wt. % hydrophobic silica NPs (diameter:12 nm, RX 200, Evonik industries, Germany) were dispersed in acetone using ultrasonic treatment for 10 minutes. Then, ethyl-alpha-cyanoacrylate (purity: 99.5%, Kobunsi Shoji Co., Ltd., Japan) was added and the dispersion was stirred for 3 hours.

Spray condition. Spray condition is summarized in **Table 2-1**. In this work, only the SD was varied from 10-50 cm. A sample where the spray mixture was casted was defined as 0 cm of SD. The coatings were basically prepared on glass substrate (Matsunami Glass Industries, Ltd., Kishiwada, Japan).

Table 2-1. The spraying parameters used in this work.

Parameters	Coating conditions					
Coating method	Cast	Spray	Spray	Spray	Spray	Spray
Sprayer type	-	Airtex (Japan)	Airtex (Japan)	Airtex (Japan)	Airtex (Japan)	Airtex (Japan)
Pressure (MPa)	-	0.7	0.7	0.7	0.7	0.7
Nozzle diameter (mm)	-	0.6	0.6	0.6	0.6	0.6
Volume (mL)	-	5	5	5	5	5
SD (cm)	0	10	20	30	40	50

Movable spray method. Movable spray method was used, the SD was gradually changed, to allow the gradient structure to be prepared. We characterized surfaces prepared at each constant SD, and then assessed the suitability of the preparation method for preparing gradient structure.

Characterization. Surface wettability was evaluated by measuring water contact angle and sliding angle. The measurements were conducted by a sessile drop method using a device created from our laboratory. Surface morphology was evaluated by surface roughness using laser microscopy (VK-9710, Keyence, Japan) and structures using field emission scanning electron microscopy (SEM, S4700, Hitachi, Japan). Surface chemistry was investigated using x-ray photoelectron spectroscopy (XPS, JPS-9010TR, JEOL, Japan). Mechanical durability was observed using an abrasion device (Tribogear Type 18L, Shinto Scientific Co., Ltd., Japan). The abrasive material was a cotton fabric and each test was conducted with 10 rounds abrasion at variable pressure. Surface-to-depth direction chemical components were analyzed using by glow discharge optical emission spectroscopy (GD-OES, GDProfiler2, HORIBA Scientific Co., Ltd., France) for the observation of gradient structure on Al substrate.

Comparison of NPs/Resin composite coatings. To investigate the mechanically durable composite structure, we prepared 4 kinds of the surfaces in **Figure 2-1A-D**. NPs single layer was designed by just spraying the mixture without Et-CA. NPs/Resin mixed layer was designed by spraying the mixture at SD=30 cm. NPs layer + Resin layer was prepared by firstly spraying the mixture without silica NPs; then spraying the mixture without Et-CA. NPs/Resin gradient layer was prepared by movable spray method with gradually changing from SD=10 cm to 50 cm. These coatings were compared via mechanical durability test.

2.2.3 Results and Discussion

Surface analysis with each spray distance. The SD strongly relates with the resulting surface coating morphology, wettability and chemistry. **Figure 2-2** shows the XPS analysis of coatings prepared at each SD. In each SD, the intense peaks obtained by **Figure 2-2A** are Si-2p in 97eV (In theory 99 eV) and Si-2s in 157 eV (In theory 151 eV) from NPs, C-1s in 288 eV (In theory 285 eV) from both Et-CA and hydrophobic group in NPs, N-1s (In theory 402 eV) from cyano group in Et-CA. Magnified XPS spectrum are shown in **Figures 2-2B**, **C**. Whereas the intensities of N-1s and Si-2p peak are increased with SD due to the increase in surface roughness (**Figure 2-3A**) and scanning area, the Si/N atomic ratio increased from 0.77 to 1.62 with increasing the SD from 0 to 30 cm indicating a surface NPs ratio increase (**Figure 2-2D**). Moreover, the Si/N ratio was almost constant in the SD from 30 to 50 cm. This is probably because the solvent evaporates complete in the SD=30 cm, and the deposition behavior of mixtures does not differ when the SD is more than 30 cm.

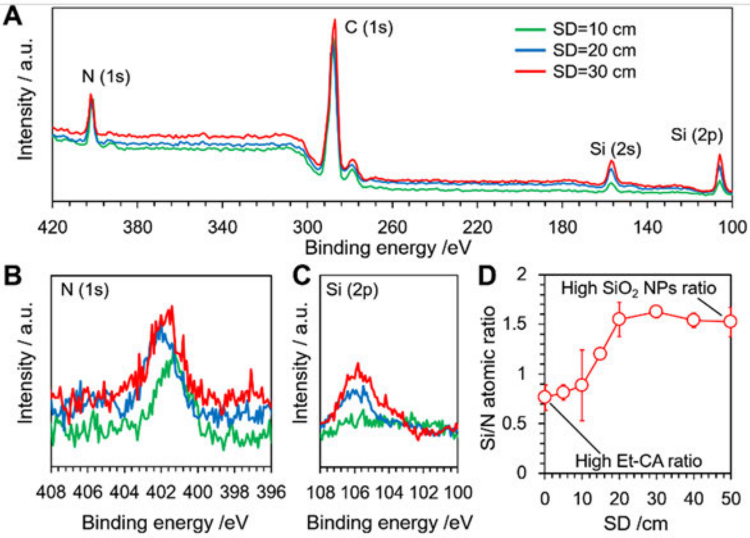

Figure 2-2. (A) XPS spectrum of coatings at different SDs. (B) Si-2p peak and (C) N-1s peak were analyzed. (D) The SD dependence on Si/N atomic ratios. The higher Si/N ratios indicate the higher surface NPs occupancy. (n=3)

The surface morphologies of coatings at each SD are shown in **Figure 2-3**. It indicates that the surface roughness fractally increases with the SD in the range (**Figure 2-3A-C**). The roughness change is quantified using a roughness value of root-mean square roughness R_{rms}. [46] The values increased from 1.097, 11.898, to 20.256 µm with varying SD from 10, 20, to 30 cm. The SEM observation (**Figure 2-3D-I**) revealed the surface NPs rate increases with the SD; The spraying at SD=10 cm formed sheet-like structure with the NPs' embedded in Et-CA (**Figure 2-3G**) whereas the coating at SD= 30 cm was hierarchically NPs' self-assembled structure (**Figure 2-3I**).

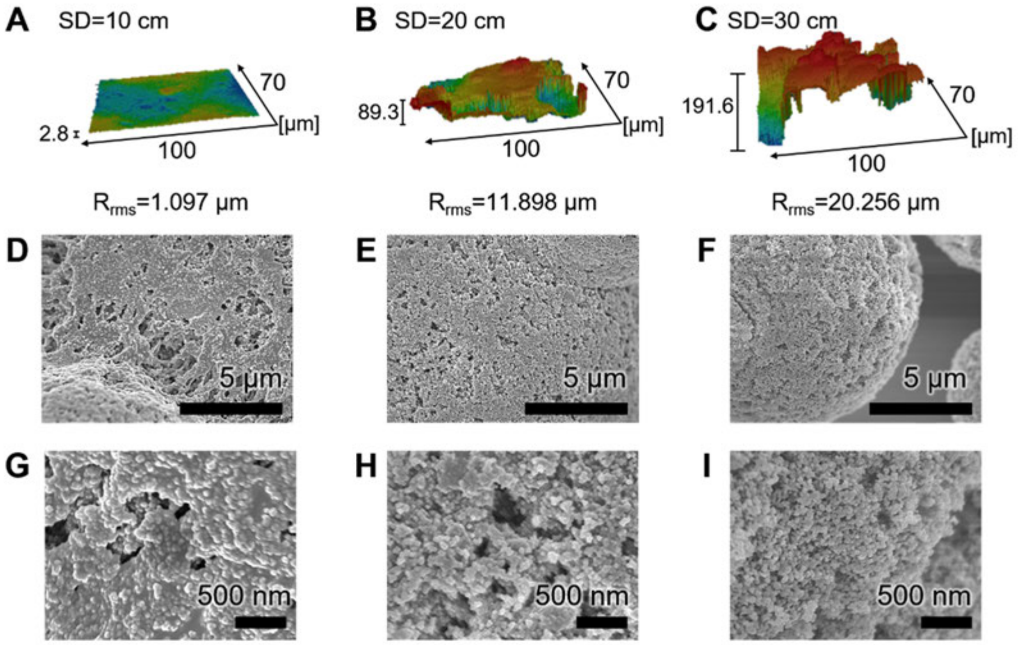

Figure 2-3. Morphological analysis of coatings at different SDs. (A)-(C) Laser microscopic images of coatings at (A) SD=10 cm, (B) SD=20 cm, and (C) SD=30 cm with R_{rms} values. (D)-(I) SEM images of coatings at (D) and (G) SD=10; (E) and (H) SD=20; (F) and (I) SD=30 cm.

The changes of surface roughness and NPs/Et-CA ratio with the SD are discussed by considering the change in spraying mixture as shown in **Figure 2-4A**. The mixture is comprised of acetone as a solvency, Et-CA monomer, and NPs. In the mixture, Et-CA initially dissolved and NPs dispersed in acetone, and acetone evaporated to a greater degree with increasing the SD. Driven by the evaporation of acetone, the mixture droplets aggregated by surface tension, and Et-CA entered inside the mixture rather than NPs because the affinity of Et-CA $\delta_{\text{Et-CA}}$ was much higher than that of NPs δ_{NPs}. At this point, the possible evaporation of Et-CA was neglected, because the weight loss of Et-CA had been less than 1% when Et-CA dissolved in acetone heated 24 h at 50 ºC. Hence, in short, the mixture aggregates driven by solvent evaporation. It drives Et-CA to enter inside the mixture rather than NPs, resulting the decrease of Et-CA density in the mixture. This explanation is consistent with the XPS results (**Figure 2-2D**). Moreover, we considered the structure of coatings at each SD as shown in **Figure 2-4B**. Since the evaporation of solvent makes the mixture to decrease the mass of solvent and the density of Et-CA, the coating at SD=30 cm is formed by the deposition of solvents' evaporated NPs and Et-CA with small density, whereas the coating at SD=10 cm is formed by the adhesion of solvent with NPs and high density Et-CA. Thus, the former one is relative rougher than the latter one due to the difference of mixture density. [42] It reasonably explain the morphology change in **Figure 2-3A-C**.

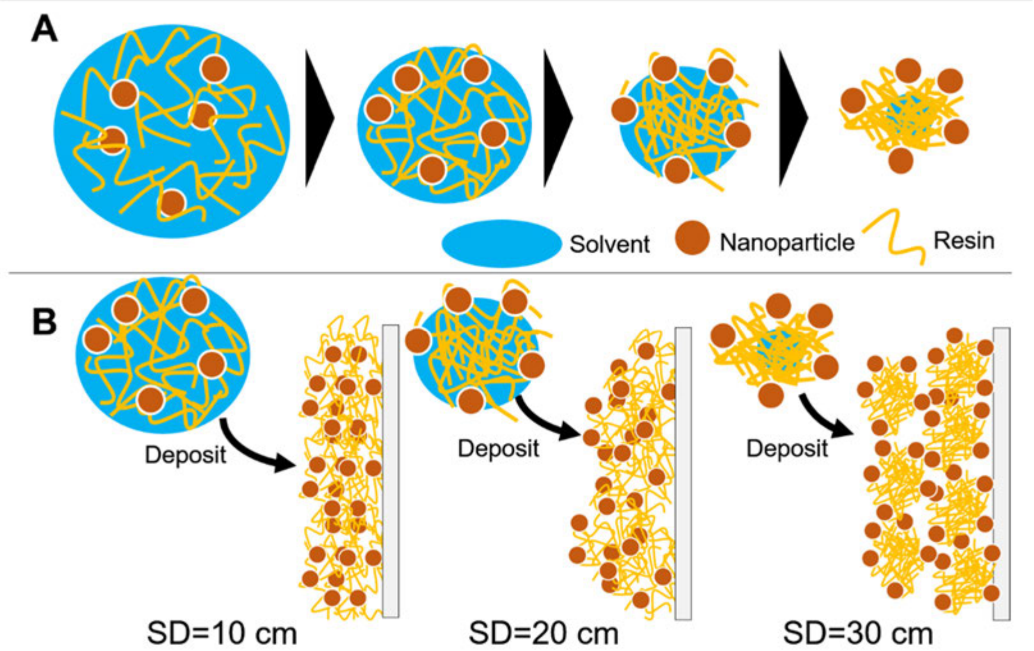

Figure 2-4. Schematic illustrations of (A) the spraying mixture change in spraying. The mixture aggregates driven by solvent evaporation. Because the affinity of Et-CA to solvent is higher than that of NPs, Et-CA enter inside the mixture rather than NPs. It results the aggregation of Et-CA in the mixture. (B) the models of structure formed at each of the SDs. As increasing the SD, the surface volume of Et-CA as well as acetone in the mixture decrease; thus, the Si/N ratio and surface roughness can be controlled by the SD.

Wettability of the coatings at various SDs is shown in **Figure 2-5A**; indicating the water contact angle increases with the SD as well as the Si/N ratio and surface roughness. Since, the water young angle on Et-CA, NPs, and air were 52º (as measured by us), 99º, and 180º, respectively, [47] the water contact angle yields: $\cos\theta_{CB} = -f_{air} + f_{Et-CA}\cos 52° + f_{NPs}\cos 99°\ (b.c. f_{air} + f_{Et-CA} + f_{NPs} = 1)$ in Cassie-Baxter state, or $\cos\theta_W = r(f_{Et-CA}\cos 52° + f_{NPs}\cos 99°)\ (b.c. f_{Et-CA} + f_{NPs} = 1)$ in Wenzel state. The differentiation of these states was observed by simple droplet adhesion test as shown in **Figure 2-5B**; the coating at SD=10 cm show Wenzel state wetting behavior due to the adhesion of a water droplet whereas the coating at SD=20 cm contact water with Cassie-Baxter state to show superhydrophobicity. [48] Thus, the threshold of wetting Wenzel and Cassie-Baxter state transition exists between the SD=10-20 cm. In Wenzel state at the SD is 0-10 cm, the contact angle increases with the SD due to the Kang-Jacobi theory. [22] On the other hand, the increase of water contact angle with the SD ranging from 30 to 50 cm is due to the increase of f_{air} (positively relates with the surface roughness) and f_{NPs}/f_{Et-CA}. However, as the increase of surface roughness with the SD, the coatings become fragile and hence the deterioration of contact angle gets larger as shown in **Figure 2-5A**. Therefore, the relationship between a hydrophobicity and a mechanical durability is found to be trade-off.

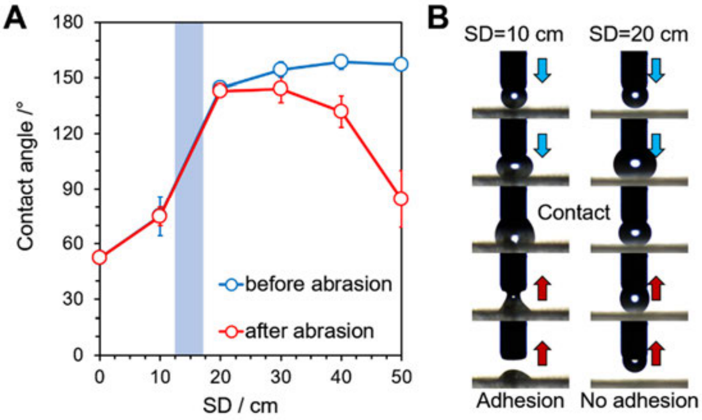

Figure 2-5. (A)Water contact angles on the coatings at various SDs before and after abrasion. The abrasion was conducted under the pressure at 5 kPa. (n=3) (B) Water droplet adhesion test on the coatings at SD=10 and 20 cm to differentiate the wetting model whether the surface is Wenzel state or Cassie-Baxter state.

Design of NPs/Resin gradient layer by movable spray method. To overcome the trade-off between a hydrophobicity and a mechanical durability, variable distance spraying: movable spray method was used for the preparation of mechanically durable superhydrophobic coating. The movable spray was conducted with SD gradually changed from 10 to 50 cm so as spraying 5 mL of the mixture. In close SD, Et-CA rich composite layer was formed whereas the long-range SD spraying formed NPs rich composite layer. Thus, the NPs/Et-CA gradient structure can be obtained as shown in **Figure 2-1D**. The gradient density of NPs and Et-CA was confirmed using GD-OES spectrum in **Figure 2-6A**. It results the Si peak from NPs gradually decreased, while N peak from Et-CA increased with the etching time (ET) in the region of ET=0-24.8 s. That's because the self-assembled outermost NPs are firstly etched by Ar sputter resulting in the exposure of the resin layer. Note that the NPs inside the self-assembled layer are also etched by Ar sputter through the nano spaces between hierarchical structures. The increase of Al peak is due to the exposure of substrate caused by etching of thin coating area. However, in the region of ET=~30.0 s, Al peak becomes constant, and both Si and N peak gradually decrease with ET due to the etching achieving to the substrate. Since the outermost surface is air-solid composite layer, the spectrum in ET=0-2.8 s was unstable. As the ET is mostly in proportion to the distance from surface to substrate, the spectrum versus ET can be approximated with the spectrum versus surface depth. It indicates the gradual decrease of NPs density and increase of Et-CA density. Moreover, the structure of gradient coating was observed using SEM (**Figure 2-6B-D**). The outermost surface was filled with NPs (**Figure 2-6C**) whereas the cross-section was the NPs-embedded Et-CA layer (**Figure 2-6D**).

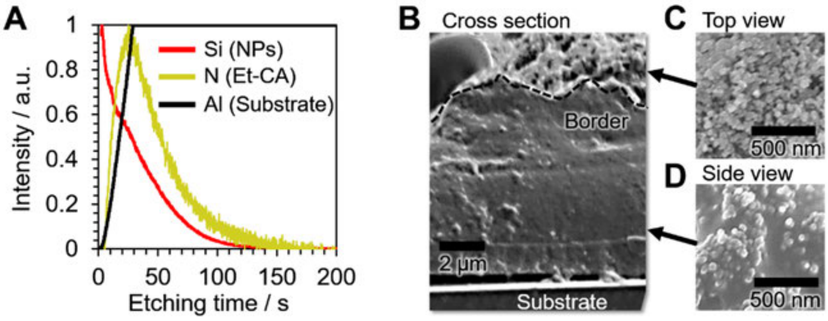

Figure 2-6. (A) GD-OES spectrum of NPs/Resin gradient layer on Al substrate as a function of etching time. (B)-(D) SEM images of the gradient layer on the substrate of (B) the tilting section, where the black dashed line indicates the border between the top and side of cross-section: (C) top view, and (D) side view.

The mechanical durability of the gradient layer coatings on various substrates was compared with simple NPs coating on the glass as shown in **Figure 2-7A**. The gradient coated aluminum, wood, and glass kept their superhydrophobicity even after the abrasion test under the pressure at 50 kPa whereas NPs coated glass lost their superhydrophobicity to be hydrophilic after the 10 kPa abrasion. There were no apparent differences in mechanical durability between the three substrates.

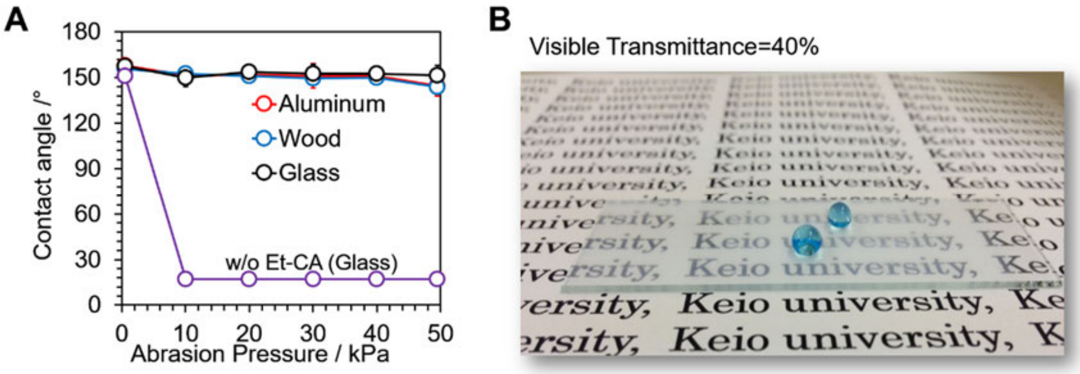

Figure 2-7. (A) Abrasion strength versus hydrophobicity of the gradient layer coated various substrates and simple NPs coating without Et-CA on glass. (B) A photographic image of the gradient layer coated glass.

Mechanical durability comparison of the superhydrophobic coatings. The mechanical durability of NPs/Resin gradient layer coating is compared with NPs single layer, NPs/Resin mixed layer, and NPs+Resin double layer (**Figure 2-1**). It is noteworthy that the gradient coating performed the best mechanical durability in the coatings as shown in **Figure 2-8A**. This is apparent that the gradient layer coating is mechanically more stable than the single NPs coating and the mixed coating due to the volume of Et-CA. The reason the gradient layer is more stable than the double layer is probably due to the interfacial energy between NPs and Et-CA. As shown in scheme in **Figure 2-8B**, the double layer coating is comprised with NPs layer and Resin layer; the adhesion of NPs with low surface tension to Et-CA is weak. On the other hand, the gradient structure continuously changes the NPs/Resin ratio with surface depth, which can treat as continuous multi-layers with little characteristic differences. Thus, the adhesion of every layers is relatively stronger than that of NPs/Resin interface.

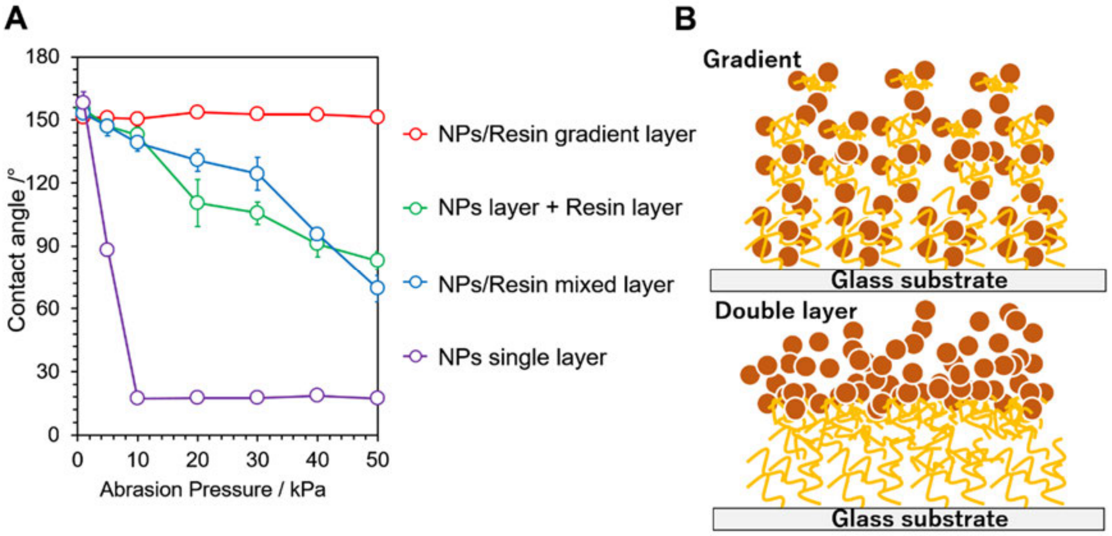

Figure 2-8. (A) Mechanical durability comparison of the NPs/Resin gradient layer, NPs + Resin layer, NPs/Resin mixed layer, and NPs single layer. (B) Schematic illustration to study the mechanical durability difference between NPs/Resin gradient layer (upper one), and NPs + Resin layer (bottom one).

2.2.4 Conclusions

In conclusion, a mechanically durable superhydrophobic coatings are designed by spraying method. The fundamental study of spray distances on the chemical or morphological variation of nanoparticles/ethyl cyanoacrylate composite coatings offered an idea to design gradient density structure using the spraying method that continuously change the spraying distance. Furthermore, mechanically durable superhydrophobic composite coatings are compared, to be found the gradient layer designed by ‘movable spray method’ performed the best mechanical durability. The facile-versatility, excellent mechanical durability, and superhydrophobicity can be helpful to practically apply superhydrophobic coating in industry. Also, the methodology contributes to develop gradient functional materials.

2.3 Design of hydrophobic polymer based optode for blood contamination-free K+ sensing

2.3.1 Introduction

Since the superhydrophobic surface decreases the contact area with liquid, giving the anti-fouling properties to materials which require the interaction with liquid contents such as optical electrode (optode) [49] are difficult by using the conventional lotus surface. However, even though the inexistence of surface air layer, low energy surface can prevent them from liquid adhesions. Hence, in this section we developed a potassium sensor for blood with blood-fouling resistance as a rarely reported example of a combination of ‘surface reactive sensor technology’ and ‘antifouling coating technology’ to advance the lotus inspired technique to wider range applications. Introduction of the antifouling feature to optode sensing improves the potential applicability of the technique and, in this case, will permit development of portable blood sensing monitoring devices for easy use in the field with the added advantage of fouling-resistance for more reliable serial usage.

Potassium ions are physiologically significant and one of the most abundant elements found intra- and extra-cellular media. [50], [51] For the diagnosis of hyper- or hypo-kalemia, which can cause various deceases including potentially fatal cardiac arrhythmias, [52] the determination of potassium levels in patients' blood is of significance for clinical analysis. Previously, various methods for the quotative determination of electrolytes in blood have been developed such as atomic absorption/emission spectroscopy (AAS/AES), [53] capillary electrophoresis (CE), [54] and ion selective electrodes (ISEs). [55] However, these methods require special devices and usually additional calibration. [56]

As an alternate, polymeric bulk optodes has been utilized for quantification of electrolyte in blood. Insertion of an ionophore selective for a reference ion into the sensor membrane allows to monitor the protonation degree of a dyestuff which can in number be used to quantify the activity of the target ion in analyte samples since the response mechanism is based on a competitive ion–exchange equilibrium (see **Figure 2-9A**). [57], [58] Optical response of an optode device is usually observed in absorbance or fluorescence mode; since the visual response of the optode can be used to quantify the activity of the primary ion, it is suitable for *in situ* blood analysis in the absence of an electrical supply such as occurs at the time of a natural disaster or in remote locations. However, most of the approaches to blood analysis are based on fluorescence mode, not visual one largely due to contamination of blood hinder accurate sensing in the visual region. In addition, it also increases the risk of infection from the wounds. [59]

Here, we report a visually responsive system for determination of potassium level in blood. The system has the additional property of blood fouling resistance. While in most previous reports adapted poly(vinyl chloride) (PVC) as based polymer, [60], [61] the fluorinated co-polymer: poly(vinylidene fluoride-*co*-hexafluoropropylene) (PVDF-HFP) have been used due to its low surface energy over PVC (**Figure 2-9B**). [62] However, the effect of surface energy on ionic-exchange in liquid-optode interface is not raveled; hence, we investigated the influence of sensor response by changing the polymer from PVC to PVDF-HFP; also, we compared their blood fouling resistance.

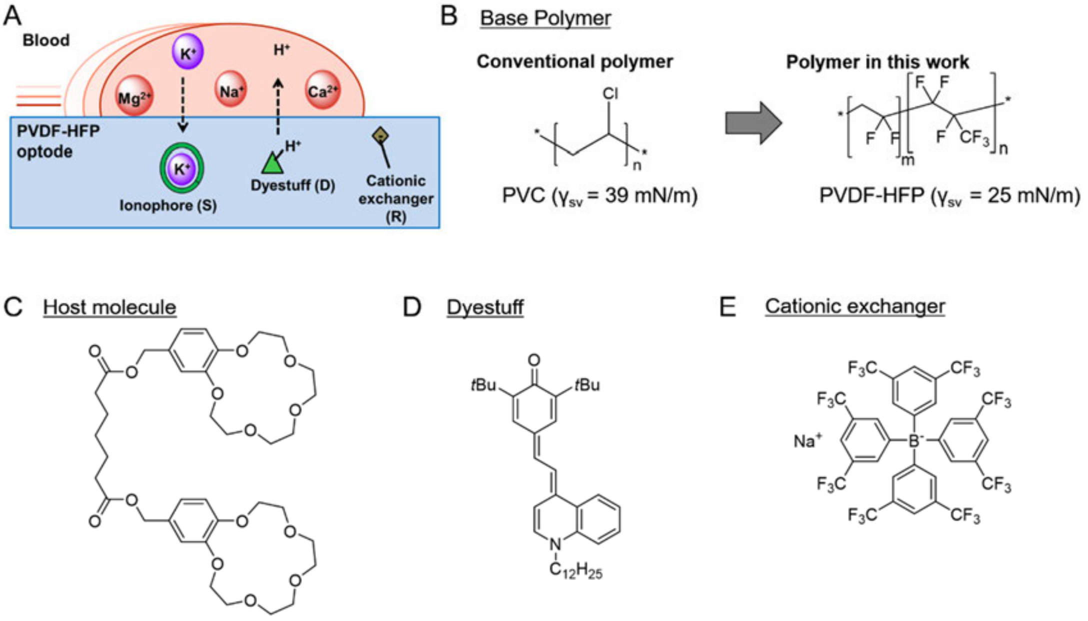

Figure 2-9. (A) Schematic illustrations of potassium ion determination mechanism of polymeric bulk optode. (B)-(E) Chemical structures of the polymers (B), host molecule (C), dyestuff (D), and cationic exchanger (E) used in this work. To give hydrophobic properties to the optode, PVDF–HFP is used as bulk polymer instead of PVC.

2.3.2 Experimental

Materials. Host molecule bis[(benzo-15-crown-5)-4-ylmethyl]pimelate (KD-M13) (**Figure 2-9C** for structure), cation-exchanger tetrakis[3,5-bis(trifluoromethyl)phenyl]borate sodium salt (NaTFPB) (**Figure 2-9E** for structure), and Bis-Tris were purchased from Djindo Laboratories (Japan). Plasticizer bis(2-ethylhexyl)Sebacate (DOS) was purchased from Tokyo Chemical Industry Co., Ltd. (Japan). Dehydrated tetrahydrofuran (THF), KCl, NaCl, $MgCl_2$, $CaCl_2$ were purchased from Kanto Chemical Co., Inc. (Japan). PVC and PVDF-HFP were purchased from Sigma-Aldrich Co., LLC. (USA). HCl aq. and 1 M NaOH aq. were purchased from Nacalai Tesque, Inc.(Japan). Dyestuff KD-M13 was synthesized according to reference (**Figure 2-9D** for structure). [63] Pig blood (including sodium citrate as anticoagulant) was purchased from Tokyo

Shibaura Zouki Co., Ltd. Human blood was purchased from BIOPREDIC International Company (France).

Optodes preparation. 1 g PVDF-HFP or 0.79 g PVC was dissolved in 15 mL THF by stirring 24 h at 60 ºC. Then, the sensing medium 2.6 mg bis[(benzo-15-crown-5)-4-ylmethyl]pimelate, 3.0 mg NaTFPB, 40 μL DOS, and 1.8 mg KD-M13 are mixed in the respective polymer solution (1mL) by stirring for 1 h. The cocktails were coated on a PET film by squeegee method. [62] Here, the PVDF-HFP based one and that of the PVC-based one are 92.5 μm, and 96.8 μm, respectively (**Figure 2-10**).

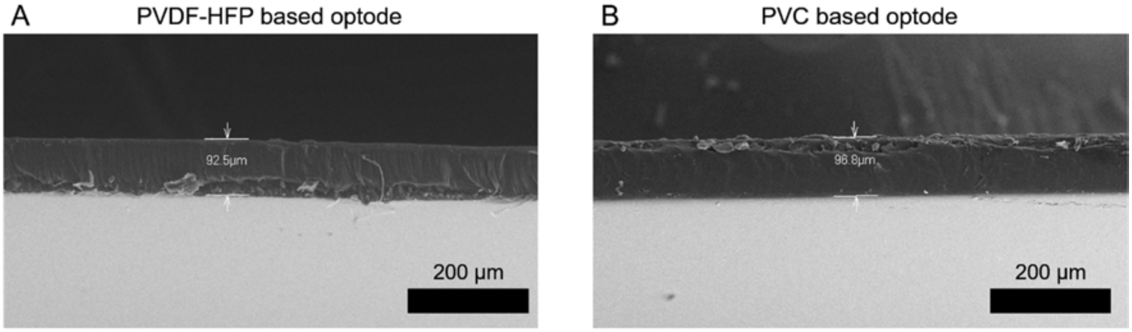

Figure 2-10. Cross-sectional SEM images of (A) PVDF-HFP based optode and (B) PVC based optode. The thickness of the PVDF-HFP based one and that of the PVC-based one are 92.5 μm, and 96.8 μm, respectively.

Analyte sample preparation. All samples were prepared using Tris-buffer and pH was adjusted to 7.4 with HCl aq. KCl, NaCl, $MgCl_2$, and $CaCl_2$ were dissolved in Tris-buffer with different concentrations ranging from 10^{-5} M to 10^{0} M.

Characterization. Absorption spectra of sensor responses were measured by using a Shimadzu UV-3600 UV/Vis/NIR spectrophotometer with each analyte sample solution in a 1 cm quartz cell. For comparison, absorption spectra of completely deprotonated sensor by applying 1 M NaOH aq. was prepared, too. Coupling constants K_{exch} and ion selectivities K^{opt}_{ij} were calculated from the response curve constructed using absorption spectra measured under different chloride salt concentrations. Potassium levels in human blood were measured by using a standard addition method. [64] A color difference meter (Color Reader CR-13, Minolta Co., Ltd., Tokyo, Japan) was used to quantify the color change of the sensor. Blood contact angles and sliding angles were measured by casting pig blood (20 μL) on a Contact-Angle Meter (CA-DT, Kyowa, Tokyo, Japan). Blood contamination area on the sensor was imaged using Image J software (U. S. National Institutes of Health, Bethesda, Maryland, USA). Surface

structure was observed using a scanning electron microscope (SEM, TM3030Plus Microscope, HITACHI, Japan).

2.3.3 Results and Discussion

Mechanism of ion-selective optode. Ion-selective optodes usually respond triggered by selective interaction between hydrogen ions and a oleophilic dyestuff. The films are made to respond to cations under a competitive ion-exchange equilibrium yielding: $M_W^{z+}+zS_O+zD_OH^+R_O^- \leftrightarrow S_{zO}M_O^{z+}R_O^{z-}+zD_O+zH_W^+$ where M^{z+} is the analyte cation, S is the ionophore, D is the dye, R is the cationic ion-exchanger, the subscript W denotes “existing in the analyte solution”, and the subscript O denotes “existing in the polymer film” as shown in scheme in **Figure 2-9A**. When M^{z+} comes in the optode, hydrogen ions are extracted from the film in order to conserve electrical neutrality within the film. This results in the release of protons from the optode without the observable morphological change in the membrane structure (**Figure 2-11**), and thus the deprotonation degree of the dyestuff is changed by M^{z+} concentration to turn into the color as shown in **Figure 2-12A**. Considering the mechanism of the ion exchange, the dynamic range of optodes can be turned by the pH value like **Figure 2-12B**; To obtain linear response curve for the potassium determination in human blood, we have to design the appropriate ion carriers, and dyestuff. Using the sensing materials in this work, we can obtain linear response at the 10 mM of potassium concentration and at pH ranges between 6-8, which fulfills a condition for human blood determination (**Figure 2-12C**, **D**).

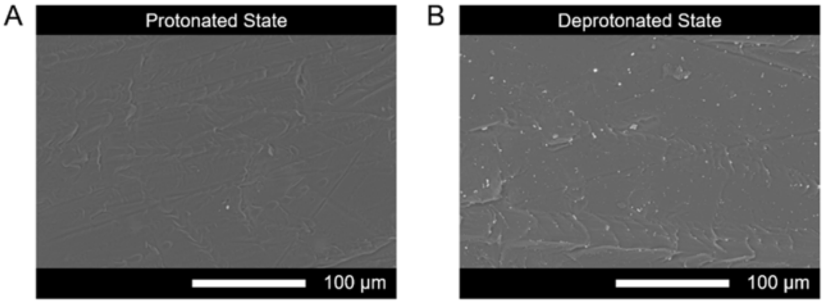

Figure 2-11. SEM images of PVDF-HFP based optode surface in (A) protonated and (B) deprotonated state.

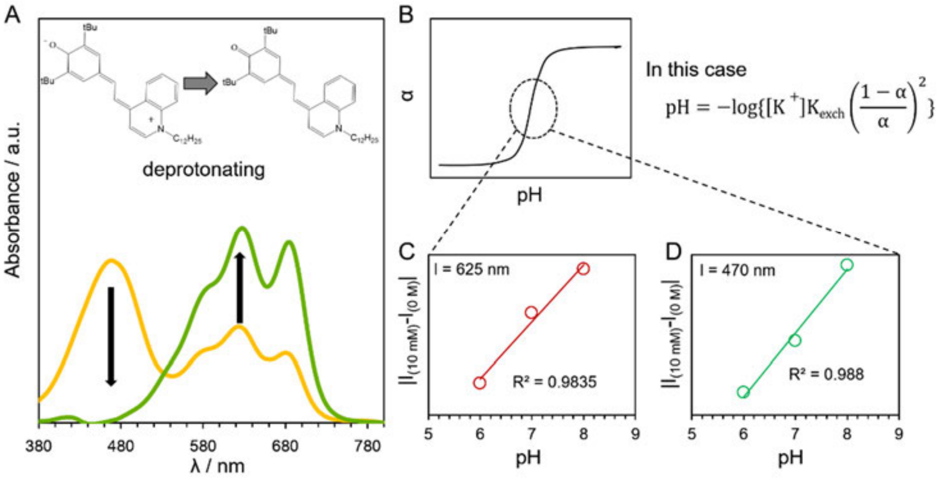

Figure 2-12. (A) Absorption spectra of the dyestuff KD-M13. In protonated state, it is yellow and turns blue upon deprotonation. Spectra were measured by dipping the film into aqueous HCl solution for the protonated state, or in aqueous NaOH solution for the deprotonated state. (B-D) Response curve in the linear region obtained by monitoring the intensity of 10 mM KCl tris-buffer at 470 nm (C) and 625 nm (D) in each pH.

Sensing properties of polymeric bulk optodes. Previously, it has been reported that the intensity of optodes varied according to the surface structure of the polymer surface.[65] In this paper, we have investigated the effect of changing the surface tension of the polymer matrix on sensing performance. **Figure 2-13** shows the sensing property of the K^+ selective membrane where the base polymer was (A and B) PVDF–HFP or (C and D) PVC. The responses lie in the range from 10^{-4} M to 10^{-1} M, which includes the physiological level of K^+ in blood. No apparent difference in the optical response or any shift of absorbance peak was observed between the PVDF-HFP (log K_{exch}=-5.19) and the PVC based optode (log K_{exch}=-5.46), where coupling constant: $K_{exch}=[S_{zO}M_O^{z+}R_O^{z-}][D_O]^z[H_W^+]^z/[M_W^{z+}][S_O]^z[D_OH^+R_O^-]^z$ was determined by the molar ratio of components. Furthermore, there was no apparent change in response velocity. Therefore, the surface tension does not influence on optical response and/or cause shifts in absorption spectra.

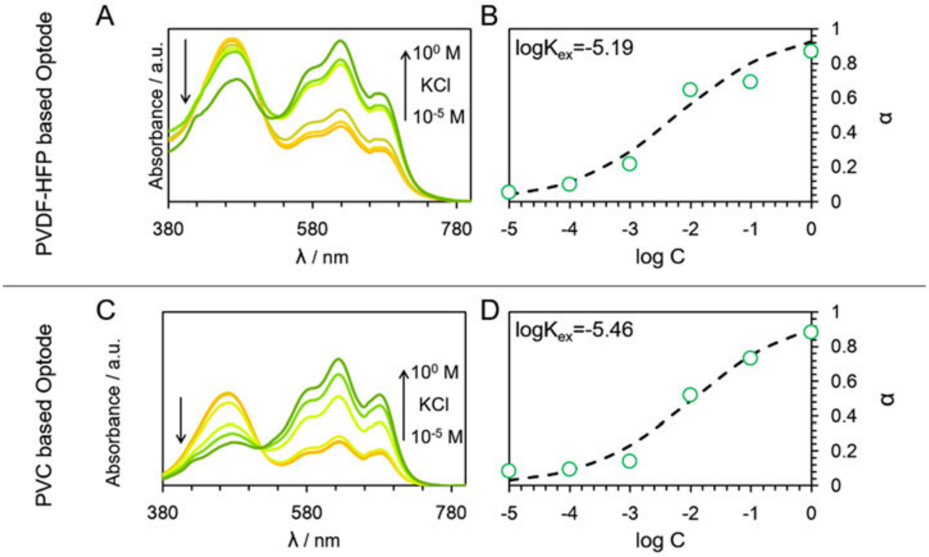

Figure 2-13. Comparison of sensing ability between the PVDF-HFP and PVC based optode. (A) Absorption spectra of the PVDF-HFP based one and (B) the response curve to K^+. (C) Absorption spectra of the PVC based optode and (D) the response curve to potassium ion.

Selectivity of the PVDF-HFP based optode. The selectivity of sensing ability is investigated for the blood potassium level determination in **Figure 2-14**. **Figure 2-14A** shows the response curve of the PVDF-HFP based optode for fluid analytes containing physiologically significant cations chloride salts (K^+, Na^+, Mg^{2+}, Ca^{2+}). Whereas the PVDF-HFP based optode turned blue in 1 M KCl buffer, it maintained its yellow color in 1 M NaCl, $MgCl_2$, or $CaCl_2$ buffer as shown in **Figure 2-14B**. We calculated the coupling constants K_{exch} (**Table 2-2**) and ion selectivities K_{ij}^{opt}, $i = K^+$ (**Table 2-3**) from the response curve; but they could not be calculated accurately for Ca^{2+} and Mg^{2+} since reliable approximations of their response curves could not be obtained. However, the results indicate that the sensor has sufficient selectivity for use in the analysis of blood samples (the ion selectivities required for blood are given in the literature [56]). Here, a linear response was obtained in the range of 10^{-4}-10^{-1} M indicating that the optode is sufficient to be selective to operate a background of other blood electrolytes, and thus suitable for physiological measurement.

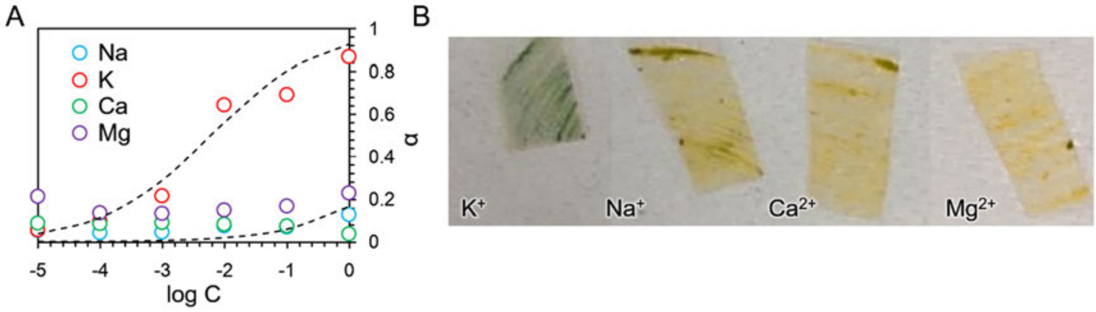

Figure 2-14. Ion selectivity of the PVDF-HFP based optode. (A) Response to NaCl, KCl, $CaCl_2$, and $MgCl_2$. (B) Photographic image of the PVDF-HFP based optodes after immersion in 1 M KCl, NaCl, $CaCl_2$, or $MgCl_2$ aqueous buffer.

Table 2-2. Exchange constants (K_{exch})

Ion	K_{exch}
K	6.47×10^{-6}
Na	1.68×10^{-9}
Mg	Unmeasurable
Ca	Unmeasurable

Table 2-3. Ion selectivity (K_{ij}^{opt}, i = K^{+})

ion	$\log K_{ij}^{opt}$	$\log K_{ij}^{opt}$ (required for 10-fold diluted blood)	$\log K_{ij}^{opt}$ (required for undiluted blood)
Na	-3.59	-3.14	-3.09
Mg	<-3	-0.92	-0.88
Ca	<-3	-1.39	-1.31

Blood fouling resistance. **Figure 2-15A** shows the blood contact angle and sliding angle of each polymer optode. It indicates that the PVDF-HFP based optode (γ_{SV}=25 mN) exhibit superior blood fouling resistance than the PVC (γ_{SV}=39 mN) based optode thanks to the formers higher contact angle and lower sliding angle. The difference of contact angle can be understood by *Young*'s theory. [19] Thanks to the blood adhesion on PVDF-HFP based optode is weaker than that on the PVC based one, the sliding on the former was lower than that on the latter. When a blood droplet slides on the PVC based optode, some small blood contamination remained on the films. For this reason, we measured a color histogram for each polymer optode just after the sliding of a blood as shown in the **Figure 2-15B**, **C**. The red area indicates remaining contaminating blood while the blue colored area indicates where the optode has reacted with blood. The PVC based optode showed the higher blood contamination than the PVDF-HFP based optode, in that the former surface indicated the higher density red peak and the lower density blue intensity than the latter surface.

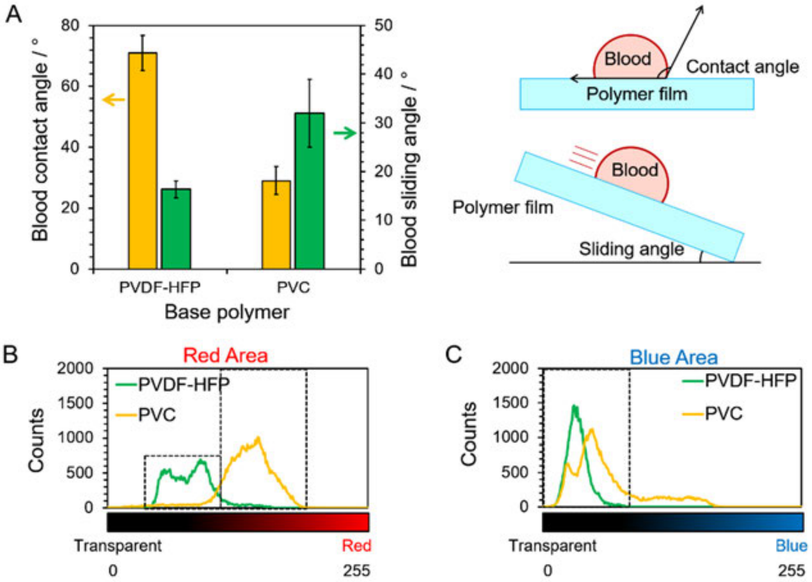

Figure 2-15. Comparison of anti-blood-contamination properties between PVDF-HFP and PVC based optode. (A) Contact angle and sliding angle of 20 μL pig blood on PVDF-HFP or PVC based optode. (B-C) Color histogram for each optode polymer after sliding the blood. (B) Red color area indicates the remaining blood contamination whereas (C) blue color area indicates the reacted area with blood.

Determination of potassium level in human blood. Finally, potassium level in human blood is determined using the PVDF-HFP optode. **Figure 2-16** shows the linear-range response curve obtained by the standard addition method. The potassium level in human blood was determined to be 5.57±0.09 mM. This value is a valid level for human blood. For applying this system to *in situ* determination, we moreover measured the color value change with potassium addition to human blood as shown in **Figure 2-17** and **Table 2-4**. The linear range response in the value *L*, *a*, *b* can be obtained; and hence, it will be helpful to the development of *in situ* determination systems.

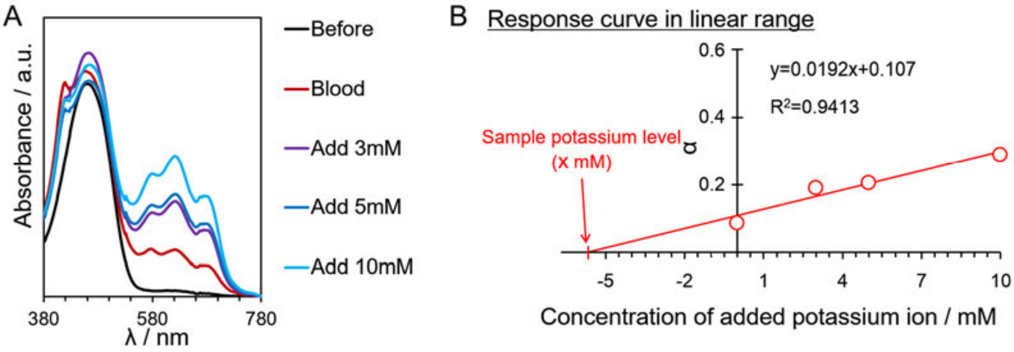

Figure 2-16. Determination of human blood potassium level by a standard addition method. [64] (A) Absorption spectra of before response, blood response, blood with 3 mM KCl added, blood with 5 mM KCl added, and blood with 10 mM KCl added. (B) Response curve of blood with potassium addition for the standard addition method.

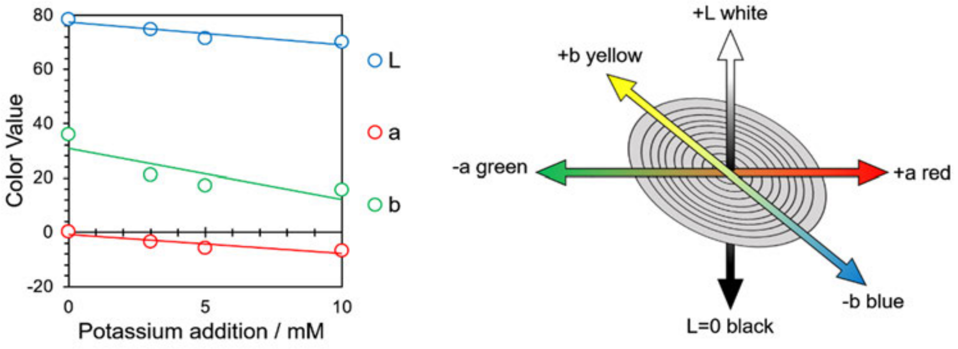

Figure 2-17. Color value change with potassium addition to human blood obtained by *in-situ* measurement using color difference meter. Linear response was obtained for the potassium ion determination as well as the response by UV-vis spectra.

Table 2-4. Color change values with potassium addition in human blood

	L	a	b
Before	88.5	2.5	33.2
Blood	78.4	0.3	35.8
Add 3 mM	74.7	-3.4	21.1
Add 5 mM	71.4	-5.9	17.1
Add 10 mM	70	-6.8	15.6

2.3.4 Conclusions

In conclusion, we developed the ion selective polymeric bulk optode by giving the additional function of blood-fouling resistance. This system will be helpful to the *in situ* and low infection-risk blood analysis in the absence of an electrical supply such as occurs at the time of a natural disaster or in remote locations. Interestingly the lower surface tension base polymer showed the better anti-fouling property whereas having maintained the sensing ability. Our work gives the possibility of improved antifouling properties for the preparation of more effective and versatile polymer bulk optodes. The system also has potential for use in functional analytical systems applied to fouling analyte samples such as polluted water or slime, by selecting the combination of polymer surface tension and sensing media components.

References

[2-1] Jiang, L., Zhao, Y., & Zhai, J. (2004). A lotus-leaf-like superhydrophobic surface: a porous microsphere/nanofiber composite film prepared by electrohydrodynamics. Angewandte Chemie, 116(33), 4438-4441.

[2-2] Kota, A. K., Kwon, G., & Tuteja, A. (2014). The design and applications of superomniphobic surfaces. NPG Asia Materials, 6(7), e109.

[2-3] Blossey, R. (2003). Self-cleaning surfaces—virtual realities. Nature materials, 2(5), 301-306.

[2-4] Lu, Y., Sathasivam, S., Song, J., Crick, C. R., Carmalt, C. J., & Parkin, I. P. (2015). Robust self-cleaning surfaces that function when exposed to either air or oil. Science, 347(6226), 1132-1135.

[2-5] Liu, K., & Jiang, L. (2012). Bio-inspired self-cleaning surfaces. Annual Review of Materials Research, 42, 231-263.

[2-6] Zhang, X., Shi, F., Niu, J., Jiang, Y., & Wang, Z. (2008). Superhydrophobic surfaces: from structural control to functional application. Journal of Materials Chemistry, 18(6), 621-633.

[2-7] Kang, S. M., You, I., Cho, W. K., Shon, H. K., Lee, T. G., Choi, I. S., ... & Lee, H. (2010). One-step modification of superhydrophobic surfaces by a mussel-inspired polymer coating. Angewandte Chemie International Edition, 49(49), 9401-9404.

[2-8] Zhang, W., Lu, X., Xin, Z., & Zhou, C. (2015). A self-cleaning polybenzoxazine/TiO 2 surface with superhydrophobicity and superoleophilicity for oil/water separation. Nanoscale, 7(46), 19476-19483.

[2-9] Yu Wang, Y., & Burke, P. J. (2013). A large-area and contamination-free graphene transistor for liquid-gated sensing applications. Applied Physics Letters, 103(5), 052103.

[2-10] Srinivasan, S., Kleingartner, J. A., Gilbert, J. B., Cohen, R. E., Milne, A. J., & McKinley, G. H. (2015). Sustainable drag reduction in turbulent Taylor-Couette flows by depositing sprayable superhydrophobic surfaces. Physical review letters, 114(1), 014501.

[2-11] Brennan, J. C., Geraldi, N. R., Morris, R. H., Fairhurst, D. J., McHale, G., & Newton, M. I. (2015). Flexible conformable hydrophobized surfaces for turbulent flow drag reduction. Scientific reports, 5, 10267.

[2-12] Lv, J., Song, Y., Jiang, L., & Wang, J. (2014). Bio-inspired strategies for anti-icing. ACS nano, 8(4), 3152-3169.

[2-13] Zhang, Q., He, M., Chen, J., Wang, J., Song, Y., & Jiang, L. (2013). Anti-icing

surfaces based on enhanced self-propelled jumping of condensed water microdroplets. Chemical Communications, 49(40), 4516-4518.

[2-14] Kreder, M. J., Alvarenga, J., Kim, P., & Aizenberg, J. (2016). Design of anti-icing surfaces: smooth, textured or slippery?. Nature Reviews Materials, 1, 15003.

[2-15] PináChen, Y. (2014). Bio-inspired resin acid-derived materials as anti-bacterial resistance agents with unexpected activities. Chemical Science, 5(5), 2011-2016.

[2-16] Zhu, H., Guo, Z., & Liu, W. (2014). Adhesion behaviors on superhydrophobic surfaces. Chemical Communications, 50(30), 3900-3913.

[2-17] Cheng, Y., Lu, S., Xu, W., Wen, H., & Wang, J. (2015). Fabrication of superhydrophobic Au–Zn alloy surface on a zinc substrate for roll-down, self-cleaning and anti-corrosion properties. Journal of Materials Chemistry A, 3(32), 16774-16784.

[2-18] Quéré, D. (2008). Wetting and roughness. Annu. Rev. Mater. Res., 38, 71-99.

[2-19] Young, T. (1805). An essay on the cohesion of fluids. Philosophical Transactions of the Royal Society of London, 95, 65-87.

[2-20] Cassie, A. B. D., & Baxter, S. (1944). Wettability of porous surfaces. Transactions of the Faraday society, 40, 546-551.

[2-21] Wenzel, R. N. (1936). Resistance of solid surfaces to wetting by water. Industrial & Engineering Chemistry, 28(8), 988-994.

[2-22] Forsberg, P. S., Priest, C., Brinkmann, M., Sedev, R., & Ralston, J. (2009). Contact line pinning on microstructured surfaces for liquids in the Wenzel state. Langmuir, 26(2), 860-865.

[2-23] Dai, X., Stogin, B. B., Yang, S., & Wong, T. S. (2015). Slippery wenzel state. ACS nano, 9(9), 9260-9267.

[2-24] Lafuma, A., & Quéré, D. (2003). Superhydrophobic states. Nature materials, 2(7), 457-460.

[2-25] Bird, J. C., Dhiman, R., Kwon, H. M., & Varanasi, K. K. (2013). Reducing the contact time of a bouncing drop. Nature, 503(7476), 385-388.

[2-26] Schutzius, T. M., Jung, S., Maitra, T., Graeber, G., Köhme, M., & Poulikakos, D. (2015). Spontaneous droplet trampolining on rigid superhydrophobic surfaces. Nature, 527(7576), 82-85.

[2-27] Sanchez, C., Arribart, H., & Guille, M. M. G. (2005). Biomimetism and bioinspiration as tools for the design of innovative materials and systems. Nature materials, 4(4), 277-288.

[2-28] Lau, K. K., Bico, J., Teo, K. B., Chhowalla, M., Amaratunga, G. A., Milne, W. I., ... & Gleason, K. K. (2003). Superhydrophobic carbon nanotube forests. Nano

letters, 3(12), 1701-1705.

[2-29] Zhai, L., Cebeci, F. C., Cohen, R. E., & Rubner, M. F. (2004). Stable superhydrophobic coatings from polyelectrolyte multilayers. Nano letters, 4(7), 1349-1353.

[2-30] Cao, L., Jones, A. K., Sikka, V. K., Wu, J., & Gao, D. (2009). Anti-icing superhydrophobic coatings. Langmuir, 25(21), 12444-12448.

[2-31] Marmur, A. (2004). The lotus effect: superhydrophobicity and metastability. Langmuir, 20(9), 3517-3519.

[2-32] Ming, W., Wu, D., van Benthem, R. A. T. M., & De With, G. (2005). Superhydrophobic films from raspberry-like particles. Nano letters, 5(11), 2298-2301.

[2-33] Guo, Z., Zhou, F., Hao, J., & Liu, W. (2005). Stable biomimetic super-hydrophobic engineering materials. Journal of the American Chemical Society, 127(45), 15670-15671.

[2-34] Nakajima, A., Fujishima, A., Hashimoto, K., & Watanabe, T. (1999). Preparation of transparent superhydrophobic boehmite and silica films by sublimation of aluminum acetylacetonate. Advanced Materials, 11(16), 1365-1368.

[2-35] Wang, S., Feng, L., & Jiang, L. (2006). One-Step Solution-Immersion Process for the Fabrication of Stable Bionic Superhydrophobic Surfaces. Advanced Materials, 18(6), 767-770.

[2-36] Sun, T., Wang, G., Feng, L., Liu, B., Ma, Y., Jiang, L., & Zhu, D. (2004). Reversible switching between superhydrophilicity and superhydrophobicity. Angewandte Chemie, 116(3), 361-364.

[2-37] Feng, L., Zhang, Z., Mai, Z., Ma, Y., Liu, B., Jiang, L., & Zhu, D. (2004). A super-hydrophobic and super-oleophilic coating mesh film for the separation of oil and water. Angewandte Chemie International Edition, 43(15), 2012-2014.

[2-38] Verho, T., Bower, C., Andrew, P., Franssila, S., Ikkala, O., & Ras, R. H. (2011). Mechanically durable superhydrophobic surfaces. Advanced Materials, 23(5), 673-678.

[2-39] Feng, L., Li, S., Li, H., Zhai, J., Song, Y., Jiang, L., & Zhu, D. (2002). Super-hydrophobic surface of aligned polyacrylonitrile nanofibers. Angewandte Chemie, 114(7), 1269-1271.

[2-40] Gao, L., & McCarthy, T. J. (2006). A perfectly hydrophobic surface (θA/θR= 180/180). Journal of the American Chemical Society, 128(28), 9052-9053.

[2-41] Nguyen, D. D., Tai, N. H., Lee, S. B., & Kuo, W. S. (2012). Superhydrophobic and superoleophilic properties of graphene-based sponges fabricated using a facile

dip coating method. Energy & Environmental Science, 5(7), 7908-7912.

[2-42] Tenjimbayashi, M., & Shiratori, S. (2014). Highly durable superhydrophobic coatings with gradient density by movable spray method. Journal of Applied Physics, 116(11), 114310.

[2-43] Tenjimbayashi, M., Komatsu, H., Akamatsu, M., Nakanishi, W., Suzuki, K., Hill, J. P., ... & Ariga, K. (2016). Determination of blood potassium using a fouling-resistant PVDF–HFP-based optode. RSC Advances, 6(17), 14261-14265.

[2-44] Jung, Y. C., & Bhushan, B. (2009). Mechanically durable carbon nanotube−composite hierarchical structures with superhydrophobicity, self-cleaning, and low-drag. ACS nano, 3(12), 4155-4163.

[2-45] Zhu, X., Zhang, Z., Men, X., Yang, J., Wang, K., Xu, X., ... & Xue, Q. (2011). Robust superhydrophobic surfaces with mechanical durability and easy repairability. Journal of Materials Chemistry, 21(39), 15793-15797.

[2-46] Yang, C., Tartaglino, U., & Persson, B. N. J. (2006). Influence of surface roughness on superhydrophobicity. Physical review letters, 97(11), 116103.

[2-47] Wang, F., Wang, X., Xie, A., Shen, Y., Duan, W., Zhang, Y., & Li, J. (2012). A simple method for preparation of transparent hydrophobic silica-based coatings on different substrates. Applied Physics A, 106(1), 229-235.

[2-48] Luo, C., & Xiang, M. (2012). Angle inequality for judging the transition from Cassie–Baxter to Wenzel states when a water drop contacts bottoms of grooves between micropillars. Langmuir, 28(38), 13636-13642.

[2-49] Seiler, K., & Simon, W. (1992). Theoretical aspects of bulk optode membranes. Analytica chimica acta, 266(1), 73-87.

[2-50] Zhang, L., Chen, S., Zhao, Q., & Huang, H. (2015). Carbon dots as a fluorescent probe for label-free detection of physiological potassium level in human serum and red blood cells. Analytica chimica acta, 880, 130-135.

[2-51] Dillon, J. J., DeSimone, C. V., Sapir, Y., Somers, V. K., Dugan, J. L., Bruce, C. J., ... & Scott, C. G. (2015). Noninvasive potassium determination using a mathematically processed ECG: Proof of concept for a novel “blood-less, blood test”. Journal of electrocardiology, 48(1), 12-18.

[2-52] Hollander-Rodriguez, J. C. & Calvert, J. F. (2006). Hyperkalemia. Am. Fam. Physician, 73, 283–290.

[2-53] Fassel, V. A., & Kniseley, R. N. (1974). Inductively coupled plasma. Optical emission spectroscopy. Analytical Chemistry, 46(13), 1110A-1120A.

[2-54] Harrison, D. J., Fluri, K., Seiler, K., Fan, Z., Effenhauser, C. S., & Manz, A. (1993). Micromachining a miniaturized capillary electrophoresis-based chemical

analysis system on a chip. Science, 261, 895-895.

[2-55] Suzuki, K., Yamada, H., Sato, K., Watanabe, K., Hisamoto, H., Tobe, Y., & Kobiro, K. (1993). Design and synthesis of highly selective ionophores for lithium ion based on 14-crown-4 derivatives for an ion-selective electrode. Analytical Chemistry, 65(23), 3404-3410.

[2-56] Xie, L., Qin, Y., & Chen, H. Y. (2013). Direct fluorescent measurement of blood potassium with polymeric optical sensors based on upconverting nanomaterials. Analytical chemistry, 85(5), 2617-2622.

[2-57] Bakker, E., Bühlmann, P., & Pretsch, E. (1997). Carrier-based ion-selective electrodes and bulk optodes. 1. General characteristics. Chemical Reviews, 97(8), 3083-3132.

[2-58] Bühlmann, P., Pretsch, E., & Bakker, E. (1998). Carrier-based ion-selective electrodes and bulk optodes. 2. Ionophores for potentiometric and optical sensors. Chemical Reviews, 98(4), 1593-1688.

[2-59] Newman, E. T., Watters, T. S., Lewis, J. S., Jennings, J. M., Wellman, S. S., Attarian, D. E., ... & Bolognesi, M. P. (2014). Impact of perioperative allogeneic and autologous blood transfusion on acute wound infection following total knee and total hip arthroplasty. J Bone Joint Surg Am, 96(4), 279-284.

[2-60] Aziz, A. A. A., Mohammed, S. F., & El Gamel, M. M. (2014). Development of an Optode for Detection of Trace Amounts of Hg2+ in Different Real Samples Based on Immobilization of Novel Tetradentate Schiff Bases Bearing Two Thiol Groups in PVC Membrane. Journal of fluorescence, 24(3), 859-874.

[2-61] Shamsipur, M., Poursaberi, T., Hassanisadi, M., Rezapour, M., Nourmohammadian, F., & Alizadeh, K. (2012). A new chelation induced enhanced fluorescence-type optical sensor based on parared immobilized in a plasticized PVC membrane for selective determination of Zn (II) ions. Sensors and Actuators B: Chemical, 161(1), 1080-1087.

[2-62] Okada, I., & Shiratori, S. (2014). High-transparency, self-standable Gel-SLIPS fabricated by a facile nanoscale phase separation. ACS applied materials & interfaces, 6(3), 1502-1508.

[2-63] Hisamoto, H., Tani, M., Mori, S., Yamada, T., Ishigaki, T., Tohma, H., & Suzuki, K. (1999). Molecular Design, Characterization, and Application of Multiinformation Dyes (MIDs) for Optical Chemical Sensings. 3. Application of MIDs for λmax-Tunable Ion-Selective Optodes. Analytical chemistry, 71(1), 259-264.

[2-64] Wang, K., Seiler, K., Morf, W. E., Spichiger, U. E., Simon, W., Lindner, E., & Pungor, E. (1990). Characterization of Potassium-Selective Optode Membranes

Based on Neutral lonophores and Application in Human Blood Plasma. Analytical sciences, 6(5), 715-720.

[2-65] Bychkova, V., & Shvarev, A. (2009). Surface area effects on the response mechanism of ion optodes: a preliminary study. Analytical chemistry, 81(17), 7416-7419.

Chapter 3 Selective-wetting materials biologically inspired by predation mechanism of a spider *Uloborus Walckenaerius*

This chapter is based on [Tenjimbayashi, M., Sasaki, K., Matsubayashi, T., Abe, J., Manabe, K., Nishioka, S., & Shiratori, S. (2016). A biologically inspired attachable, self-standing nanofibrous membrane for versatile use in oil–water separation. Nanoscale, 8(21), 10922-10927.]

3.1 Selective wetting properties

In this chapter, selective-wetting porous materials biologically inspired by predation of a spider are introduced. Selective wetting surfaces which are wet by a liquid whereas de-wet against the other liquid, have recently been well researched because of the potential application for separation filter. [1] Liquid surface tension, and interfacial tension with surface etc., are different according to liquid kinds; thus, contact angle depends on liquid kinds, too. The difference of contact angles can become larger with surface morphology such as surface roughness and liquid-solid interactions to lead the liquid dependent wetting with Cassie-Baxter state or Wenzel state as shown in **Figure 3-1**. [2] Especially, porous materials with controlled morphology and/or surface chemistry perform selective wettability in extreme because the wetting behaviors are divided into two states. The one state is *Cassie-Baxter* state in which liquid droplets do not come into the pores to show high contact angle; the other state is *Wenzel* state in which liquid droplets penetrate among the pores to show contact angle being 0°. The wetting/de-wetting threshold (WT) are decided by the robustness factor A^*, which is the ratio of breakthrough pressure $P_{breakthrough}$ and a reference pressure $P_{ref} = 2\gamma_{LV}/l_{cap}$, where $l_{cap} = (\gamma_{LV}/\rho g)^{0.5}$ is capillary length for the liquid, γ_{LV}, ρ, and g are the liquid surface tension, density, and gravity acceleration constant. [3] Because the reference pressure is close to the minimal value of millimetric droplets' keeping air-solid-liquid interface (Cassie state), [4] the porous material with $A^* \gg 1 \Leftrightarrow P_{breakthrough} - P_{ref} \gg 0$ prevents the liquid from penetration (**Figure 3-2A**) whereas the material with $A^* \leq 1 \Leftrightarrow P_{breakthrough} - P_{ref} \leq 0$ let the liquid penetrate on it (**Figure 3-2B**).

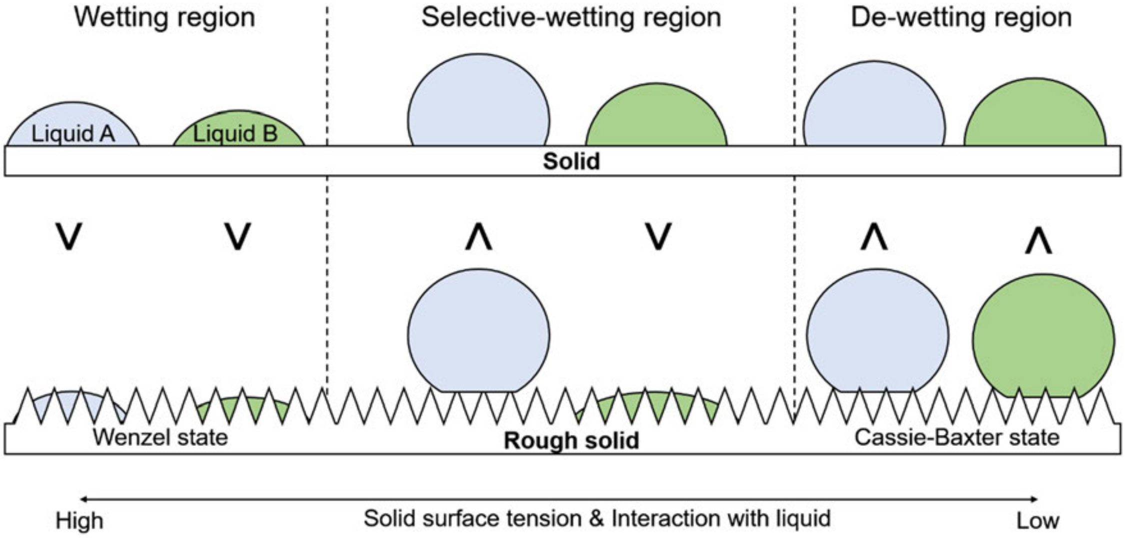

Figure 3-1. Schematic illustration of strategy for enhancing selective wettability. The control of surface-liquid interaction and surface roughness can contact liquid A with *Cassie-Baxter* state and liquid B with *Wenzel* state at the same time.

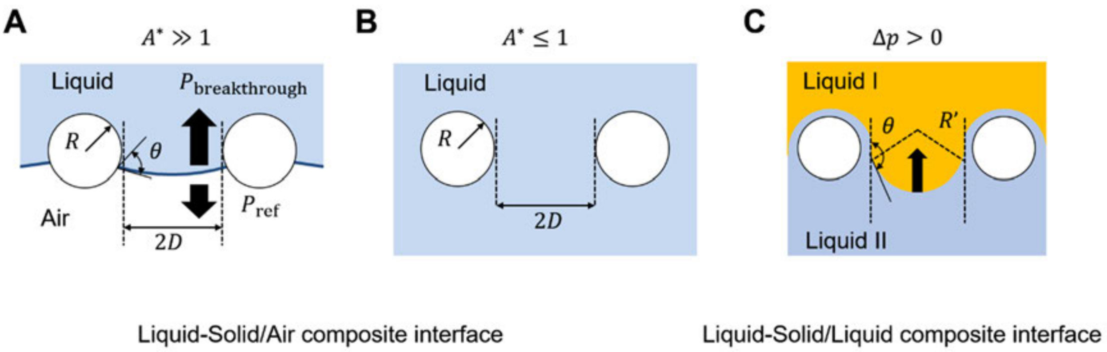

Figure 3-2. Schematic illustration of liquid wetting behaviors on a porous material. (A) Liquid fail to penetrate into the porous material with the robustness factor $A^* \gg 1$. Here, R is a cylinder radius and 2D is an inter-cylinder space. (B) Liquid penetrate the porous material with $A^* \leq 1$. (C) Liquid I fail to penetrate the porous material due to the existence of liquid II with *Young-Laplace* pressure $\Delta p > 0$. Here, R' is a radius of a curvature of liquid I at inter-cylinder space.

The above discussion was based on the independent wetting behavior on solid/air composite materials. However, in case the two kinds of immiscible liquid contacts with the surface, we have to consider the liquid-liquid-solid system. When the liquid mixture comes into contact with the porous material, the liquid wetting behaviors are divided into two states: (i) both liquid I and liquid II penetrate on the surface as shown in Figure 1A, and (ii) the liquid I-liquid II interface is formed as shown in **Figure 3-2C**. In the latter case, the liquid I is prevented from the penetration by the liquid II which wets to fill the pores. The interfacial pressure between liquids: *Young-Laplace* pressure Δp is given by: $\Delta p = 2\gamma_{I-II}/R' = -l_c(\cos\theta)/S$ where γ_{I-II} is liquid-liquid interfacial tension, R' is radius of curvature of the meniscus, and S is pore area. In any case, the wetting behaviors are selectively controlled by solid-liquid-air interfacial tension, surface morphology, and capillary.

From these backgrounds, various selective wetting materials are introduced, which are categorized by hydrophobic/oleophilic materials, [6-10] hydrophilic/underwater-oleophobic type, [11-14] hydrophilic/oleophobic type, [3] dual-phobic (incorporates hydrophilic/underwater-oleophobic and oleophilic/underoil-hydrophobic) type [15, 16], selective oleophobic/oleophilic type [2], smart switching type [17-20], and some exception [21-23]; their applications are mostly separation filter membranes. Even though the both theoretical and practical development of this fields enabled highly efficient liquid separation including emulsion with high flux, there still remains the challenges for practice including low selectivity of materials, low formability, high cost, complex process, and large-scale fabrication. [24] In section 3-2, we introduce an attachable self-standing nanoweb sheet inspired by an impeding mechanism of a spider *Uloborus Walckenaerius*, whose web can capture any insect using electrostatic force; the sheet can be attached to the various materials to give them a hydrophobic/oleophilic property. The versatility of this material will be helpful for the practice in industry of selective wetting materials.

3.2 Design of Hydrophobic/Superoleophilic nanofibrous film for effective oil/water separation

3.2.1 Introduction

As represented by 2010 Deepwater Horizon oil spill accident in the Gulf of Mexico, oil pollution in water is a worldwide problem. [25] It causes long-term negative effects on the health of living organisms and the environment. [26] However, high purity oil is an important energy resource for human lifestyle. [27] The refuse disposal systems currently available for industrial effluents from factories or for burning rubbish are both expensive and time consuming. [28] Therefore, it is important to develop methods for the extraction of oil from water. [29]

Recent approaches to separate oil and water are based on the selective wetting of them onto 2D or 3D porous materials. [30] Various approaches to design selective wetting materials are reported to separate oil-water mixtures, emulsions, and chemical components. [6-20, 28-31] For example, Dong et al. reported superhydrophilic and underwater superoleophobic membranes by coating graphene oxide to meshes. [14] Yang and co-workers reported oil absorbent by coating melamine sponge with lignin. [31] In these approaches, the materials designed for oil-water separation need to make use of both 2D and 3D structured porous solids with a specific supporting body. Thanks to the development of selective wetting materials, this technology has already achieved the highly effective and continuous separation of oil from mixtures and emulsions using strategies of oil-water filtration, [13-15] oil absorption, [31, 32] and oil collection [33, 34] The remaining challenges of oil-water separation are: (i) adding other functions such as transparency, [7] durability, [33] self-healing [35] and a stimuli-response [21, 36]; (ii) working under special conditions i.e. at different pressures, [13] or at different temperatures, [37] or in the presence of other chemicals; [2] and (iii) making this technology scalable, facile, and low cost. [2, 38] The last requirement, especially, is essential in practical use of this technology. Hence, we aimed to develop a scalable, facile, and low-cost material that could be applied to both 2D and 3D structured porous supporting bodies for oil-water separation techniques.

Our strategy is to design a self-standing sheet with selective-wettability that can be attached to various materials to provide this function to both 2D and 3D materials. However, this type of versatile attachment is difficult to design because the conventional approach to this requires chemical bonding or physical cross-linking between the supporting material and the coating material.

Here, nature offers a remarkably simple alternative idea. The spider *Uloborus walckenaerius* weaves an electrically charged thread into fluffed nanofibers from individual spigots using specialized comb on its legs; the webs capture flying insects by electrostatic van der Waals forces (**Figure 3-3A**). [39, 40] Inspired by the capture mechanism, we designed an attachable self-standing nanofiber sheet (NF-S) using the easily chargeable fluorine polymer Poly(vinylidene fluoride-*co*-hexafluoropropylene) (PVDF-HFP) as shown in **Figure 3-3B, C**. Thanks to the electrostatic van der Waals forces, the NF-S can attach to various materials as shown in **Figure 3-3D-G**. The strategy provided oil-water separation ability to both 2D and 3D materials. [41] In addition, the scalability, versatility and low cost fabrication of the NF-S will contribute to the practical use of oil-water separation. Also, the concept of attaching the function to various materials gives new insight into the development of functional materials.

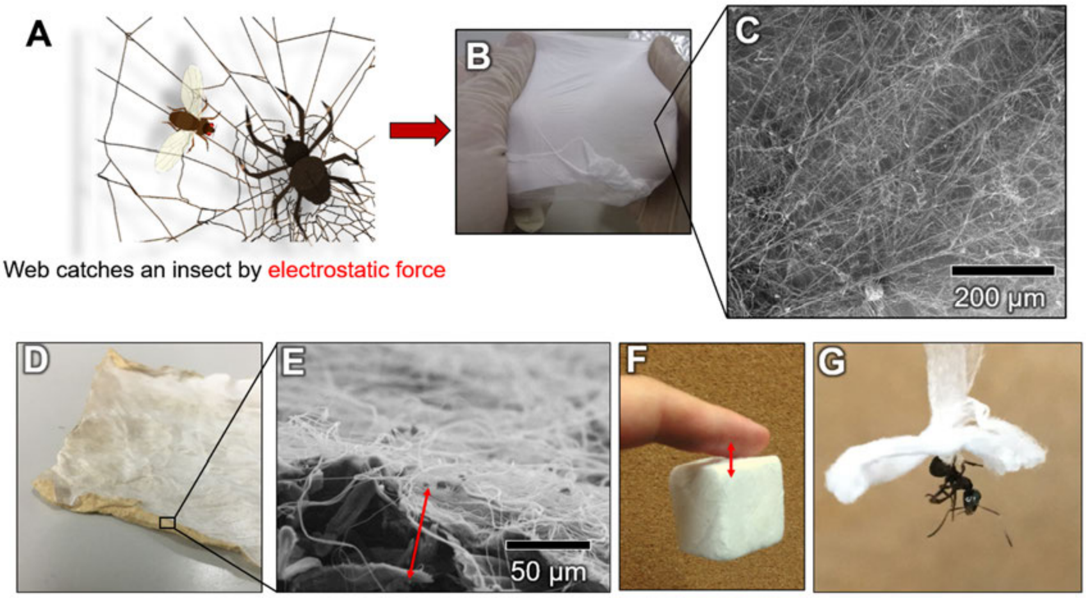

Figure 3-3. Biomimetics of *Uloborus walckenaerius* spider web to design an attachable self-standing NF-S. (A) Schematic image of the predation mechanism of *Uloborus walckenaerius*. (B) Photo-image and (C) SEM image of an attachable self-standing NF-S. (D) Attachment of a NF-S to a Kimtowel and (E) its magnified image. (F, G) Attachment of a NF-S block to (F) a finger and (G) an insect.

3.2.2 Experimental

Materials. PVDF-HFP ($((\text{-CH}_2\text{CF}_2\text{-})_m[\text{-CF}_2\text{CF(CF}_3)\text{-}]_n$, M_w ~400,000, M_n ~130,000, m:n = 10:1 (molar ratio)) was purchased from Sigma-Aldrich (St. Louis, MO, USA). Ethyl-alpha-cyanoacrylate (Et-CA, Alonalpha 201, $\text{NCCH}_2\text{COOEt}$, purity > 99 % with 2,2'-methylenebis(6-tert-butyl-4-methylphenol) < 0.2 %) was kindly provided from Toagosei Co., Ltd. (Tokyo, Japan). Both polymers, which mainly consisted of a nanofibers sheet, were biocompatible, fulfilling the “Food and Drug Administration” standard. Acetone (CH_3COCH_3), toluene (Ph-CH_3), hexadecane ($\text{C}_{16}\text{H}_{34}$), *n*-dodecane ($\text{C}_{12}\text{H}_{26}$), decane ($\text{C}_{10}\text{H}_{22}$), and oleic acid ($\text{CH}_3(\text{CH}_2)_7\text{CH=CH}(\text{CH}_2)_7\text{COOH}$) were purchased from Kanto Chemical Co., Inc. (Tokyo, Japan). Gasoline (grade: 90-91 octane) was purchased from a gas station. Ultrapure water was obtained using an Aquarius GS-500 (CPW, Advantec Co., Saijo, Japan) and dyed with Brilliant Blue (Tokyo Chemical Industry Co., Ltd., Tokyo, Japan). Melamine sponges, poly(vinylchroride) tubes (PVC tubes), and aluminum foil were purchased from a supermarket. Plastic syringes (Volume ~20 mL) and needles (21G ½) were purchased from Terumo Co. (Tokyo, Japan).

Fabrication of a PVDF-HFP/Et-CA nanofibers sheet. **Figure 3-4** summarizes the designing procedure of various oil-water separating devices. The NF-S was designed by an electrospinning method. PVDF-HFP (1 g) and Et-CA (0.1 g) were dissolved in acetone (3.9 g) by stirring for 24 h at 60 °C. The solution was loaded into a plastic syringe with needles. The vertical tip-to-collector distance between the tip of the nozzle and the aluminum foil (used as a collector) was 20 cm. The applied voltage was set at 20 kV by a high voltage power unit. The flux of the syringe pump was set at 3 mL/h. The nanofibers collection area was about 450 cm^2. The electrospinning time was 2400 s and the weight change before and just after electrospinning was 3.0 g. The electrospun nanofibers on the aluminum foil were dried for one day. The designed NF-S was easily peeled from the aluminum foil. The self-standing NF-S was attached to a melamine sponge, glass container, or PVC tube. Furthermore, we found that the NF-S was able to be attached to materials firmly and closely by wetting the NF-S using isopropanol (IPA, $CH_3CH(OH)CH_3$). When wetted with IPA, the NF-S become sticky, and after drying it was firmly attached to the materials.

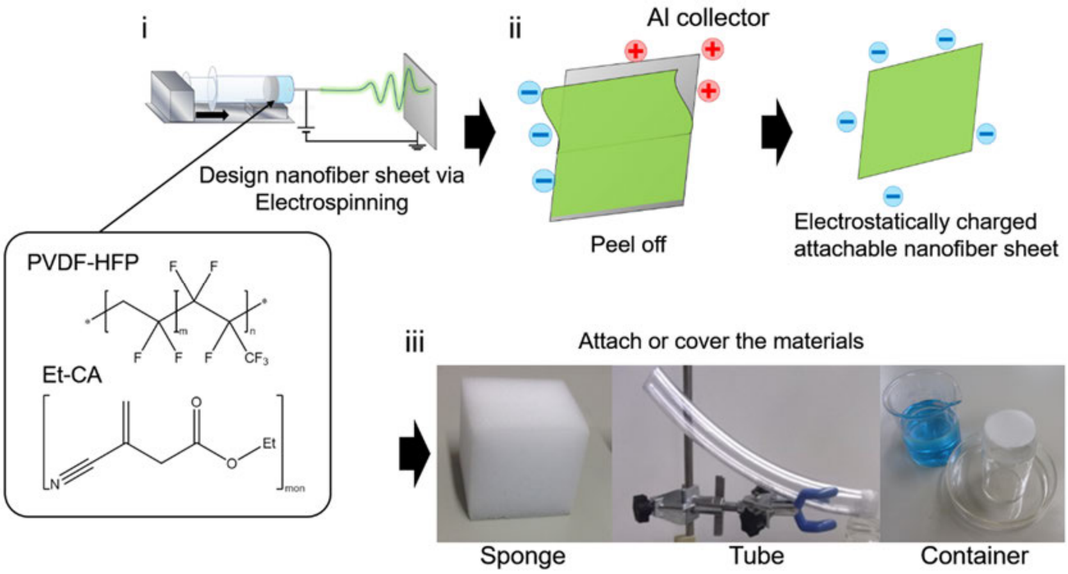

Figure 3-4. Schematic images of the designing procedure. i. The design of the NF-S using an electrospinning method. ii. Peeling the NFs-S from the aluminum foil, which allows the NF-S to become self-standing and negatively charged. iii. The self-standing NF-S was attached to a melamine sponge for oil absorption, to the tip of PVC tube for oil-water separation by filtration, and to a container for oil collection.

Characterization. The morphology of the NF-S was measured by field emission scanning electron microscopy (FE-SEM, Miniscope® TM3030Plus; Hitachi, Japan) with an applied voltage of 15.0 kV; all samples were coated with osmium before observation. The surface chemical components of the NF-S were analyzed by energy-dispersive X-ray spectrometry (EDX, QUANTAX 70; Bruker Nano GmbH, Berlin, Germany). Fiber diameter distributions in the NF-S were obtained by SEM images using the Image J software (U. S. National Institutes of Health, Bethesda, Maryland, USA). The elastic force and extension rate of the NF-S were evaluated by using TRAPEZIUM LITE (Shimadzu Co., Ltd., Kyoto, Japan). The contact angles of the liquids on the NF-S were measured by a commercial contact angle system (FACE; Kyowa Interface Science Co., Ltd., Niiza, Japan). Each static contact angle measurement was performed using 10 μL liquid droplets at room temperature (20 °C) (n = 5 for each sample surface). The wetting processes on the NF-S at room temperature were observed by time-resolved images of the 10 μL casting liquid droplets on the NF-S monitored by a high-speed camera (HAS-D3, Ditect, Tokyo, Japan). The separation efficiency for the oil-water mixtures was calculated by the following equation: $\text{Separation efficiency} / \% = \frac{w_{\text{water}}}{w_{\text{water}}+w_{\text{oil}}} \times 100$ where w_{water} and w_{oil} are the weight of water and oil that remained in the PVC tube, respectively (n = 3 for each oil on NF-S). The flux of the penetrating oil on the NFs-S was calculated by the following equation: $\text{Flux} / \text{Lh}^{-1}\text{m}^{-2} = \frac{V_{\text{penetration}}}{t_{\text{penetration}} \times A_{\text{sheet}}}$ where $V_{\text{penetration}}$ is the volume of penetrated oil on the NF-S, $t_{\text{penetration}}$ is the time of oil penetration, and A_{sheet} is an area of the NF-S that was penetrated by the oil. To mitigate the influence of gravity on the flux, the penetrating oil was cast in small volumes that just covered the whole surface of the NF-S. The mechanical strength of the melamine sponge covered by the NF-S was evaluated by cycles of compression and release using pressing equipment (AH-2003, AS ONE Co., Osaka, Japan). The intervals between compression and release were within 30 seconds at room temperature.

3.2.3 Results and Discussion

Characterization of the NF-S. The NF-S was fabricated by electrospinning a PVDF-HFP/Et-CA mixture on the aluminum collector. The thickness of the NF-S was approximately 135 μm (see **Figure 3-5**) and estimated cost was US$ 0.88 m^{-2} (see **Table 3-1**). The NF-S is self-standing and stretchable (**Figure 3-3B**) whose maximum strain was about 250% at a stress >1 MPa (**Figure 3-6A**) The fracture behavior of the NF-S in a strain-stress test was gradual, meaning the thinner fibers within the sheet fractured first, then thicker fibers, resulting in a gradual decrease in the stress at strains >250%. The fiber diameter was 0.972±0.344 µm whose distribution ranged from 0.3 to 2.5 µm (**Figure 3-6B**). Thus, the mixture of nano- and micro-fibers contributed the strength of the NF-S. The surface area determined by the Brunauer-Emmett-Teller method was 1.1173±0.1037 m^2/g (see **Figure 3-6C** for calculation).

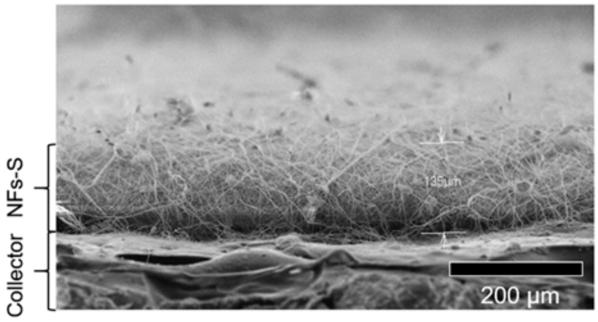

Figure 3-5. Cross-sectional SEM images of the NF-S. The thickness of the NF-S is 135 µm.

Table 3-1. The cost of materials for fabrication of the NF-S. All costs were taken from Sigma-Aldrich (St. Louis, MO, USA) HP at http://www.sigmaaldrich.com (accessed on 22 January 2016).

	Weight / g m^{-2}	Cost / \$ g^{-1}	Cost / \$ m^{-2}
PVDF-HFP	0.40	0.479	0.19160
Et-CA	0.04	15.450	0.61800
Acetone	1.56	0.049	0.07644
Total	-	-	0.88604

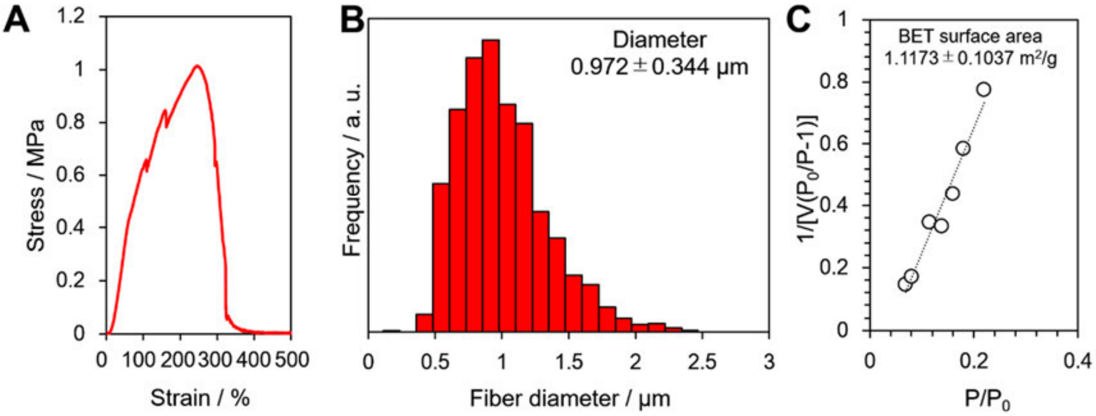

Figure 3-6. (A) The NF-S strength and elastic properties. (B) Distribution of fiber diameter in the NF-S. (C) BET fit for the N_2 adsorption isotherm of the NF-S.

Surface chemistry of the NF-S was analyzed using EDX as shown in **Figure 3-7**. The NF-S was composed of PVDF-HFP (hydrogen, carbon, and fluorine) and Et-CA (hydrogen, carbon, nitrogen, and oxygen). Et-CA was added to adjust wettability strength and elastic properties. The EDX mapping in **Figure 3-7A** showed carbon, nitrogen, oxygen, and fluorine peaks, indicating the presence of PVDF-HFP and Et-CA. The atomic ratio of nitrogen to oxygen was about 1:2 which means the fibers included Et-CA (**Table 3-2)**. The elemental distribution confirmed that the PVDF-HFP and Et-CA was mixed in the fiber (**Figure 3-7B**).

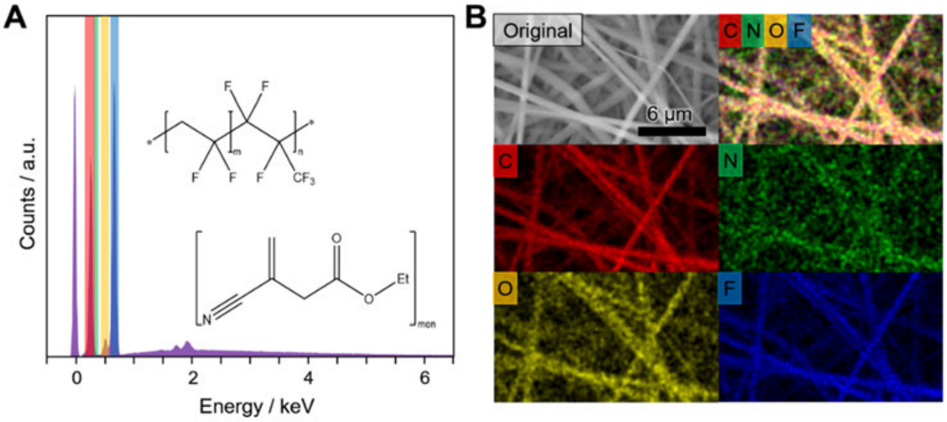

Figure 3-7. (A) Elemental composition and (B) elemental distribution of carbon, nitrogen, oxygen, fluorine, and overall distribution of the NF-S.

Table 3-2. Weight and atomic ratio of the NF-S elemental composition.

	Weight ratio	Atomic ratio	Error range
C	0.462	0.568	0.048
N	0.023	0.024	0.003
O	0.047	0.044	0.006
F	0.468	0.364	0.046

Selective-wettability of the NF-S. The NF-S was characterized by a selective wettability for oil-water separation. We studied the water blocking and oil penetration mechanisms for the NF-S in detail (**Figure 3-8**). Water blocking ability of the NF-S was tested for the bare NF-S (i), toluene infused NF-S (ii), and hexadecane infused NF-S (iii). Under any condition, the water droplets did not penetrate the surface to show apparent contact angle (**Figure 3-8B**). Conversely, both toluene and hexadecane droplet penetrated the NF-S to perform superoleophilicity (iv, v, and **Figure 3-8C**). The WT were investigated by measuring the contact angle of various water/ethanol mixtures as shown in **Figure 3-8D**. [42] The WT of the NF-S exists at a surface tension in the range of 36.09-38.56 mN m^{-1}.

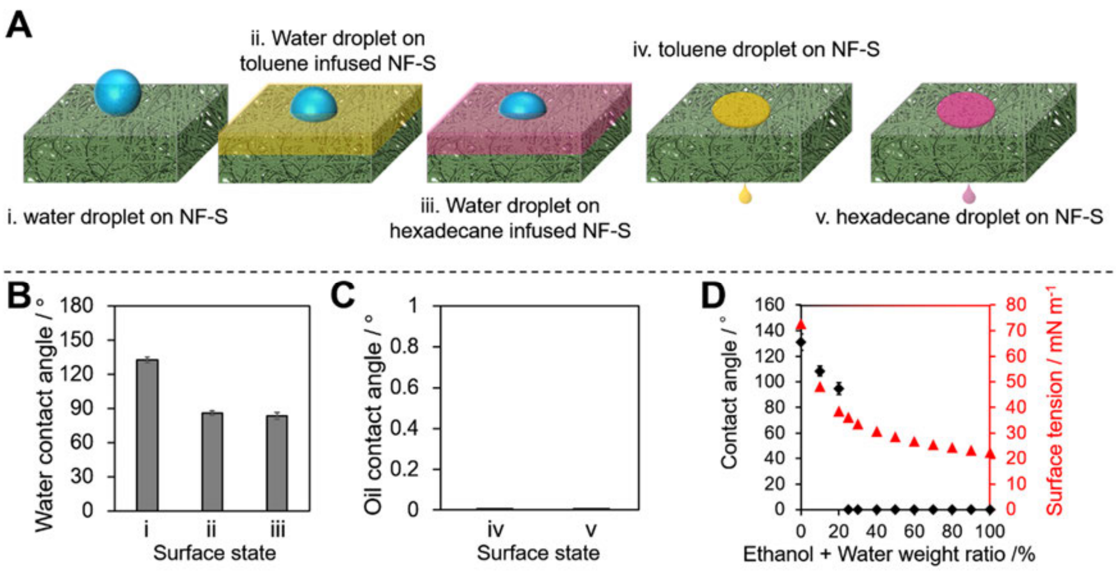

Figure 3-8. Wetting behaviors of water and oils on the NF-S. (A) Schematic illustrations of a water droplet on: (i) the NF-S; (ii) a toluene-infused NF-S; and (iii) hexadecane-infused NF-S; and (iv) a toluene droplet and (v) a hexadecane droplet on the NF-S. (B) Water contact angle on (i)-(iii). (C) Oil contact angles of (iv) and (v). (D) The contact angles and surface tensions (20 °C) for an ethanol-water mixture. [42] The limit for wetting or repelling is at a surface tension in the range of 36.09-38.56 mN m^{-1}.

Then dynamic wetting behaviors of oil and water on the NF-S were investigated in **Figure 3-9**. Water droplet on the pristine NF-S showed the highest hydrophobicity (**Figure 3-9B**). In case (i)-(iii), water droplets blocked their penetration. In case (ii) and (iii), we found that an oily layer formed on the NF-S surface and blocked water invasion as a result of immiscibility of oil and water as shown in **Figure 3-9C**. [43] **Figure 3-9D** indicates most of the oil penetrated the surface but some of the oil remained on the surface to form liquid layer immobilized by the capillary force of the NF-S, which allowed oil-water separation.

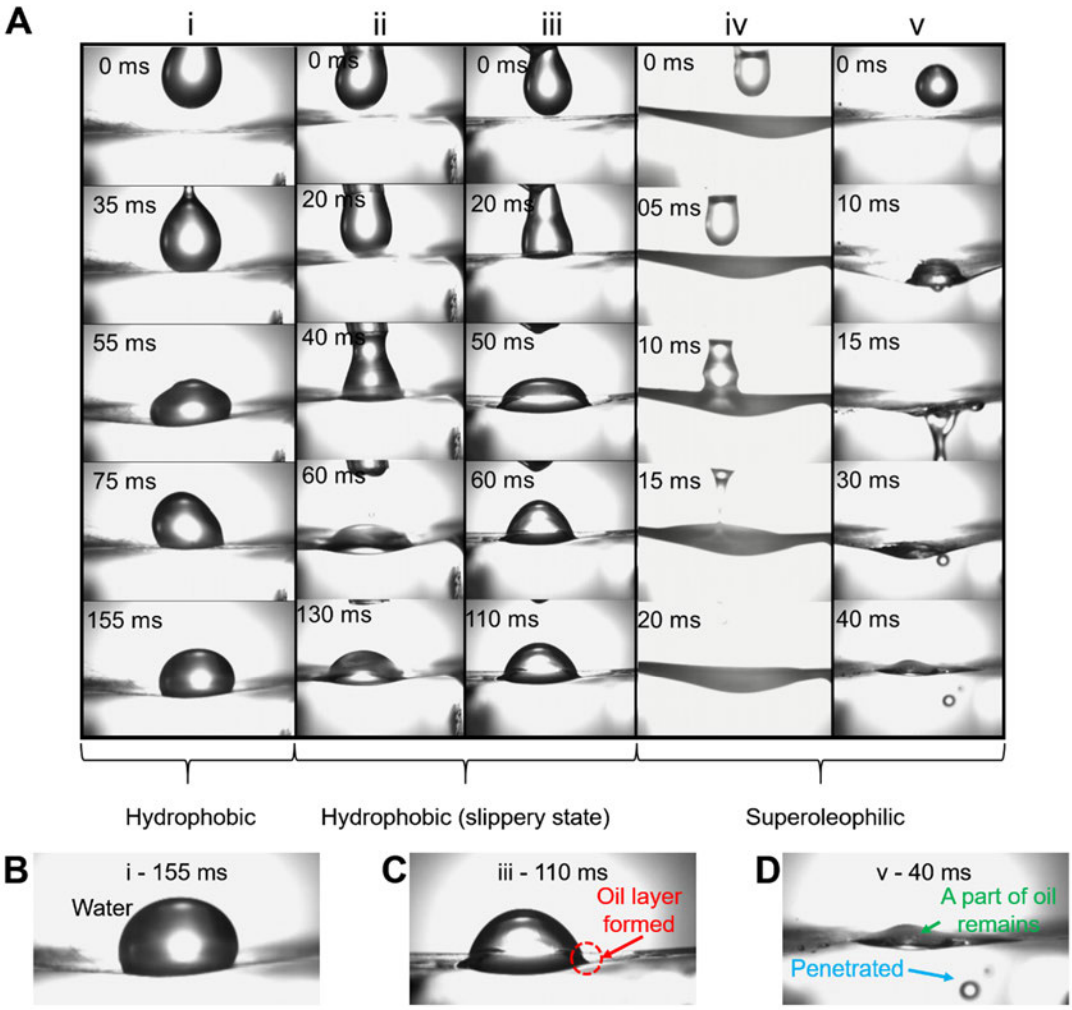

Figure 3-9. Dynamic wetting behaviors water and oil on the NF-S. (A) Time-lapsed images (i)-(iv) and (B)-(D) selected magnified images.

Application of the NF-S. We applied the NF-S to three types of applications; oil absorption, oil-water separation, and oil collection. The oil absorbent was fabricated by covering a melamine sponge with the NF-S (sponge + NF-S) as shown in **Figure 3-10A**. Even though the melamine sponge is naturally omniphilic, the surface of the sponge + NF-S performed the hydrophobicity and oleophilicity at the same time shown in **Figure 3-10B**. The oil absorbent was used in processes (i)-(iii) in **Figure 3-10C**. The merit of the combination of sponge + NF-S is that the absorbed oil can be easily extracted for re-use, whereas other oil absorption methods require more complex extraction processes such as heating. [31, 32] This feature comes from the flexibility of the NF-S and melamine sponge. The NF-S maintained its structure after oil extraction (**Figure 3-11**) to realize repeatable oil absorption and extraction without deterioration (**Figure 3-10D**) with high absorption capacity for various types of oil as shown in **Figure 3-10E**. We also conducted a compression test to determine the 3D structural retention, which performed the high stability of the sponge structures as shown in **Figure 3-10F**, thanks to the natural properties of the melamine sponge. Thus, we attached a selective wetting function to the sponge, which already had stable liquid storage properties and high compression durability. This is new insight into materials functionalization, that is, an example of an addition of function to an already functional material to create an advanced material.

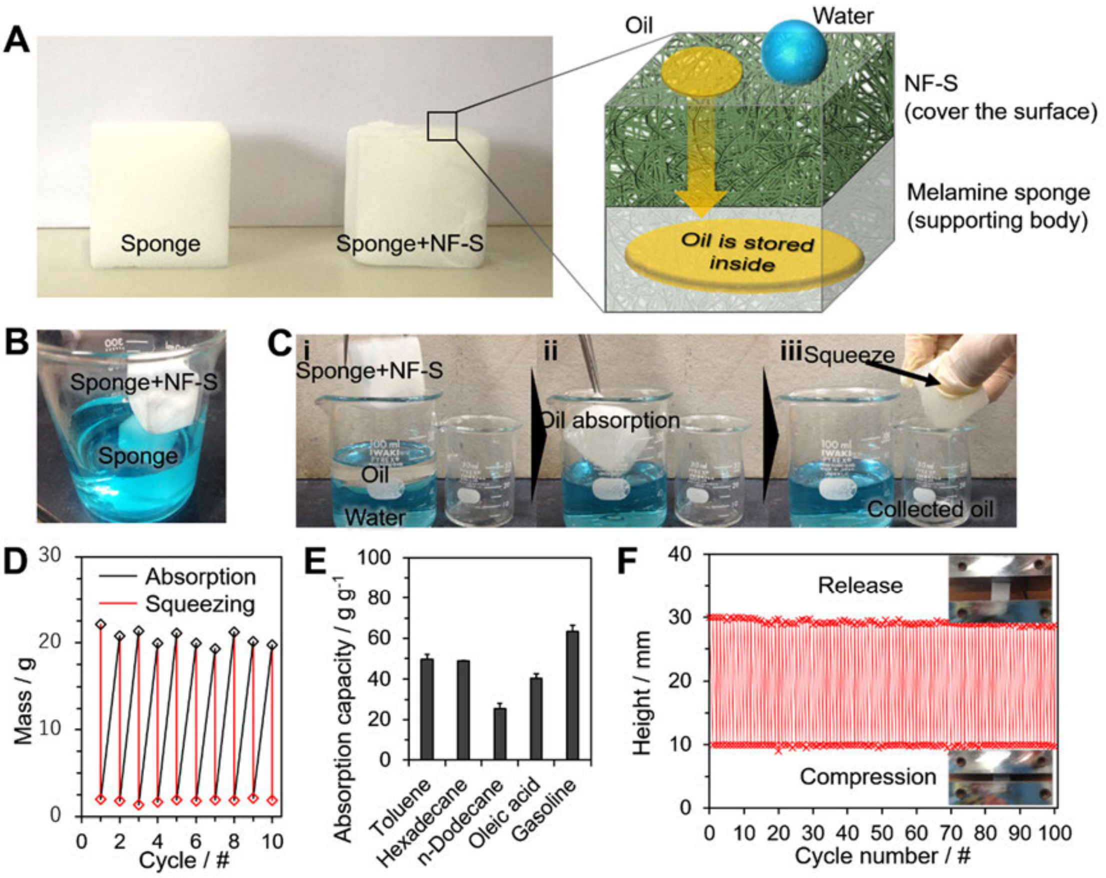

Figure 3-10. Application of the NF-S to oil absorbent. (A) A photo-image of an uncoated

melamine sponge (sponge) and the NF-S attached melamine sponge (sponge + NF-S) with a schematic image of the magnified oil absorbents. (B) A photo-image of the samples in a beaker half-fulfilled with dyed water. (C) Photo-images of the sponge + NF-S being used in separating oil in processes (i)-(iii). (D) Mass change of toluene inside the sponge with cycles of absorption and squeezing. (E) Absorption capacities for the oil-water mixtures with different types of oil. (F) Cyclical pressing measurements for the sponge + NF-S.

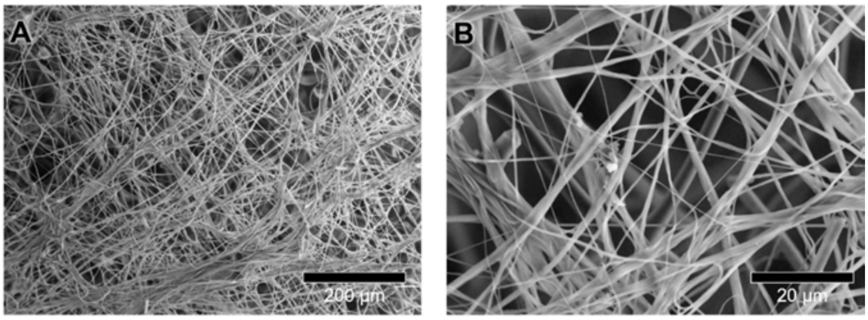

Figure 3-11. Dynamic wetting behaviors water and oil on the NF-S. (A) Time-lapsed images (i)-(iv) and (B)-(D) selected magnified images.

Figure 3-12 shows the application of the NF-S in an oil-water filter. The NF-S was attached to the tip of a PVC tube and the oil-water separation is shown in processes (i)-(iii) in **Figure 3-12A**. When an oil-water mixture was poured into the PVC tube, only oil penetrated the NF-S and was collected in a container below the PVC tube to obtain separated water and oil (**Figure 3-12B**). The separation efficiency for various types of oil was determined to be >99% in average (**Figure 3-12C**). The flux value for each type of oil is shown in **Figure 3-12D**. The flux (f) is related to the viscosity of the oil (μ) by $f = \mu d g L^{-1}$, where L, d, and g are the thickness and pore diameter of the NF-S, and gravitational constant, respectively (see **Table 3-3** for the viscosity of oils. [44, 45]). [2] Thus the separation flux decreased as the thickness increased (**Figure 3-12E**) and the pore size decreased (**Figure 3-12F**). The flux for gasoline permeating the membrane was 3000 $Lm^{-2}h^{-1}$. Herein, we compared the separation efficiency, flux, and the cost with various literatures in **Table 3-4**. [8, 33, 46-54] The-NF-S performed the cheapest cost and also high level separation efficiency and flux values. Furthermore, the NF-S folded five times performed the extraction of pure oils from an emulsified oil-water mixture with only assistance from gravitation (**Figure 3-12G-J**) via processes (i)-(iii) in **Figure 3-12A**.

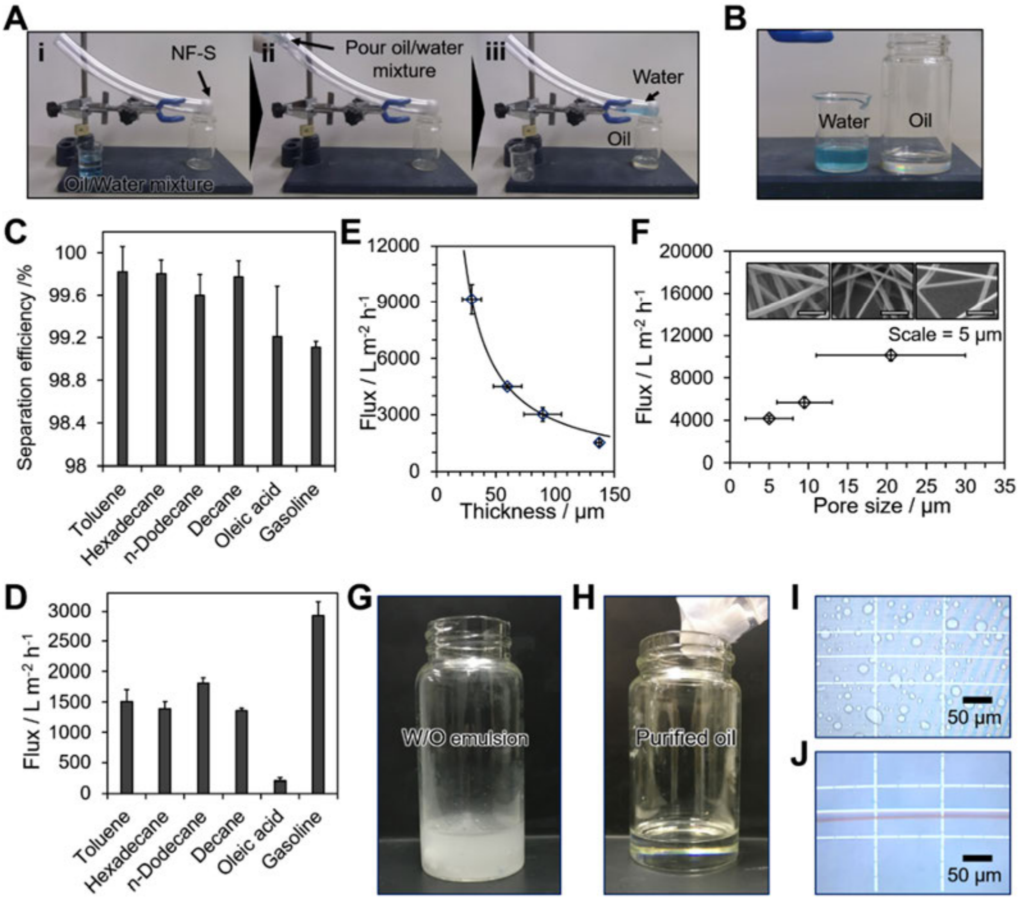

Figure 3-12. Application of 2D oil-water separation. (A) Oil-water separation filter. Photo-images show the separation of toluene from the toluene-water mixture in processes (i)-(iii). (B) A photo-image of toluene and water after separation. (C) Separation efficiency and (D) separation flux of oil-water mixtures with different types of oil. (E, F) Separation flux of the toluene-water mixture with different NF-S thicknesses (E) and pore diameters (F) adjusted by folding and extending the NF-S. (G, H) Photo-images and (I, J) microscopic images of the emulsified toluene-water mixture before (G, I) and after separation (H, J).

Table 3-3. Characteristics for each oil.

	Viscosity / mP s	Surface tension / mN m^{-1}	Density / g m^{-3}
Toluene	0.560	28.50	0.865
Hexadecane	3.061	27.47	0.773
n-Dodecane	1.352	25.35	0.745
n-Decane	0.841	23.83	0.730
Oleic acid	31	32	0.894
Gasoline [44, 45]	0.86	21.56	0.726

Table 3-4. Summary of 2D materials for oil/water separation properties

Materials	Preparation methods	Separation efficiency (%)	Flux (L m^{-2} h^{-1})	Cost (US$)	Reference
Polyaniline coated cotton fabric	vapor phase deposition	97.8	n.a.	4.5	[33]
polydopamine/n-dodecyl mercaptan mesh	Michael addition reaction	98.12	n.a.	7.6	[46]
cellulose hollow fiber	immersion precipitation technique	>97	7.7	<5	[47]
cellulose acetate-graft-polyacrylonitrile membranes	phase inversion method	>97	300	16.9	[48]
Vertically-aligned carbon nano-tube	thermal chemical vapor deposition	n.a.	85.6	-	[49]
poly(2-methacryloyloxylethyl phosphorylcholine)	grafting	>99.9	880	37.2	[50]

PMMA-b-P4VP membrane	copolymer synthesis and electro spinning	>98	n.a.	7.8	[51]
polybenzoxazine/TiO2	dip coating and thermal curing	>98	2900	23.6	[52]
carbon soot caoted steel mesh	combustion by candle	>99	10.2	<1	[53]
PTFE coated mesh	spray method	n.a.	n.a.	6.1	[8]
PVDF membrane	phase-inversion process	>99.9	3415	51.3	[54]
PVDF-HFP/Et-CA nanofibrous membrane	Just attach the NFs-S	99.8	3000	0.88	This work

Finally, the application of the NF-S in oil-collector is performed. The container which is covered with the NF-S allowed oil penetration in that only oil was collected in the container after pouring an oil-water mixture through the material as shown in processes (i)-(iii) in **Figure 3-13**.

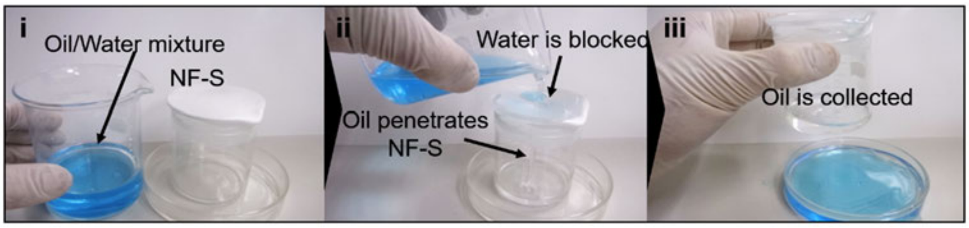

Figure 3-13. Application of an oil collector. Photo-images of toluene collection in a container from a toluene-water mixture in processes (i)-(iii).

Effect of PVDF-HFP: Et-CA ratio on NF-S performance. We furthermore discuss an influence of PVDF-HFP per Et-CA ratio on the NF-S properties. As varying the Et-CA weight ratio from PVDF-HFP: Et-CA=1:0.1 / w: w to =0.8:0.3 /w: w, the elastic property, wettability, fiber diameter, surface chemistry of NF-Ss changed as shown in **Figure 3-14**. The Et-CA is rigid and fragile, has higher surface energy than PVDF-HFP as mentioned in Chapter 2. The viscosity of Et-CA in acetone is lower than that of same contents of PVDF-HFP, considered with molecular weight. Thus, the addition of Et-CA in PVDF-HFP makes NF-Ss the lower strain and the more robust (**Figure 3-14A**), and the decrease of fiber diameter (**Figure 3-14C, D**). The decrease of surface energy and the fiber diameter with Et-CA addition makes NF-Ss an unlinered wettability change (**Figure 3-14B**) owing to the variation of surface energy and trapped air ratio. The surface chemistry of each NF-S consisted of PVDF-HFP and Et-CA was confirmed by Fluorine per Nitrogen atomic ratio from EDX (**Figure 3-14 E, F**, **Table 3-5**).

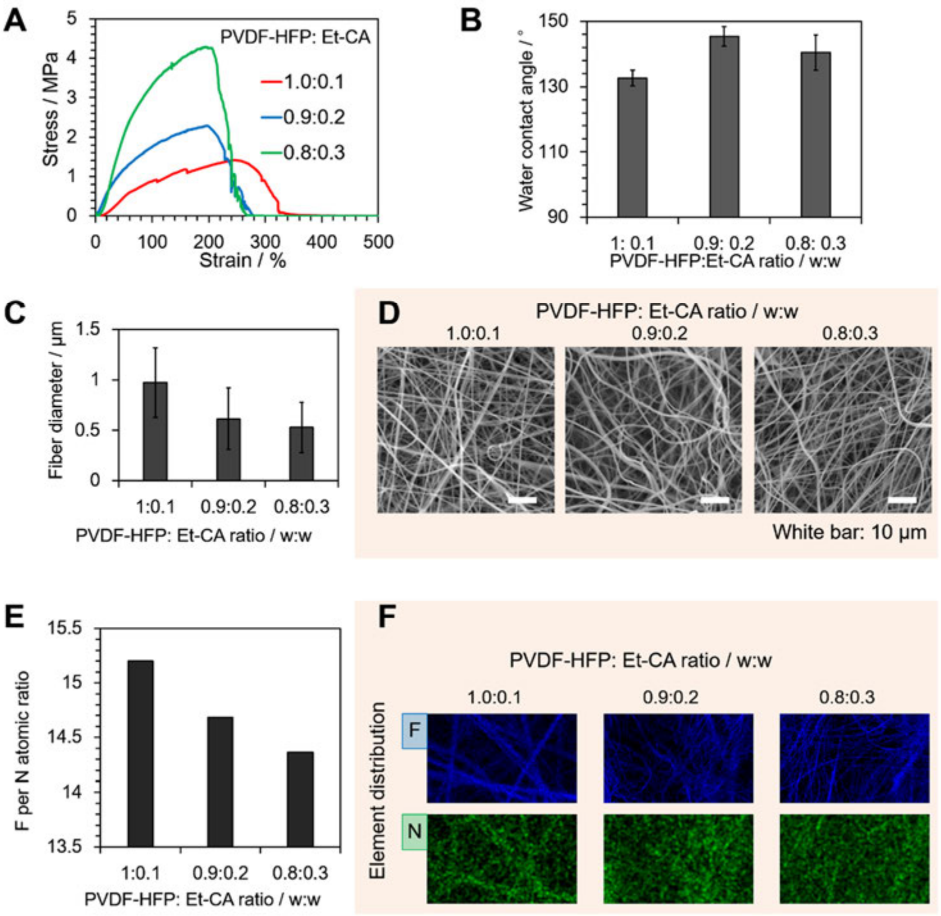

Figure 3-14. Effect of PVDF-HFP: Et-CA ratio on (A) extension ratio, (B) water contact angle, and (C, D) fiber diameter with the SEM images (D). (E) Atomic ratio of fluorine per nitrogen for each ratio of PVDF-HFP with Et-CA. (F) Elemental distribution of fluorine and nitrogen in the fibers with respect to the ratio of PVDF-HFP to Et-CA.

Table 3-5. Normalized atom ratio of fluorine, carbon, oxygen, and nitrogen by changing the ratio of PVDF-HFP to Et-CA.

		PVDF-HFP:Et-CA ratio / w:w		
		1:0.1	0.9:0.2	0.8:0.3
Normalized atom weight	F	36.412 ± 4.865	40.989 ± 5.302	42.483 ± 5.454
	C	56.838 ± 4.841	51.510 ± 4.265	50.378 ± 4.145
	O	4.354 ± 0.564	4.709 ± 0.576	4.181 ± 0.512
	N	2.396 ± 0.333	2.791 ± 0.348	2.958 ± 0.360

Method for large scale fabrication of NF-Ss. We designed a large-scale electrospinning device for the large-scale fabrication of the NF-Ss using a combination of a slider and drum roll as shown in **Figure 3-15**, and manufacture a NF-S at a size of 600×500 mm. This increases the possibilities to use the technology for practice.

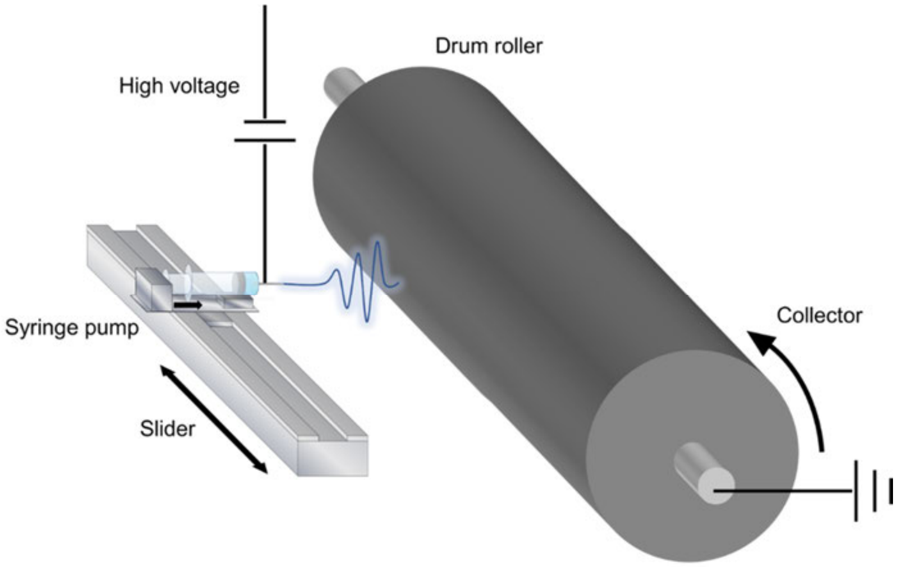

Figure 3-15. Electrospinning device for large-scale fabrication of NF-Ss. The slider moves in the direction of the arrow and the drum roller rotates to design uniform and large-scale NF-Ss

3.2.4 Conclusions

We introduced a self-standing, super-elastic and adhesive NF-S with selective wettability of hydrophobicity and oleophilicity at the same time inspired by the *Uloborus walckenaerius* spider web. The versatile application, low cost and simple process, scalability of NF-S can be helpful to develop the selective wetting materials for practical use. The dynamic wetting analysis revealed the part of oil remained on the NF-S functioned to block water penetration. We also give a new insight into the whole of materials field, that is, the possibility of designing advanced materials by combining different functional materials (e.g. In this work, the high absorption capacity by the melamine sponge and the selective wettability by NF-Ss are combined to be an oil-absorbent.)

References

[3-1] Wang, B., Liang, W., Guo, Z., & Liu, W. (2015). Biomimetic super-lyophobic and super-lyophilic materials applied for oil/water separation: a new strategy beyond nature. Chemical Society Reviews, 44(1), 336-361.

[3-2] Wang, L., Zhao, Y., Tian, Y., & Jiang, L. (2015). A general strategy for the separation of immiscible organic liquids by manipulating the surface tensions of nanofibrous membranes. Angewandte Chemie International Edition, 54(49), 14732-14737.

[3-3] Kota, A. K., Kwon, G., Choi, W., Mabry, J. M., & Tuteja, A. (2012). Hygro-responsive membranes for effective oil–water separation. Nature communications, 3, 1025.

[3-4] Tuteja, A., Choi, W., Mabry, J. M., McKinley, G. H., & Cohen, R. E. (2008). Robust omniphobic surfaces. Proceedings of the National Academy of Sciences, 105(47), 18200-18205.

[3-5] Dagastine, R. R., Manica, R., Carnie, S. L., Chan, D. Y. C., Stevens, G. W., & Grieser, F. (2006). Dynamic forces between two deformable oil droplets in water. Science, 313(5784), 210-213.

[3-6] Zhang, X., Li, Z., Liu, K., & Jiang, L. (2013). Bioinspired Multifunctional Foam with Self-Cleaning and Oil/Water Separation. Advanced Functional Materials, 23(22), 2881-2886.

[3-7] Yokoi, N., Manabe, K., Tenjimbayashi, M., & Shiratori, S. (2015). Optically transparent superhydrophobic surfaces with enhanced mechanical abrasion resistance enabled by mesh structure. ACS applied materials & interfaces, 7(8), 4809-4816.

[3-8] Feng, L., Zhang, Z., Mai, Z., Ma, Y., Liu, B., Jiang, L., & Zhu, D. (2004). A super-hydrophobic and super-oleophilic coating mesh film for the separation of oil and water. Angewandte Chemie International Edition, 43(15), 2012-2014.

[3-9] Si, Y., Fu, Q., Wang, X., Zhu, J., Yu, J., Sun, G., & Ding, B. (2015). Superelastic and superhydrophobic nanofiber-assembled cellular aerogels for effective separation of oil/water emulsions. ACS nano, 9(4), 3791-3799.

[3-10] Si, Y., Yu, J., Tang, X., Ge, J., & Ding, B. (2014). Ultralight nanofibre-assembled cellular aerogels with superelasticity and multifunctionality. Nature communications, 5, 5802.

[3-11] Xue, Z., Wang, S., Lin, L., Chen, L., Liu, M., Feng, L., & Jiang, L. (2011). A novel superhydrophilic and underwater superoleophobic hydrogel-coated mesh for

oil/water separation. Advanced Materials, 23(37), 4270-4273.

[3-12] Zhang, L., Zhong, Y., Cha, D., & Wang, P. (2013). A self-cleaning underwater superoleophobic mesh for oil-water separation. Scientific reports, 3, 2326.

[3-13] Gao, X., Xu, L. P., Xue, Z., Feng, L., Peng, J., Wen, Y., ... & Zhang, X. (2014). Dual-Scaled Porous Nitrocellulose Membranes with Underwater Superoleophobicity for Highly Efficient Oil/Water Separation. Advanced Materials, 26(11), 1771-1775.

[3-14] Dong, Y., Li, J., Shi, L., Wang, X., Guo, Z., & Liu, W. (2014). Underwater superoleophobic graphene oxide coated meshes for the separation of oil and water. Chemical Communications, 50(42), 5586-5589.

[3-15] Tian, X., Jokinen, V., Li, J., Sainio, J., & Ras, R. H. (2016). Unusual Dual Superlyophobic Surfaces in Oil–Water Systems: The Design Principles. Advanced Materials, 28(48), 10652-10658.

[3-16] Tao, M., Xue, L., Liu, F., & Jiang, L. (2014). An intelligent superwetting PVDF membrane showing switchable transport performance for oil/water separation. Advanced Materials, 26(18), 2943-2948.

[3-17] Zhang, L., Zhang, Z., & Wang, P. (2012). Smart surfaces with switchable superoleophilicity and superoleophobicity in aqueous media: toward controllable oil/water separation. NPG Asia Materials, 4(2), e8.

[3-18] Sun, T., Wang, G., Feng, L., Liu, B., Ma, Y., Jiang, L., & Zhu, D. (2004). Reversible switching between superhydrophilicity and superhydrophobicity. Angewandte Chemie, 116(3), 361-364.

[3-19] Xia, F., Feng, L., Wang, S., Sun, T., Song, W., Jiang, W., & Jiang, L. (2006). Dual-Responsive Surfaces That Switch between Superhydrophilicity and Superhydrophobicity. Advanced Materials, 18(4), 432-436.

[3-20] Lim, H. S., Kwak, D., Lee, D. Y., Lee, S. G., & Cho, K. (2007). UV-driven reversible switching of a roselike vanadium oxide film between superhydrophobicity and superhydrophilicity. Journal of the American Chemical Society, 129(14), 4128-4129.

[3-21] Hou, X., Hu, Y., Grinthal, A., Khan, M., & Aizenberg, J. (2015). Liquid-based gating mechanism with tunable multiphase selectivity and antifouling behaviour. Nature, 519(7541), 70-73.

[3-22] Shannon, M. A., Bohn, P. W., Elimelech, M., Georgiadis, J. G., Marinas, B. J., & Mayes, A. M. (2008). Science and technology for water purification in the coming decades. Nature, 452(7185), 301-310.

[3-23] Park, C. H., Lee, S. Y., Hwang, D. S., Shin, D. W., Cho, D. H., Lee, K. H., ... & Doherty, C. M. (2016). Nanocrack-regulated self-humidifying membranes. Nature,

532(7600), 480-483.

[3-24] Tenjimbayashi, M., Sasaki, K., Matsubayashi, T., Abe, J., Manabe, K., Nishioka, S., & Shiratori, S. (2016). A biologically inspired attachable, self-standing nanofibrous membrane for versatile use in oil–water separation. Nanoscale, 8(21), 10922-10927.

[3-25] Reddy, C. M., Arey, J. S., Seewald, J. S., Sylva, S. P., Lemkau, K. L., Nelson, R. K., ... & Van Mooy, B. A. (2012). Composition and fate of gas and oil released to the water column during the Deepwater Horizon oil spill. Proceedings of the National Academy of Sciences, 109(50), 20229-20234.

[3-26] Liu, X., Meng, R., Xing, Q., Lou, M., Chao, H., & Bing, L. (2015). Assessing oil spill risk in the Chinese Bohai Sea: a case study for both ship and platform related oil spills. Ocean & Coastal Management, 108, 140-146.

[3-27] Jayaramulu, K., Datta, K. K. R., Rösler, C., Petr, M., Otyepka, M., Zboril, R., & Fischer, R. A. (2016). Biomimetic Superhydrophobic/Superoleophilic Highly Fluorinated Graphene Oxide and ZIF-8 Composites for Oil–Water Separation. Angewandte Chemie International Edition, 55(3), 1178-1182.

[3-28] Cristóvão, R. O., Botelho, C. M., Martins, R. J., Loureiro, J. M., & Boaventura, R. A. (2015). Fish canning industry wastewater treatment for water reuse–a case study. Journal of Cleaner Production, 87, 603-612.

[3-29] Kwon, G., Post, E., & Tuteja, A. (2015). Membranes with selective wettability for the separation of oil–water mixtures. MRS Communications, 5(03), 475-494.

[3-30] Chu, Z., Feng, Y., & Seeger, S. (2015). Oil/water separation with selective superantiwetting/superwetting surface materials. Angewandte Chemie International Edition, 54(8), 2328-2338.

[3-31] Yang, Y., Yi, H., & Wang, C. (2015). Oil absorbents based on melamine/lignin by a dip adsorbing method. ACS Sustainable Chemistry & Engineering, 3(12), 3012-3018.

[3-32] Yang, Y., Deng, Y., Tong, Z., & Wang, C. (2014). Renewable lignin-based xerogels with self-cleaning properties and superhydrophobicity. ACS Sustainable Chemistry & Engineering, 2(7), 1729-1733.

[3-33] Zhou, X., Zhang, Z., Xu, X., Guo, F., Zhu, X., Men, X., & Ge, B. (2013). Robust and durable superhydrophobic cotton fabrics for oil/water separation. ACS applied materials & interfaces, 5(15), 7208-7214.

[3-34] Brown, P. S., & Bhushan, B. (2015). Mechanically durable, superoleophobic coatings prepared by layer-by-layer technique for anti-smudge and oil-water separation. Scientific reports, 5, 8701.

[3-35] Fang, W., Liu, L., Li, T., Dang, Z., Qiao, C., Xu, J., & Wang, Y. (2016). Electrospun N-Substituted Polyurethane Membranes with Self-Healing Ability for Self-Cleaning and Oil/Water Separation. Chemistry–A European Journal, 22(3), 878-883.

[3-36] Wang, H., Zhou, H., Yang, W., Zhao, Y., Fang, J., & Lin, T. (2015). Selective, Spontaneous One-Way Oil-Transport Fabrics and Their Novel Use for Gauging Liquid Surface Tension. ACS applied materials & interfaces, 7(41), 22874-22880.

[3-37] Li, J., Shi, L., Chen, Y., Zhang, Y., Guo, Z., Su, B. L., & Liu, W. (2012). Stable superhydrophobic coatings from thiol-ligand nanocrystals and their application in oil/water separation. Journal of Materials Chemistry, 22(19), 9774-9781.

[3-38] Wang, G., He, Y., Wang, H., Zhang, L., Yu, Q., Peng, S., ... & Xue, Q. (2015). A cellulose sponge with robust superhydrophilicity and under-water superoleophobicity for highly effective oil/water separation. Green Chemistry, 17(5), 3093-3099.

[3-39] Kronenberger, K., & Vollrath, F. (2015). Spiders spinning electrically charged nano-fibres. Biology letters, 11(1), 20140813.

[3-40] Peters, H. M. (1984). The spinning apparatus of Uloboridae in relation to the structure and construction of capture threads (Arachnida, Araneida). Zoomorphology, 104(2), 96-104.

[3-41] DiStasio, R. A., von Lilienfeld, O. A., & Tkatchenko, A. (2012). Collective many-body van der Waals interactions in molecular systems. Proceedings of the National Academy of Sciences, 109(37), 14791-14795.

[3-42] Vazquez, G., Alvarez, E., & Navaza, J. M. (1995). Surface tension of alcohol+ water from 20 to 50 C. Journal of chemical and engineering data, 40(3), 611-614.

[3-43] Wong, T. S., Kang, S. H., Tang, S. K., Smythe, E. J., Hatton, B. D., Grinthal, A., & Aizenberg, J. (2011). Bioinspired self-repairing slippery surfaces with pressure-stable omniphobicity. Nature, 477(7365), 443-447.

[3-44] Zhu, L., Chen, J., Liu, Y., Geng, R., & Yu, J. (2012). Experimental analysis of the evaporation process for gasoline. Journal of Loss prevention in the process Industries, 25(6), 916-922.

[3-45] Wang, F., Wu, J., & Liu, Z. (2006). Surface tensions of mixtures of diesel oil or gasoline and dimethoxymethane, dimethyl carbonate, or ethanol. Energy & fuels, 20(6), 2471-2474.

[3-46] Cao, Y., Zhang, X., Tao, L., Li, K., Xue, Z., Feng, L., & Wei, Y. (2013). Mussel-inspired chemistry and michael addition reaction for efficient oil/water separation. ACS applied materials & interfaces, 5(10), 4438-4442.

[3-47] Li, H. J., Cao, Y. M., Qin, J. J., Jie, X. M., Wang, T. H., Liu, J. H., & Yuan, Q. (2006). Development and characterization of anti-fouling cellulose hollow fiber UF membranes for oil–water separation. Journal of Membrane science, 279(1), 328-335.

[3-48] Chen, W., Su, Y., Zheng, L., Wang, L., & Jiang, Z. (2009). The improved oil/water separation performance of cellulose acetate-graft-polyacrylonitrile membranes. Journal of Membrane Science, 337(1), 98-105.

[3-49] Lee, C., & Baik, S. (2010). Vertically-aligned carbon nano-tube membrane filters with superhydrophobicity and superoleophilicity. Carbon, 48(8), 2192-2197.

[3-50] He, K., Duan, H., Chen, G. Y., Liu, X., Yang, W., & Wang, D. (2015). Cleaning of oil fouling with water enabled by zwitterionic polyelectrolyte coatings: Overcoming the imperative challenge of oil–water separation membranes. ACS nano, 9(9), 9188-9198.

[3-51] Li, J. J., Zhou, Y. N., & Luo, Z. H. (2015). Smart fiber membrane for pH-induced oil/water separation. ACS applied materials & interfaces, 7(35), 19643-19650.

[3-52] Zhang, W., Lu, X., Xin, Z., & Zhou, C. (2015). A self-cleaning polybenzoxazine/TiO2 surface with superhydrophobicity and superoleophilicity for oil/water separation. Nanoscale, 7(46), 19476-19483.

[3-53] Li, J., Kang, R., Tang, X., She, H., Yang, Y., & Zha, F. (2016). Superhydrophobic meshes that can repel hot water and strong corrosive liquids used for efficient gravity-driven oil/water separation. Nanoscale, 8(14), 7638-7645.

[3-54] Zhang, W., Shi, Z., Zhang, F., Liu, X., Jin, J., & Jiang, L. (2013). Superhydrophobic and superoleophilic PVDF membranes for effective separation of water-in-oil emulsions with high flux. Advanced Materials, 25(14), 2071-2076.

Chapter 4 Slippery-wetting materials bioinspired by pitcher plant *Nepenthes rafflesiana Jack*

This chapter is based on [Tenjimbayashi, M., Togasawa, R., Manabe, K., Matsubayashi, T., Moriya, T., Komine, M., & Shiratori, S. (2016). Liquid-Infused Smooth Coating with Transparency, Super-Durability, and Extraordinary Hydrophobicity. Advanced Functional Materials, 26(37), 6693-6702.]

4.1 Slippery wetting properties

The carnivorous pitcher plants such as *Nepenthes rafflesiana Jack* wet their leaves with lubricating oil to make insects slide down into their digestive juices. Inspired by the 'slippery' mechanism, Wong et al. reported slippery liquid infused porous surface(s) (SLIPS) by infusing a porous substrate with lubricating oil as in **Figure 4-1**. [1] Introduction of the slippery liquid interface rather than air-solid interface such like lotus surface enabled perfect slipperiness toward various kinds of liquid which was immiscible with lubricating oil. Indeed, the state-of-the-art surfaces have potential development of antiwetting materials with multi-functionality including transmittance, self-healing, damage tolerance, and pressure-stability.

Slippery wetting surface are designed by forming the porous oleophilic base layer (BL) and the following lubricant infusion to form a liquid layer (LL). SLIPS fabrication is based on three criteria: (i) LL must wick into, wet and stably adhere within the BL, (ii) the BL must be preferentially wetted by the LL rather than by the target liquid to be repelled, and (iii) the LL and the target liquid must be immiscible. [1] The first requirement is satisfied by micro-nanotextured rough BL to immobilize LL using capillary interaction.

To satisfy the second criterion-the BL must perform selective-wettability in that wet by the liquid as LL whereas dewet by the liquid to be repelled. From the viewpoint of thermodynamics, SLIPS must fulfill the criteria shown in **Figure 4-2**: Configuration *1* [lubricating liquid (liquid A) layer is formed on the roughened solid and target liquid (liquid B) does not replace the liquid layer] must be more stable than configuration A (roughened solid is wet by liquid B), and also configuration *2* (roughened solid is wet by liquid A) must be more stable than configuration *A* at the same time. The stability can be quantified by calculating total interfacial energies; $E_1 < E_A$, and $E_2 < E_A$ where the energy of configuration *1*,*2*, and *A* are E_1, E_2, and E_A, respectively. They yield $\Delta E_1 = E_A - E_1 = R(\gamma_B cos\theta_B - \gamma_A cos\theta_A) - \gamma_{AB} > 0$, and $\Delta E_2 = E_A - E_2 = R(\gamma_B cos\theta_B - \gamma_A cos\theta_A) + \gamma_A - \gamma_B > 0$ where γ_A, γ_B, and γ_{AB} are the surface tension of liquid A, liquid B, and the interfacial tension between the liquids, θ_A and θ_B are equilibrium contact angles of the liquids on a smooth BL, R is roughness factor.

SLIPS technology opened the new insight into the whole materials science by introducing a liquid coating rather than solid coating materials. Previously liquid infused surface materials have been widely studied. Aizenberg group developed SLIPS technologies into anti-icing metal materials, [2] antithrombosis and biofouling resistant medical device, [3] liquid gate filter, [4] highly effective heat transfer condensation material, [5] and smart optics/wettability tunable materials. [6] In our group, various liquid infused materials are reported including self-standing gel-like material, [7] anti-reflective anti-icing surface, [8] anti-biofouling endoscope lens, [9] solar cell coating, [10] and temperature triggered smart coating materials. [11]

Although such liquid immobilizing coating technology as represented in SLIPS showed the potential development, there still remains challenges in long-term use and controllable liquid layer formation since the rough BL limits liquid layer control and the exposure of rough BL along with LL evaporation deteriorates the properties. Thus, in this chapter, we developed the technologies into liquid layer patternable surface without introducing rough BL, to enlarge the potential application. [12] Our work also performed breakthrough toward the conventional liquid technology criteria: the roughness of BL being necessary for liquid surface, in that we succeeded liquid infused smooth surface by introducing π interaction instead of capillary. The surface with π-interacted liquid adsorption, smoothness, and hydrophobicity in short 'SPLASH' will be helpful to the development in whole materials science, we believe.

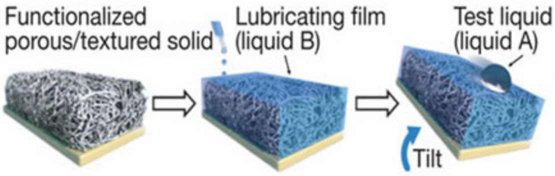

Figure 4-1. Schematic illustrations showing the fabrication of a SLIPS reproduced with permission. Copyright 2011, Nature Publishing Group [1].

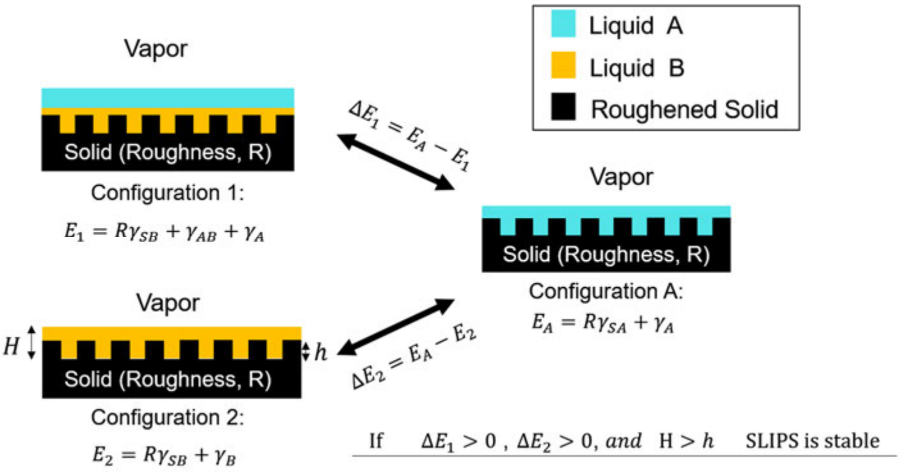

Figure 4-2. Schematic illustration which explains criteria for thermodynamically stable SLIPS formation. When configuration 1, and 2 are more stable than configuration A, SLIPS is stably let liquid A slide on the surface.

4.2 Surface with π-interaction liquid adsorption, smoothness and hydrophobicity (SPLASH)

4.2.1 Introduction

Hydrophobic coatings are of great importance in many scientific and technological fields, and various approaches have been used for their preparation and development of applications. [13-15] Lotus leaf inspired superhydrophobic surface is one of the famous approaches. The concept of superhydrophobic surface is to reduce the contact area between a liquid layer and the surface by trapped microscopic air layer on the controlled rough structure. Thus, the created air/solid composite surface enables liquid droplets to easily roll off. Although the development of superhydrophobic surfaces has made it possible to incorporate excellent liquid repellency with transparency or durability, [16, 17] there are still challenges for practical use, such as limited hydrophobicity (depending on the wetting state, temperature, size or viscosity), [18, 19] limited self-healing, and pressure instability due to the rough surface structure. [20]

SLIPS, where a LL is formed at the interface by infusing lubricating liquid in a nano/microscale porous BL, overcome the challenges of conventional hydrophobic surfaces; Thanks to the unique fluidic character, SLIPS succeed to possess stable hydrophobicity, transparency, quick self-healing property, and pressure stability.

From these backgrounds, LL-formation on surfaces has attracted strong attention for the design of multi-functional materials with special wettability, such as SLIPS, [1] xerogels, [21] and self-lubricating organogels [22] that contain a hydro-immiscible LL with multi-functional properties. Indeed, recently surfaces with covalently attached liquid-like molecules that show slipperiness towards liquids are also being developed. [18, 23, 24]

Hydrophobic surfaces that make use of the fluidity of the liquid interface retains the immobilized LL by capillary forces of the sponge-like BL. [25] Thus, the remaining challenges for next generation LL-immobilized surfaces are patternable LL formation on solid surfaces and LL transport to realize the systematic use of the LL surface. However, our concern is that the change of the LL thickness during the process of LL transport or patterning can make the immobilized LL surface properties unstable along with the exposure of the rough structure of BL. [1, 3, 6, 26] Therefore, a drastically different approach is required for designing controllable LL formation or transport on solids with a completely smooth structure to realize stable LL properties regardless of its thickness.

Here, we introduce a new approach for constructing liquid-absorbed smooth surface using π-electron interactions at the solid-BL/LL interface. In our approach, a π-electron-abundant smooth surface interacts with organic materials *via* π-stacking, which works even under a liquid state, [27, 28] allowing a wide variety of LLs to be trapped on the solid BL without rough structure. In addition, the localization of π-electrons enabled controllable LL formation, and liquid transport on smooth BL is also realized by patterned liquid adsorption, which has been limited only to water, previously. [25, 29] Furthermore, the π-stacking interaction realized superwetting of decyltimethoxysilane (DTMS) on BL without roughness enhancing to realize stable LL formation. By applying this concept, our π-electron-abundant smooth BL, which retains a hydrophobic and extremely low viscosity organic liquid (in this case DTMS), was designated as a surface with π-electron interaction liquid adsorption, smoothness, and hydrophobicity: SPLASH, which allows the development of a hydrophobic surface with multifunctional properties such as high optical transparency, extraordinary hydrophobicity, and defect-free self-healing properties; these properties were stable regardless of a changing in LL thickness.

This novel concept demonstrates the potential for designing controllable and stable liquid surfaces with multifunctionality, which may serve as the next generation state-of-the-art surfaces by replacing the “solid functional surface” with the “liquid-adsorbing surface”. [1, 6, 11, 21, 30-32] These liquid-adsorbing surfaces can be applied not only to hydrophobic surfaces but also to functional liquid surfaces for the development of a wide range of thin-film technologies, we believe. [33]

4.2.2 Experimental

Cocktail preparation. Mixture A for phenyl group modification was prepared by mixing 0.4322 g of phenyltriethoxysilane (PTES, Shin-Etsu Chemical Co., Ltd., Tokyo, Japan), 1.3791 g of tetramethoxysilane (TMOS, Junsei Chemical Co., Ltd., Tokyo, Japan), 5.59 mL of ethanol, 0.7566 mL of deionized water, and 2.04 μL of HCl in order, and the resulting mixture was stirring for 24 h for the reaction. Mixture B for decyl group modification was prepared by mixing 0.4725 g of decyltrimethoxysilane (DTMS, Shin-Etsu Chemical Co., Ltd.), 1.8876 g of tetraetoxysilane (TEOS, Wako Chemical Co., Ltd., Osaka, Japan), 5.59 mL of ethanol, 0.7566 mL of deionized water, and 2.04 μL of HCl in order, and the resulting mixture was stirring for 24 h for the reaction. Mixture C for the rough BL was prepared by dispersing 4 wt.% $(CH_3)_3$-Si modified hydrophobic SiO_2 nanoparticles (Aerosil RX 200, diameter ~12 nm, Evonik Industries, Germany) in ethanol.

Preparation of the surfaces. All of the substrates were made hydrophilic using UV/O_3 treatment [NL-UV253, Shoko Scientific Co., Ltd., (formerly Japan Laser Electron), Kanagawa, Japan] before coating with the LLs. The SiO_2-Ph were attached to the substrate by spin coating mixture A at a speed of 1000 rpm for 5 s and then at 2000 rpm for 10 s. SiO_2–C_{10} were attached to the substrate by spin coating cocktail B at a speed of 1000 rpm for 5 s and then at 2000 rpm for 10 s. These coatings were dried for 24 h at room temperature. The SPLASH was prepared by casting 0.08 μL cm^{-2} DTMS on the ethanol (purity 99.5%)-rinsed SiO_2–Ph substrate. DTMS was spread by a blower (The components of the SPLASH showed low toxicity with the standard of both LC-50 and LD-50.). The rough BL was prepared by spraying mixture C with the conditions of 0.8 MPa spraying pressure, 5 s spraying time, and about 30 cm of spray distance between the sprayer and the substrate, and drying for 1 h at room temperature.

Liquid spreading behaviour. Liquid spreading behaviour and liquid layer formation were measured using a high-speed camera (HAS-D3, Ditect Co., Ltd., Tokyo, Japan) and analyzed with Image J software (U. S. National Institutes of Health, Bethesda, Maryland, USA).

Wettability. Static contact angles, sliding angles, and underwater contact angles were measured using a contact-angle meter (CA-DT, Kyowa, Tokyo, Japan) and our own instrument. Endoscope application was conducted using an oscillating endoscope (SM20052, Machida Endoscope Co., Ltd., Japan). Contact angle hysteresis was measured by increasing and decreasing the droplet volume while taking screenshots and extracting the advancing and receding contact angles. Self-cleaning procedure of the SPLASH was assessed by covering the SPLASH with sands (Akadama-tuchi, Marukei, Co., Ltd., Tochigi, Japan) and casting deionized water droplet. Liquid sliding speeds were measured using a high-speed camera and analysed with Image J software. Mist spraying tests were conducted using a commercial hand sprayer and digital microscope (VHX5000, Keyence Corporation, Japan).

Optical analysis. Optical measurements were performed using a spectrophotometer (UVmini-1240, Shimadzu, Japan) and a haze meter (NDH-5000, Nippon Denshoku Industries, Japan) with a white-light-emitting diode (5 V, 3 W) as the optical source. The photocurrent density–voltage curves of single-crystal standard solar cells (Akihabara, Japan) were measured under illumination with an AM 1.5 solar simulator (100 mW cm^{-2}) for a 2.8 cm^2 masked area. A 500W xenon lamp (UXL-500SX, Ushio Inc., Tokyo, Japan) was used as the light source. A thickness and a refractive index of BL was measured using Ellipsometry (MARY-102, Five Lab, Japan).

Surface analysis. The surface smoothness was measured by atomic force microscopy (Nanoscope IIIa, Digital Instruments, USA). The surface morphology of the rough BL was measured by field emission scanning electron microscopy (FE–SEM, S-4700, Hitachi, Japan) with 5 kV voltage. The existence of π electrons was confirmed using the FE-SEM with charging-up and X-ray photoelectron spectroscopy (XPS, JPS-9010TR; JEOL Ltd., Japan) of π electrons derived from the satellite peak.

Durability analysis. Mechanical durability was assessed by vigorously cutting or wiping the SPLASH by cutter or cotton fabrics, respectively. Long term stability of the SPLASH was measured by preparing 6 samples under deionized water (ionic resistance: 18.2 MΩ) covered by container for preventing water evaporation, and 6 samples in our laboratory (20 °C). 0.08 μL cm^{-2} of DTMS as LL was casted on SiO_2–Ph coated glass substrate.

4.2.3 Results and Discussion

π-interacted liquid control on smooth surface. We firstly discuss how the existence of π-electrons affects the liquid wettability of the smooth solid surface. On the smooth surface, liquid without interactions never soaks into the substrate because there are no pore or space on solids. Thus, the design of hydrophobic smooth surface with patterned adsorption can achieve the control of LL formation or transport. We prepared two kinds of hydrophobic smooth surface using silane technology. One is the π electron abundant smooth surface by attaching phenyl groups to glass substrates with SiO_2 cross-linker

(SiO_2–Ph), because π electrons are charged in compounds including aromatic or alkyne groups. In this case, π electrons are confined in phenyl group tethered non-conducting SiO_2 matrix to make substrates π electron-abundant. The existence of π electrons was confirmed by X-ray photoelectron spectroscopy (XPS), whose satellite peaks derived from the π electrons were observed in 287-292 keV (**Figure 4-3A**). The other is essentially non-polar smooth surface prepared by decyl-group-modified surfaces (SiO_2–C_{10}) and the XPS spectrum is shown in **Figure 4-3B**. These two surfaces are almost completely flat, with root mean square roughness R_{rms} of <1 nm (**Figure 4-4**). The existence π-electrons influenced on various liquid wetting behavior as shown in **Figure 4-5A**. The liquid adsorption properties of the surfaces were quantified by measuring the sliding angles (SAs) of various test liquids (10 μL), as shown in **Figure 4-5B**. On smooth surface, liquids are never soaked into the surface, generally. Thus, all test liquids slide on SiO_2–C_{10}, whereas the liquids are completely pinned to form LL on SiO_2-Ph. In addition, static contact angles (SCAs) of test liquids are shown in **Figure 4-5C** (with visual images: **Figure 4-5A**). Oily liquids become superoleophilic on SiO_2–Ph coatings regardless the values of liquid surface energy, whereas the SCAs are proportional to liquid surface energy on SiO_2–C_{10}. These wettability analyses indicate that the liquid is adsorbed on the smooth surface owing to π interactions. The results showed that oily liquids with –OH, –COOH, –CHO, –CH, –OMe, –OEt, and –Ph groups except water, adsorb on SiO_2–Ph by CH-π, XH-π (X=O, COO, CO), or π-π interactions. Thus, we prepared various hydrophobic liquids with the functional groups mentioned above and checked whether they form a LL on SiO_2–Ph and whether the liquid-adsorbed surface can repel water droplets (see **Table 4-1**).

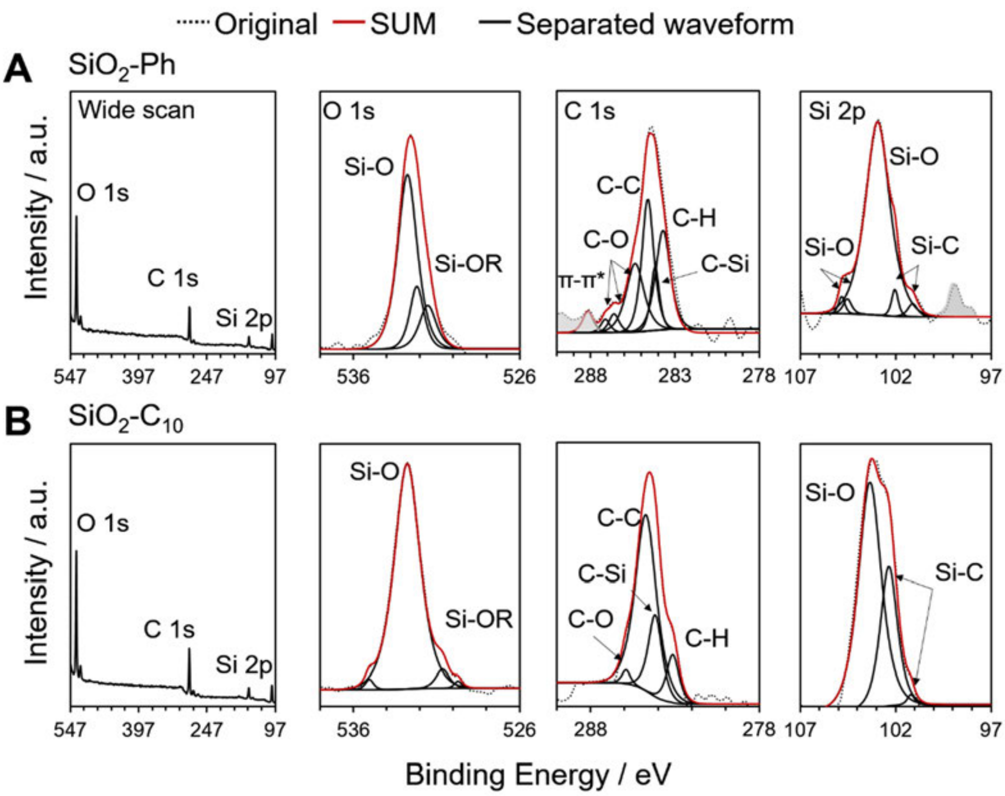

Figure 4-3. Wide-range x-ray photoelectron spectroscopy (XPS) analysis of the SiO_2-Ph and SiO_2-C_{10} showing the O_{1s}, C_{1s}, and Si_{2p} spectra employing an MgKα laser.

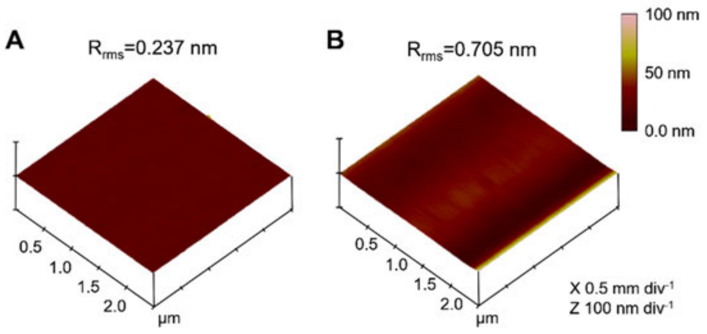

Figure 4-4. AFM images of (A) SiO_2-Ph and (B) SiO_2-C_{10} coated glass substrate.

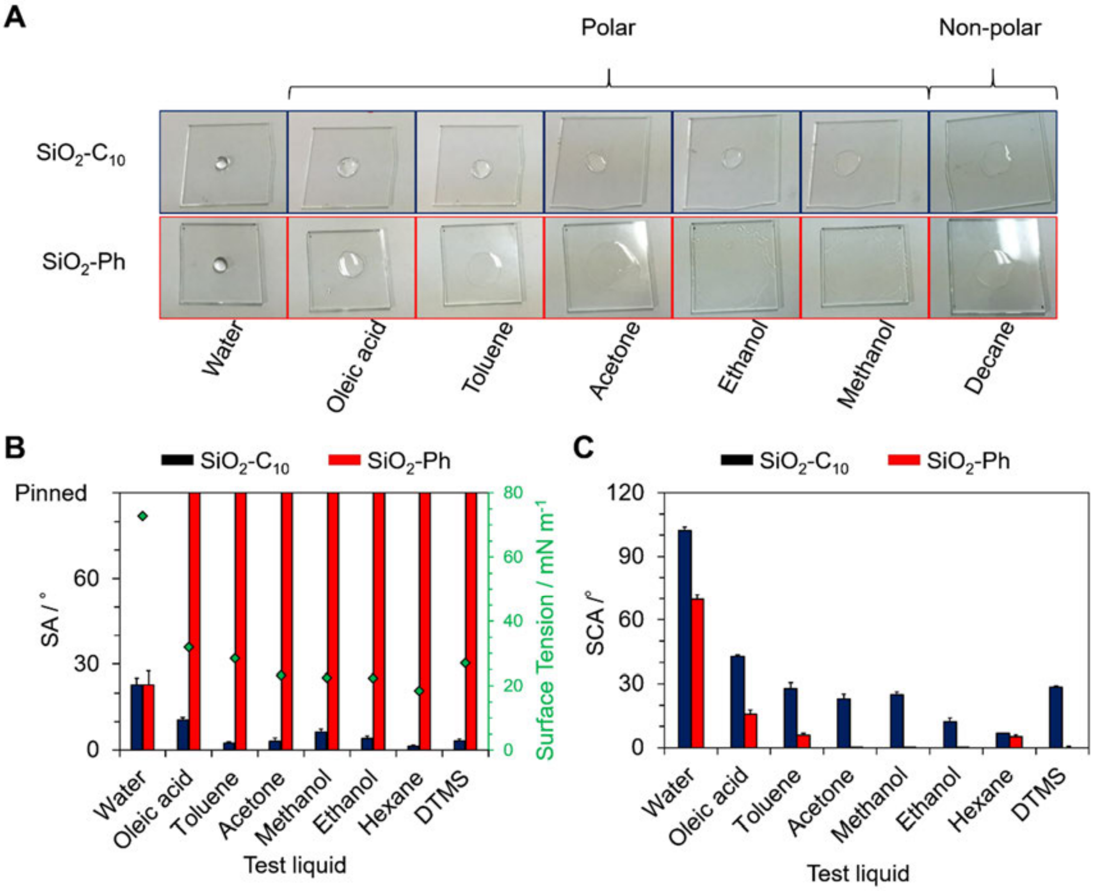

Figure 4-5. (A) Photographic images of various liquids dropped on the surface of SiO_2–Ph or SiO_2–C_{10}. These liquids are castedusing micropipette (10 μL). (B) Check of LL wetting on SiO_2–Ph compared with SiO_2–C_{10} (without π electrons). Sliding angle (SA) of various liquids measured on each surface. These liquids are casted on the surface using micropipette (10 μL). When the test liquid is adsorbed, the liquid does not slide. (C) Static contact angle (SCA) of various liquids measured on each surface.

Table 4-1. Summary of the types of liquid that can be adsorbed on the smooth surface and act as a liquid-repelling surface.

Liquid	Surface tension / mN m^{-1}	Viscosity / cSt	Structure	Whether liquid has interaction group	Whether a surface can repel water or not	Water sliding angle /°
KF-56A	24.4	15	$CH_3Si(CH_3)_2O[Si(CH_3)_2O]_m[Si(Ph)_2O]_nSi(CH_3)_3$	Y	Y	7.2±4.2
KF-96-30cs	20.7	30	$CH_3Si(CH_3)_2O[Si(CH_3)_2O]_nSi(CH_3)_3$	Y	Y	22.3±3.8
KF-96-100cs	20.9	100		Y	Y	24±9.7
KF-96-300cs	21.1	300		Y	Y	21.7±4.3
KF-96-500cs	21.1	500		Y	Y	26.3±3.3
KF-99	20	20	$CH_3Si(CH_3)_2O[SiHCH_3O]_nSi(CH_3)_3$	Y	Y	18.2±4.8
KF-50-100cs	21.8	100	$CH_3Si(CH_3)_2O[Si(CH_3)_2O]_m[Si(Ph)_2O]_nSi(CH_3)_3$	Y	Y	19±0.9
KF-50-300cs	22.2	300		Y	Y	5.8±1.8
DTMS	27	≈3.0	$CH_3(CH_2)_9Si(OMe)_3$	Y	Y	2.8±0.8
PFOTS	<20	—	$CF_3(CF_2)_5(CH_2)_2Si(OEt)_3$	Y	Y	20.2±1.4
PFDTS	<20	—	$CF_3(CF_2)_7(CH_2)_2Si(OEt)_3$	Y	Y	21.7±3.0
Krytox GPL 103 (PFPE)	17.1	30	$F(CFCF_3CF_2O)_nCF_2CF_3$	N	N	N/A
Hexadecane	27.6	≈3.1	$CH_3(CH_2)_{14}CH_3$	Y	Y	6.2±1.1
Oleic acid	32	≈30	$CH_3(CH_2)_7(CH)_2(CH_2)_7COOH$	Y	Y	2.8±1.8
Olive oil	≈35.8	46.7	Mixture of fatty acid R-COOH	Y	Y	5.8±1.9
Sesame oil	≈31.8	—		Y	Y	3.9±0.4
Rapeseed oil	≈35.0	50.6		Y	Y	4.2±1.0

These results show the possibility that the patterning of SiO_2–Ph and SiO_2–C_{10} can form localized LL and even with LL transportation capability. **Figure 4-6A** shows the designing approach of SiO_2–Ph and SiO_2–C_{10} patterned surface. The localization of π-electron-abundant layer can form LL, whereas non-polar layer cannot form them, achieving the mm-ordered control of LL formation (**Figure 4-6B**). Additionally, we demonstrated LL transport by designing a "sticky" [20, 29] π electrons, with the procedure as shown in **Figure 4-6C**, resulting in LL transport by diagonal sliding on the smooth solid (**Figure 4-6D**).

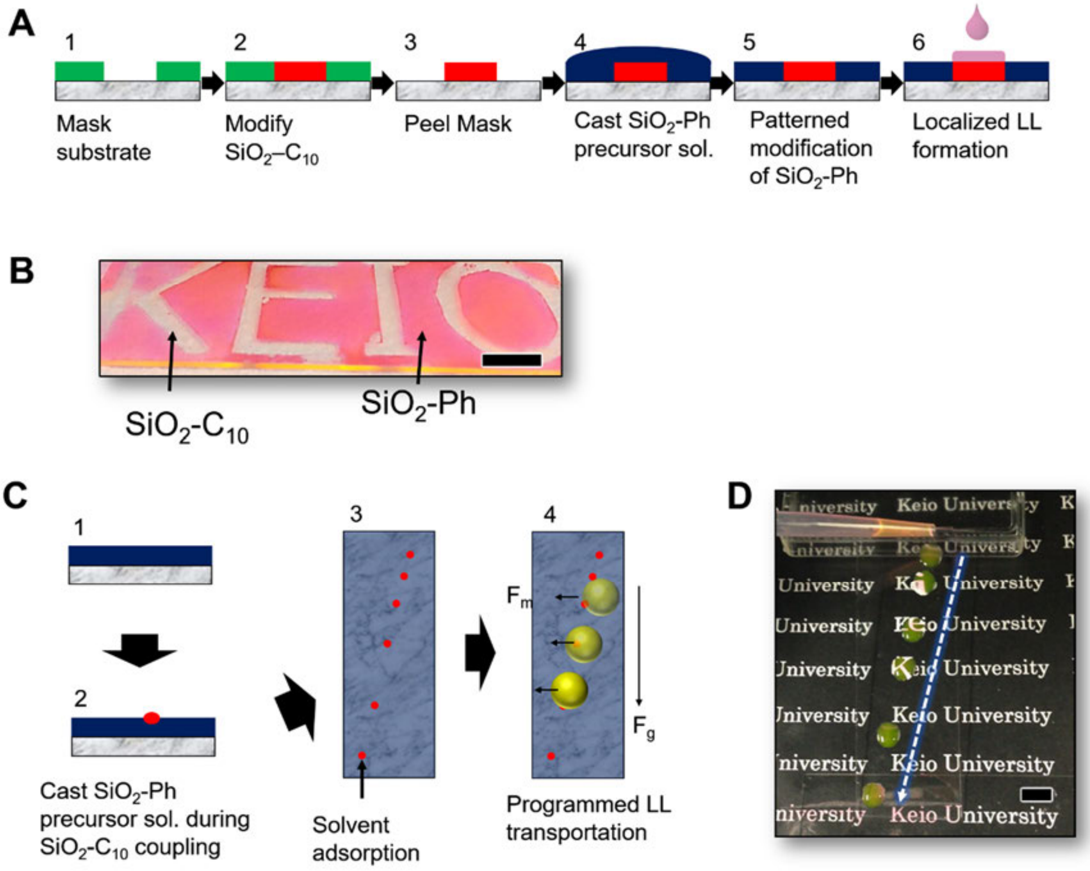

Figure 4-6. (A) Preparation procedure of the patternable LL formation. Patterned mask substrate (green) (1) is modified with SiO_2–C_{10} (red) to give (2). SiO_2–Ph precursor solution is then cast on the surface after the mask is removed (3) and the SiO_2–C_{10} area (blue) repels this liquid (4) to give the patterned surface (5). Dyed acetone as LL is cast on the patterned surface. (B) LL is formed in the shape of KEIO the scale bar is 10 mm. (C) Preparation procedure of the programmed LL transportation. Movement of LL on the patterned surface by the pinning effect. (1) SiO_2–C_{10} precursor solution (blue) is cast on the substrate and the (2) SiO_2–Ph precursor solution (red) is cast using a micropipette

during the SiO_2–C_{10} modification to program the way to transport (3). The LL (dyed acetone in this case) navigates along the blue dots by Marangoni F_m with gravity F_g forces, resulting movement of a LL droplet on the programmed surface. (D) The LL slides along the direction of the blue dotted arrow.

π-interacted dynamic wetting control on smooth surface. We discuss the wetting behaviour on SiO_2–Ph and SiO_2–C_{10} to investigate how the wetting are influenced by π-interaction and how the LL are formed. We prepared DTMS (viscosity ≈ 0.003 Pa s, surface tension = 27 mN m^{-1}) droplet to cast on SiO_2–Ph and SiO_2–C_{10} under a weber number $We=1.79$ with $We=\rho v^2 D\gamma^{-1}$ to observe the liquid-solid interactions because CH-π interactions work between –OMe of DTMS and SiO_2–Ph as shown in **Figure 4-7A**. Here, ρ is the liquid density, ν is the impact velocity, D is the droplet diameter, and γ is surface tension of DTMS. [34] **Figure 4-7B**, **C** show the time lapsed images of DTMS wetting behaviour on SiO_2–Ph and SiO_2–C_{10} captured by high speed camera with frame rate 1000 fps. Whereas DTMS droplet gradually shrink on SiO_2–C_{10} after the impact at -0.1 s, the droplet gradually spread to wet on SiO_2–Ph, finally being superoleophilicity (static contact angle, SCA <1°) at -30.0 s. Similar tendency was observed with changing DTMS into other test liquids. For quantifying wetting behaviour on two surfaces, the spreading width of the DTMS droplet was plotted as shown in **Figure 4-7D**, indicating that the width of LL on SiO_2–Ph gradually increasing. The wetting behaviour was approximated by the law of $W^2 (W^4-W_{impact}{}^4) \sim \gamma_L \cos\theta_{adv} (\tau-\tau_{impact})$ where W is spreading width, W_{impact} is initial wetting width (cross point of red and blue plot in Figure 6D), γ_L is surface tension of casting liquid, is θ_{adv} advancing contact angle, τ is time, and is τ_{impact} initial wetting time. [21] The fitting coefficient on SiO_2–C_{10} and SiO_2–Ph was 0.825 and 0.995, respectively (**Figure 4-7E**). In addition, we compared three smooth surfaces of SiO_2–C_{10},

SiO_2–Ph, and SiO_2-OH (Uncoated glass washed by EtOH) with the surface tension γ_s =24.4, 33.3, and 50.2 mN m^{-1}, respectively calculated from Van Oss method (**Table 4-2**), [35] whereas DTMS showed superoleophilicity (Oil contact angle [τ=30]≈0°) only on SiO_2–Ph as shown in **Figure 4-8A**. Although the surface energy of SiO_2–Ph surface is lower than uncoated glass from the water contact angle values, the contact angle of DTMS on SiO_2–Ph is much lower than that on SiO_2–OH. This result appears the adsorption of LL by CH-π interaction [36] between SiO_2–Ph and DTMS works as the combination of affinity force such as electrostatic force (like hydrogen bond) and dispersion force by aromatic groups' high polarizability. Thus, existence of π-electron on SiO_2–Ph leads to decrease interfacial tension between DTMS and SiO_2–Ph because of the Fowkes equation, [37] given by $\gamma_{SL} = \gamma_S + \gamma_L - 2\sqrt{\gamma_S^d \gamma_L^d} - 2\sqrt{\gamma_S^h \gamma_L^h}$ where γ_{SL} is interfacial tension of solid (S) and liquid (L), γ_S, γ_L is the surface tension of S and L, γ^d is the dispersion component, γ^h is the affinity component. Thus, the low γ_S and high γ^d, γ^h results low γ_{SL}. In addition, the Young's theory, [38] given by $\theta = cos^{-1}\left[\frac{\gamma_S - \gamma_{SL}}{\gamma_L}\right]$ where θ is contact angle of liquid, reveals that the low γ_{SL} can decrease contact angle and also induce moving of contact line to realize spread-wetting even though the γ_s is small. Thus, the existence of π-electron on surface enables low contact angle with selective liquid interaction (i.e. polar liquids became superoleophilic (SCA=0°) by π-electron effect shown in **Figure 4-6A, C**). Also, we observed the wetting behaviour of water droplet on DTMS cast BLs as shown in **Figure 4-8B**. In case of water droplet cast on SiO_2–OH with DTMS layer, the water droplet was pinned on the surface because the affinity of water with solid was stronger than that of DTMS with solid. In case of water droplet cast on SiO_2–C_{10} with DTMS, both water and DTMS was slid on the surface. In case of water droplet cast on SiO_2–Ph s with DTMS, water droplet was slid on the surface stably. Although perfluoropolyether (PFPE) does not adsorbed in pi electrons charged smooth base layer, PFPE has been retained on the base layer. Thus, we observed the condition of water droplet casting on smooth BL with PFPE as LL. Water droplet on PFPE surface is soaked to be pinned between LL and BL, as shown in **Figure 4-9**. This phenomenon supports our theory that SPLASH requires π interaction between LL and BL.

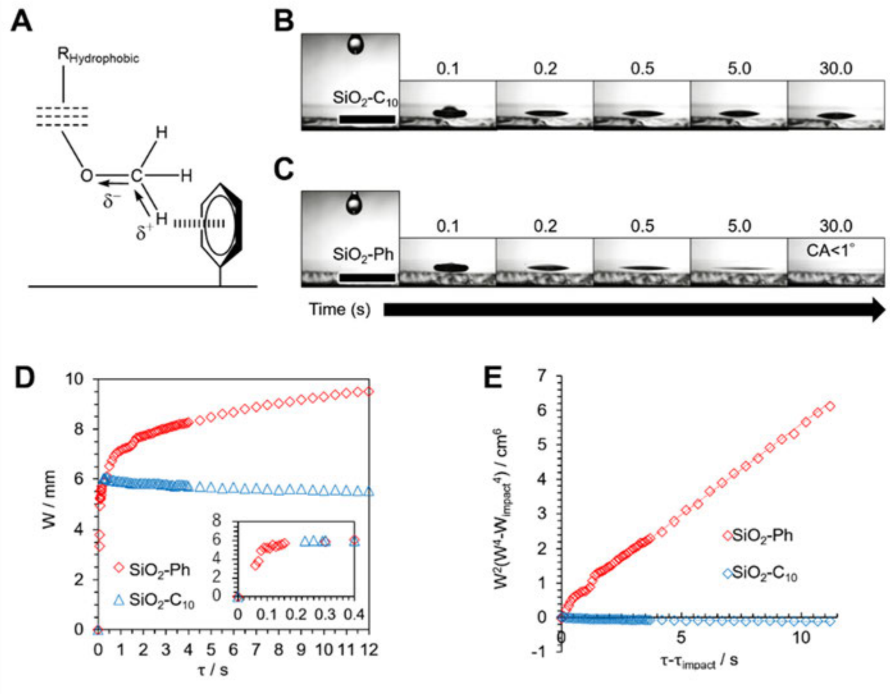

Figure 4-7. π-interacted liquid wetting analysis. (A) CH-π interactions between decyltrimethoxysilane (DTMS) as LL and SiO_2–Ph as BL. (B, C) Time-lapsed DTMS (10 μL) wetting behaviour on (B) SiO_2–C_{10} and (C) SiO_2–Ph. The scale bar is 5 mm. Because of the CH/pi interaction between LL and SiO_2-Ph BL, DTMS showed the extreme superoleophilicity (static contact angle SCA<1°) on SiO_2–Ph coated glass (25 mm × 25 mm) after 30 s. (D) Spreading width W of DTMS droplet wetting on SiO_2–Ph (Red) and SiO_2–C_{10} (Blue) per time t. (E) Approximation of droplet spreading with the law of $W^2(W^4-W_{impact}^4) \sim \gamma_L \cos\theta_{adv}(\tau-\tau_{impact})$.

Table 4-2. Surface tensions of each surface calculated by the Van Oss method.

Solid	$\gamma_{SV}(LW)$ / mN m^{-1}	$(\gamma_{SV}^{+})^{0.5}$ / (mN m^{-1})$^{0.5}$	$(\gamma_{SV}^{-})^{0.5}$ / (mN m^{-1})$^{0.5}$	$\gamma_{SV}(AB)$ / mN m^{-1}	γ_{SV} / mN m^{-1}
C_{10}- tethered area	24.12	0.38	0.35	0.27	24.39
Ph- tethered area	27.31	0.73	4.12	5.97	33.28

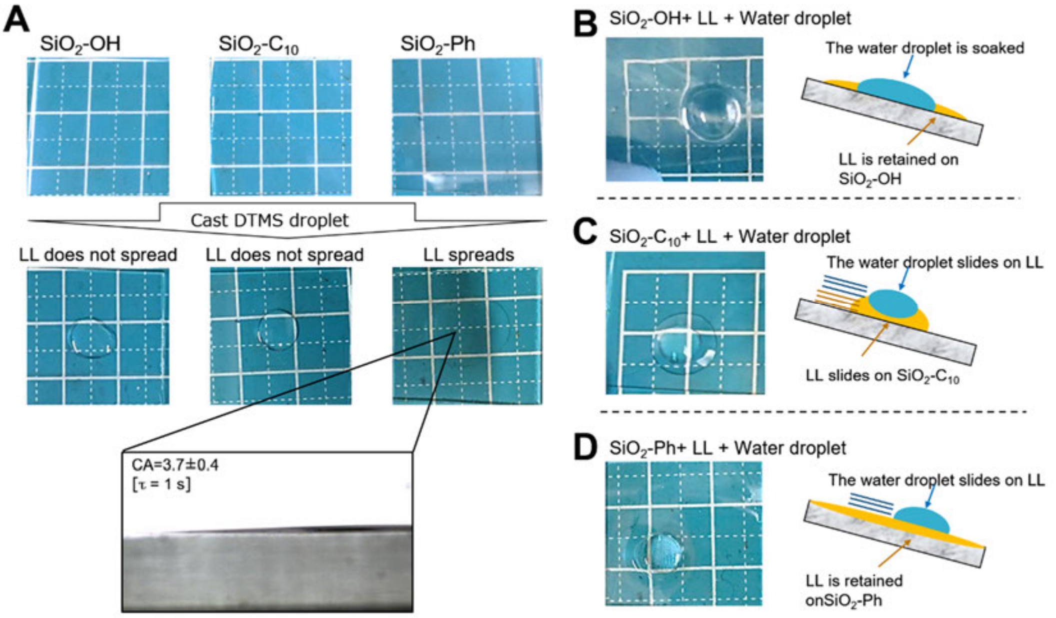

Figure 4-8. π-interacted liquid wetting analysis on different 3 functionalized smooth surfaces. (A) Images of LL wetting behaviour on the BLs of SiO_2-OH, SiO_2-C_{10}, and SiO_2-Ph. (B)-(D) The wetting behaviour of water droplet on DTMS cast BLs of (B), SiO_2-OH, (C), SiO_2-C_{10}, (D), and SiO_2-Ph.

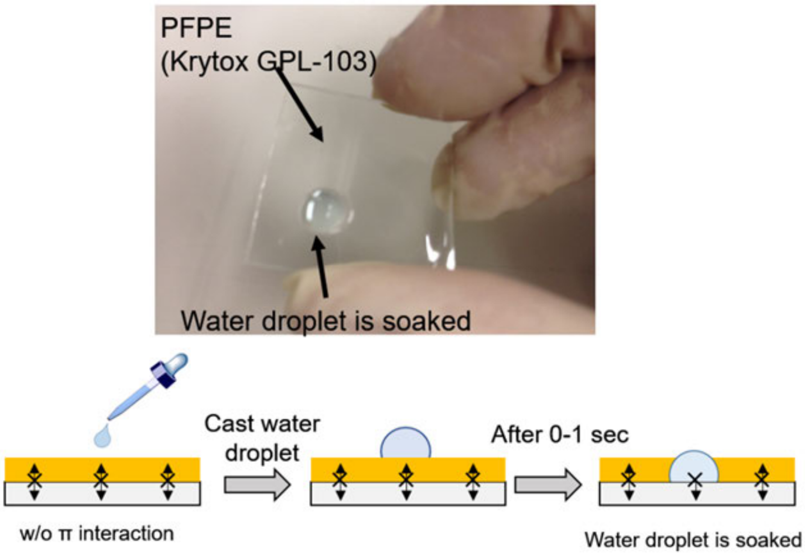

Figure 4-9. Photo image and schematic illustration showing the condition of water droplet casting on smooth BL with PFPE LL.

Surface design and hydrophobicity of the SPLASH. The SPLASH is realized by super-wetting of DTMS on SiO_2–Ph. **Figure 4-10A** shows the schematic illustration of the SPLASH structure. The UV/O_3-treated hydrophilic glass substrate was covalently attached to SiO_2–Ph via sol gel reaction to design smooth BL (R_{rms}=0.237 nm). Then, 0.08 μL cm^{-2} of DTMS was casted on the BL after EtOH washing. The limited thickness of LL was adsorbed by CH-π interaction and excess LL is adsorbed by the homogeneity between the liquid and the LL. We measured the change of the LL thickness and anti-wetting to water of a 50 mm × 50 mm SPLASH with adding shear stress using a spin coater. The LL thickness and the weight change are correlated with an equation; $t = \Delta m/(\rho S)$, where t is the LL thickness, Δm is the mass change, ρ is the density and S is the surface area. Even though the thickness of the excess LL drastically decreased with increasing spin rate until a spin rate of 3000, the thickness of the LL remained almost constant after the addition of shearing stress above 4000 rpm (**Figure 4-10B**). **Figure 4-**

11A, **B** show the wettability change of water on glass, the BL, and the LL-covered BL (the SPLASH). The SPLASH showed extraordinary water repulsion with a SA=0.5°. In addition, the dynamic water contact angle was extremely low with the contact angle hysteresis $\Delta\theta$=0.75° (**Figure 4-11C**, **D**). That's not only because of the LL property but also of the smoothness of BL with keeping the fluidity of LL. When we compared rough BL designed by self-assembly of hydrophobic nanoparticles and our smooth BL, LL on rough BL slides a water droplet with high hysteresis whereas LL on smooth BL can smoothly slide a water droplet (**Figure 4-12**). In addition, the SPLASH showed self-cleaning ability against sand on the surface (**Figure 4-11E**). It means that water droplets roll on the SPLASH. Differentiating water rolling from sliding is performed using the value of $(\mu_{\mathrm{o}}/\mu_{\mathrm{w}})\cdot(h_{\mathrm{cm}}/t)$, where μ_{w} is viscosity of water, h_{cm} is the height of the centre-of-mass of the water droplet above the solid surface, and t is thickness of the LL.[26] When $(\mu_{\mathrm{o}}/\mu_{\mathrm{w}})\cdot(h_{\mathrm{cm}}/t)$ >> 1 (or <1) water rolls (or slides) on the SPLASH. The calculated $(\mu_{\mathrm{o}}/\mu_{\mathrm{w}})\cdot(h_{\mathrm{cm}}/t)$ $\approx 2.1\times10^3$, indicating water rolling on the SPLASH. **Figure 4-11F** shows various targets sliding on the SPLASH, and the SPLASH repels not only water but also water in various states (boiled water and ice blocks) and other aqueous solutions (saline and blood). A strong benefit of the SPLASH is that the surface can strongly repel blood with fluorine-free materials. **Figure 4-11G** shows photographs of uncoated and SPLASH-coated glass after immersing in blood for a few seconds, showing that there is no blood contamination on the SPLASH-coated surface. We expect that this technology is suitable for medical applications, because the LL can be oleic acid via XH-π interaction (**Table 4-1**), which is classified as an edible oil, immiscible with blood, and the BL can endure ethanol disinfecting (ethanol cleaning is included in the preparation procedure of the SPLASH). Interestingly, the SPLASH repelled ice cream (a complex of solid, liquid, and chemical components), in which the melted part of the ice cream rapidly slid on the SPLASH, as shown in **Figure 4-11H**. We also expect this technology to be suitable for food packaging applications, because the LL can be silicone oil KF-54 via π-π interaction, which is contained in the positive list and immiscible with various fluidic foods containing oil as shown in **Figure 4-11I**.

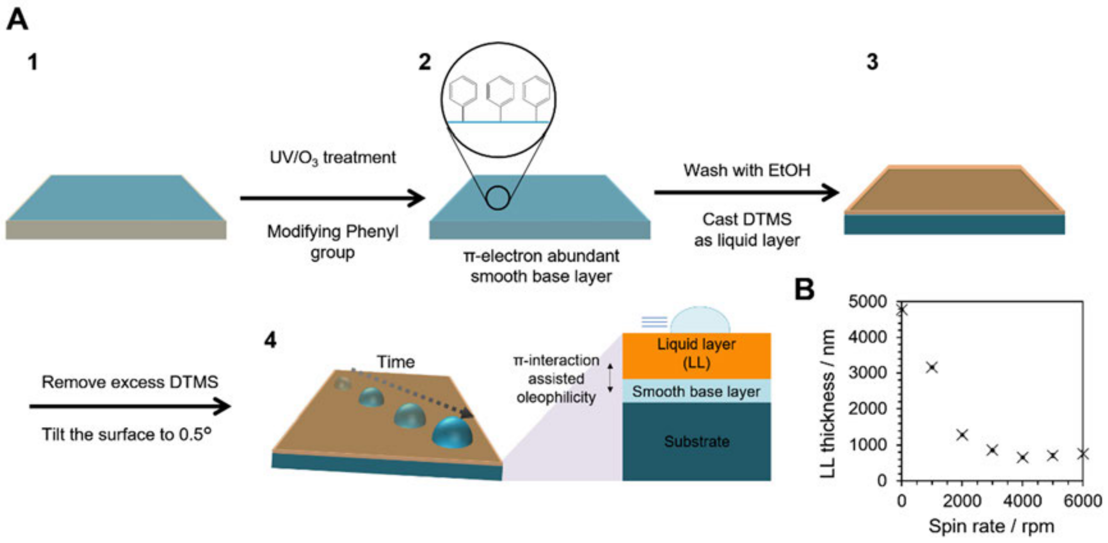

Figure 4-10. (A) Schematic illustration of procedure for designing SPLASH, and (B) Check of LL (DTMS) thickness formed on smooth base layer with shearing stress by a spin coater.

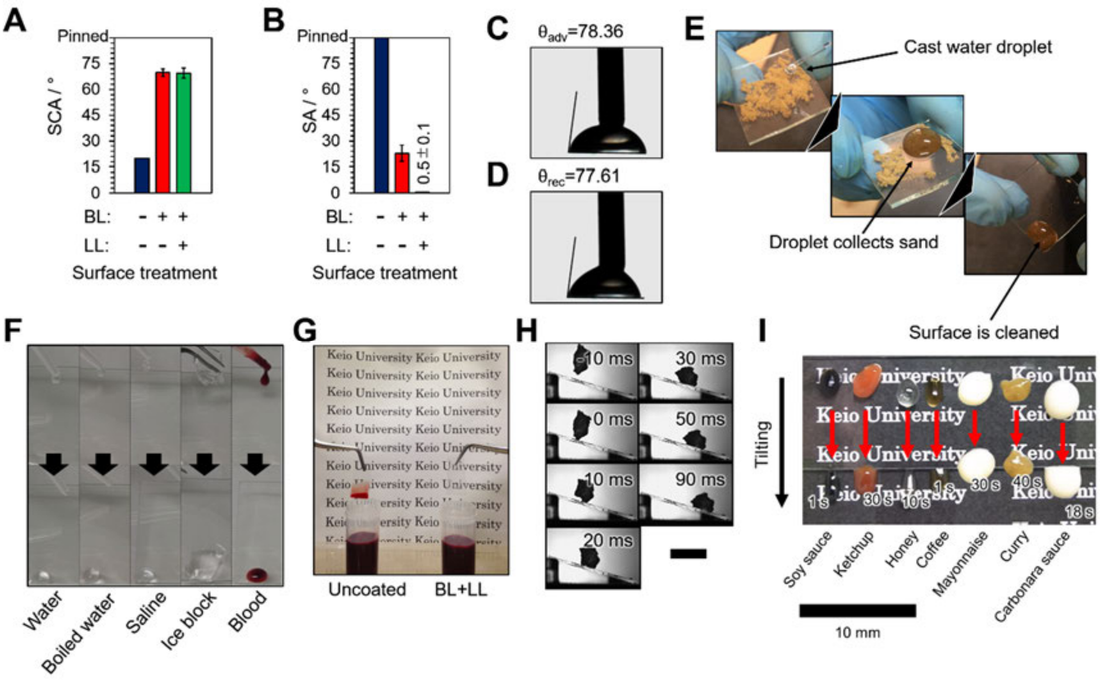

Figure 4-11. Hydrophobicity of the SPLASH. (A) Static contact angle (SCA) and (B) sliding angle of water droplet on each layered coating. Their values change after attaching SiO_2-Ph as the BL and DTMS as the LL. (C, D) Wetting image of (C) advancing contact angle (θ_{adv}) and (D) receding contact angle (θ_{rec}) measurement of water droplet. The calculated contact angle hysteresis ($\Delta\theta$) was 0.75°, that is extremely low values realized by fluidity of LL not resisted by the roughness of BL. (E) Photo-images of self-cleaning procedure of the SPLASH. Sands covering the SPLASH are cleaned by water droplet. (F) Various liquids with high temperature, chemical complexity, different states, and biomedia sliding on the SPLASH tilting 15°. (G) Images of glass (left) and coated glass (right) after dipping in blood. (H) High-speed camera images of ice cream, which is a complex with water/salt and solid/liquid, on BL+LL tilting 15°. (I) Various fluidic foods (soy sauce, ketchup, honey, coffee, mayonnaise, curry, carbonara sauce) slide on a SPLASH when a LL of silicone oil KF-54 is chosen. Soy sauce, ketchup, honey, coffee, mayonnaise, curry and carbonara sauce from supermarket.

An analysis of water droplet sliding behaviour and micro-droplet repellency on the SPLASH. The conceptual change from a superhydrophobic surface to a SLIPS results in loss of the quantity of the target liquid motion [6] to limit high speed removal or small water droplet removal. A recent approach has been reported to improve the quantity of the target liquid motion where a super-hydrophobic-like slippery surface [39] is prepared by constructing a needle-like base structure or decreasing the viscosity of the lubricant on SLIPS based on the equation $\mathrm{p} \sim \rho \mathrm{V}(1-\phi_{\mathrm{s}})/\mu_0$, where p is the liquid quantity of motion, ϕ_s is the area fraction of BL, ρ is the density of targeting liquid, V is the volume of targeting liquid and μ_0 is the lubricant viscosity. [40] However, decreasing the lubricant viscosity causes exposure of the BL in few minutes after LL formation, prohibits droplet movement and thus SLIPS have a large limitation for high speed removal or small water droplet removal (**Figure 4-12**). The uniqueness of the SPLASH with the low viscosity ($\mu_0 \approx$ 0.003 Pa s) and smoothness of BL ($\phi_{\mathrm{s}} \approx 0$) can achieve high targeting liquid quantity of motion even though the liquid volume is small. **Figure 4-13A** shows the liquid sliding length L per time τ ranging 0-1 s. The linear approximation for the calculation of water sliding velocity v with the law of $\mathrm{L} = \mathrm{v}\tau\ (\tau < 1)$ with the lowest fitting coefficients was 98.07. **Figure 4-13B** shows the water sliding speed with the various volume of water. Because of the high quantity of motion on the SPLASH, even the water droplet of V=1 μL slides on the surface. These properties enabled the surface to repel water mist applied by hand-spraying. **Figure 4-13C, D** show the continuously mist sprayed coatings. The SPLASH remained transparent after mist spraying. To investigate the reason why the SPLASH can efficiently repel water mist, we observed the behavior of water mist with a digital microscope. The observation revealed that the water mist removal process is composed of two stages: coalescence and the “sweep” effect. **Figure 4-13E**, **F** show a digital microscope image and a schematic illustration of coalescence, showing that microsized water droplets (yellow circles) move slowly and coalesce to form a large droplet (red circle) that slides. This phenomenon is realized because of the movement of small water droplets, which is unique to the SPLASH. The sweep effect is the behavior of a large droplet, as shown in the digital microscope image and the schematic illustration in **Figure 4-13G, H**. The large droplet moves and absorbs more microdroplets. The blue dotted area shows the passage of the large droplet. No droplets remain after the passage. Interestingly, the direction of the movement of the large droplet is not completely straight because the movement of the droplet is driven not only by gravity, but also by hydrophilic forces between droplets. Hence, the large droplet slides, searches for, and absorbs microdroplets, which is similar to how a sweeper finds dust to collect. Conventionally, to slide micro-size water droplet was extremely challenging. Recently J. Aizenberg and co-authors constructed the SLIPS with water collection and asymmetric bumps to realize the sliding of microdoplets. [5] Thus, here we note that the sweep and coalescence mechanism in the SPLASH can be used for various applications, such as heat transfer condensation, anti-fogging, and anti-icing. [41-43]

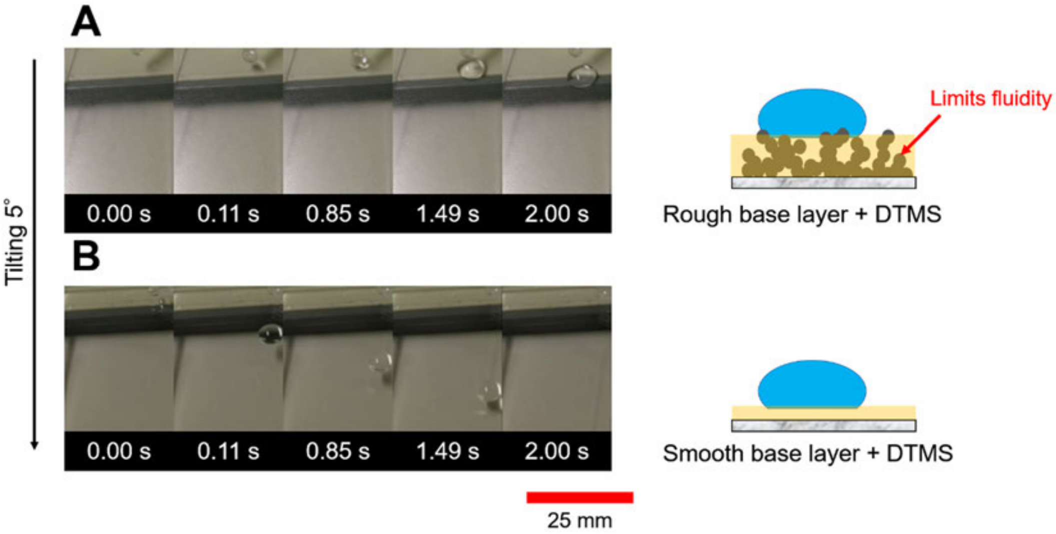

Figure 4-12. Time-lapsed images that compare water sliding behavior on rough BL+DTMS and smooth BL+DTMS.

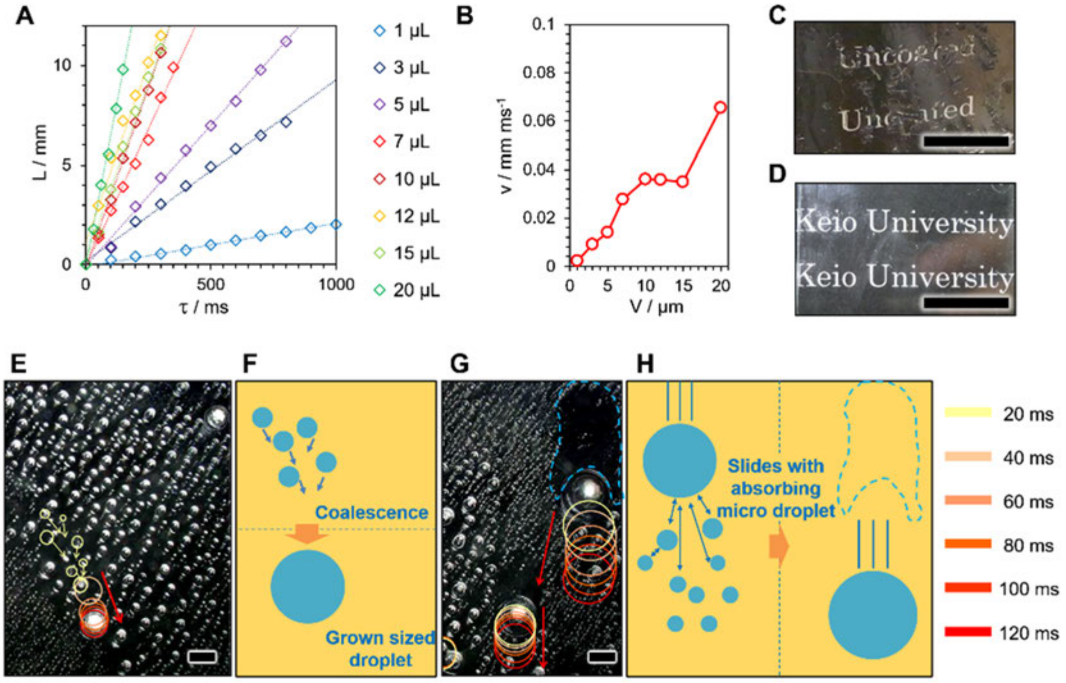

Figure 4-13. An analysis of water droplet sliding behaviour on the SPLASH. (A) The sliding length L of various volume water droplet per time τ on the SPLASH tilting 6° following the linear approximation with the law of $L = v\tau$ $(\tau < 1)$. (B) The sliding velocities v of various volume V of water droplet on the SPLASH tilting 6°. This graph revealed even 1 μL of water droplet slides on the SPLASH. (C, D) Photo images of (C) control and compared to (D) the SPLASH after misty water spraying test. Misty water was sprayed several times to them with same conditions. The scale bars are 20 mm. (E-H) Magnified images and schemes of water mist sprayed several times on the SPLASH tilting 75°. The water droplets circled in yellow coalescence into the droplet circled in red in an interval of 20 ms. The misty water droplets were removed by two steps of (E, F) and (G, H) process. (E, F) Microsized water droplets (yellow circles) coalesce into the large droplet and then the droplet slides (red circle). (G, H) Large water droplet moves absorbing microdroplets. The blue dotted area is the passage of the large droplet. No droplets remain in the blue dotted area.

Optical properties of the SPLASH. The optical properties of the SPLASH along with the rough BL+DTMS surface for comparison were analysed by photographs, transmittance in the visual wavelength range, and optical values of total transmittance (TT), parallel transmittance (PT), haze (HAZE) and diffusion (DIF). PT means the degree that light passes through a sample within a small range of angles (<15°). **Figure 4-14A-C** shows the measured transmittance of uncoated glass, the BL coating, and the BL with LL coating. The transmittance values are about 90% and not significantly different before and after applying the LL coatings, as shown in **Figure 4-14A, B**. However, the scattering of uncoated glass, the BL coating and the BL with LL coating slightly changes. To further investigate the optical components, we measured the TT, PT, HAZE and DIF values of the coatings (**Figure 4-14C**). The results indicate that there is no apparent loss of optical reflectance through the BL and LL coating and the scattering values of HAZE and DIF decreased after BL (and LL) coating because of the BL smoothness, resulting in higher PT than the uncoated surface. After LL coating on BL, the scattering values of HAZE and DIF are higher than those of the BL coating. The reason for the scattering value changing after LL coating can be associated with the change of phenyl groups arrangement by π–π interactions due to the LL adsorption. This is completely different from the concept of the liquid-infused surface, [1] where scattering decreases after infusing lubricant on the rough surface. Compared to uncoated substrate, the SPLASH showed lower scattering. Thus, a solar cell covered with the SPLASH showed higher performance than the one covered with uncoated substrate (**Figure 4-14D**). We further investigated the smoothness of the SPLASH showing the stable transparency against the change of LL thickness on smooth BL (**Figure 4-14E** for SEM image) compared to rough BL (**Figure 4-14F** for SEM image). **Figure 4-14G** shows the influence of BL roughness and LL on the visual transmittance of PT and the scattering loss of HAZE. The smooth BL after LL addition maintained its high transparency and low scattering with time because the interface between the layer and air is always flat in these states, as shown in the schematic illustrations in **Figure 4-14H**. On the other hand, the rough BL with LL shows relatively low transmittance and high scattering because of surface hierarchy. **Figure 4-14H** also shows schematic illustrations of the surface-state transitions on the rough BL. When LL is cast on the rough BL, the coating temporally becomes transparent because the surface/air interface becomes smooth. However, this surface becomes hazy with time because LL absorbs into the rough BL to decrease LL thickness, resulting the exposure of roughness. [6] These data indicate why BL must be smooth. Here the film thickness of smooth BL was 144.18±5.76 nm and the refractive index was 1.4422±0.0056

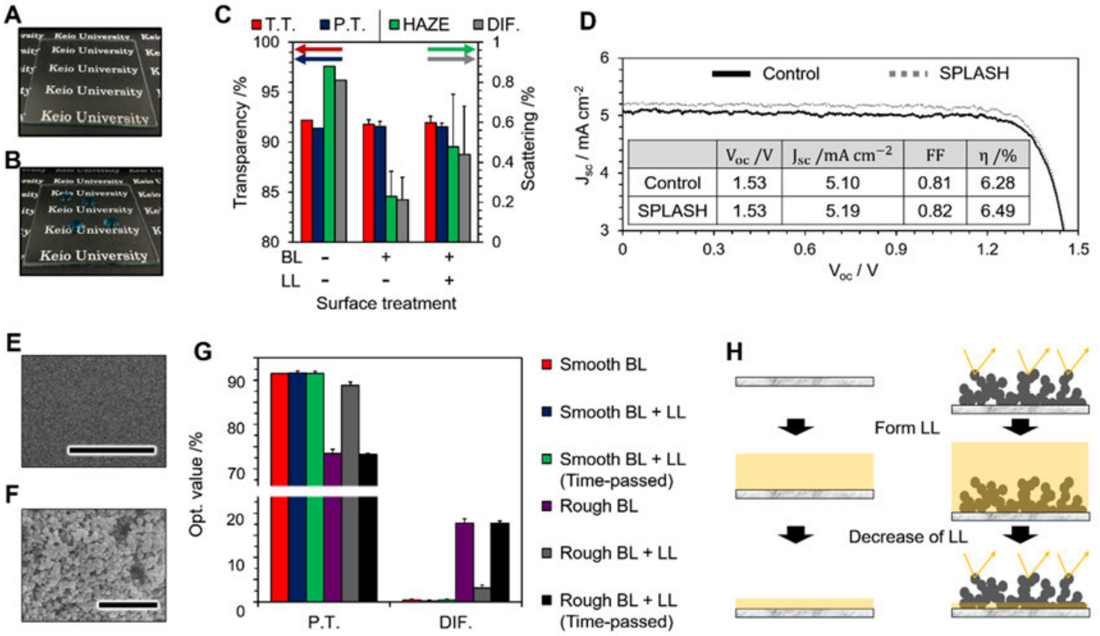

	V_{oc} /V	J_{sc} /mA cm^{-2}	FF	η /%
Control	1.53	5.10	0.81	6.28
SPLASH	1.53	5.19	0.82	6.49

Figure 4-14. Optical properties of the hydrophobic-liquid-adsorbed smooth surface. (A–D) Transparency of the SPLASH. (A) Photograph of the BL-coated glass substrate and (B) photograph of dyed water sliding on the BL with LL coating. (C) Total transmittance (TT), parallel transmittance (PT), haze (HAZE), and diffusion (DIF) of each surface. PT means the degree that light passes through a sample within a small range of angles (<15°). The HAZE value is given by haze (%) = DIF/TT × 100. (D) Solar cell application of the

SPLASH. Photocurrent density (J_{sc}) versus voltage (V_{oc}) for solar cells tilting 30°, one covered with a glass substrate, and one covered with SPLASH. Inserted table is a summary of the photovoltaic performance of solar cells under various conditions. (E-H) Assessment of the optical properties with the smooth BL [the same coating as the BL in (C)] and rough BL with DTMS as the LL. (E, F) The SEM images of smooth BL (E, the scale bar is 10 μm) and rough BL (F, the scale bar is 0.5 μm) by self-assembly of SiO_2 nanoparticles. (G), Optical values of PT and DIF for the smooth BL, smooth BL with LL, smooth BL with LL with time (30 min) to decrease LL thickness, rough BL, rough BL with LL, and rough BL with LL with time. (H), Schematic illustrations of the surface scattering change in the surface structure on the smooth BL and the rough BL with LL thickness. Smooth BL with LL shows stable transmittance with LL decrease whereas rough BL with LL increase light scattering with LL decrease.

Assessment of SPLASH stability and defect tolerance. The SPLASH maintained transparency and hydrophobicity despite the decrease of LL thickness controlled by spinning rate (see **Figure 4-10B**) as shown in **Figure 4-15A**. In addition, the SPLASH was stable continuously for at least 2 weeks under ambient conditions and even in water (**Figure 4-15B**). Even though the LL thickness decreased with time, the sliding angle was kept low whereas SLIPS gradually decreased the sliding angle along with the decrease of LL thickness. [44] This difference comes from whether BL was exposed or not. Thus, the SPLASH can perform stable hydrophobicity against the change of LL thickness. In addition, the SPLASH focus on repelling water based solution. Thus the adaptive pH range of targeting liquid is important for practical use. We worried the hydrolysis of Si–O bond in LL reacting with the water in specific pH values. Although the SPLASH repelled water with different pH values ranging 2-13 adjusted by HCl and NaOH, the water with pH>13.88 is soaked into a surface as shown in **Figure 4-15C**. In addition, pH values changed the water sliding angle, because pH values change the interfacial tension between LL and water γ_{LW} followed by ${\gamma^{h}}_{W}$ changing with pH values. [37] The

SPLASH coated on flexible PET film showed stable water sliding ability against bending, as shown in **Figure 4-15D**. The flexibility of the SPLASH comes from the smoothness of the BL and the stable LL. When the BL is rough, change of the LL height causes an exposure of rough solid to pin the target liquid. [6] On the other hand, a smooth BL does not get exposed by changing the LL height, as shown in **Figure 4-15E**. As shown in **Figure 4-15F**, we quantified the flexibility by measuring the sliding angle with the substrate bending rate of H/L, where H is the difference of the height from the centre of the substrate above the lowest area and L is the length of the substrate from end to end. Even bending 90% (when $H/L \approx 3.7$, the acute angle of the bent substrate is about 15.45° so the bending rate of $(180-15.45)°/180°\times100 \approx 90\%$), the sliding angle of the vertical side against the bending direction remained <2°. Furthermore, we investigated the mechanical robustness of the SPLASH. The SPLASH remained hydrophobicity even after cutting it 16 times (**Figure 4-15G**). Detailed analysis of cutting test revealed that the SPLASH shows self-healing ability of the LL as shown in schematic illustration in **Figure 4-15H**. When the LL is partially removed, the separated LL heals itself driven by the spreading wetting force as shown in **Figure 4-7C**. The SPLASH also showed abrasion resistance against cotton fabric. Cotton fabric is inherently superhydrophilic and shows strong liquid-absorbing properties. The SPLASH maintained hydrophobicity even after 80 times abrasion, as shown in **Figure 4-15I**. This is because the LL adsorbed on the BL by a stronger adsorbing force of F_{stacking} than the liquid absorbing force of F_{cap} by cotton fabrics (**Figure 4-15J**). This data also supports the liquid adsorption strength by π-stacking.

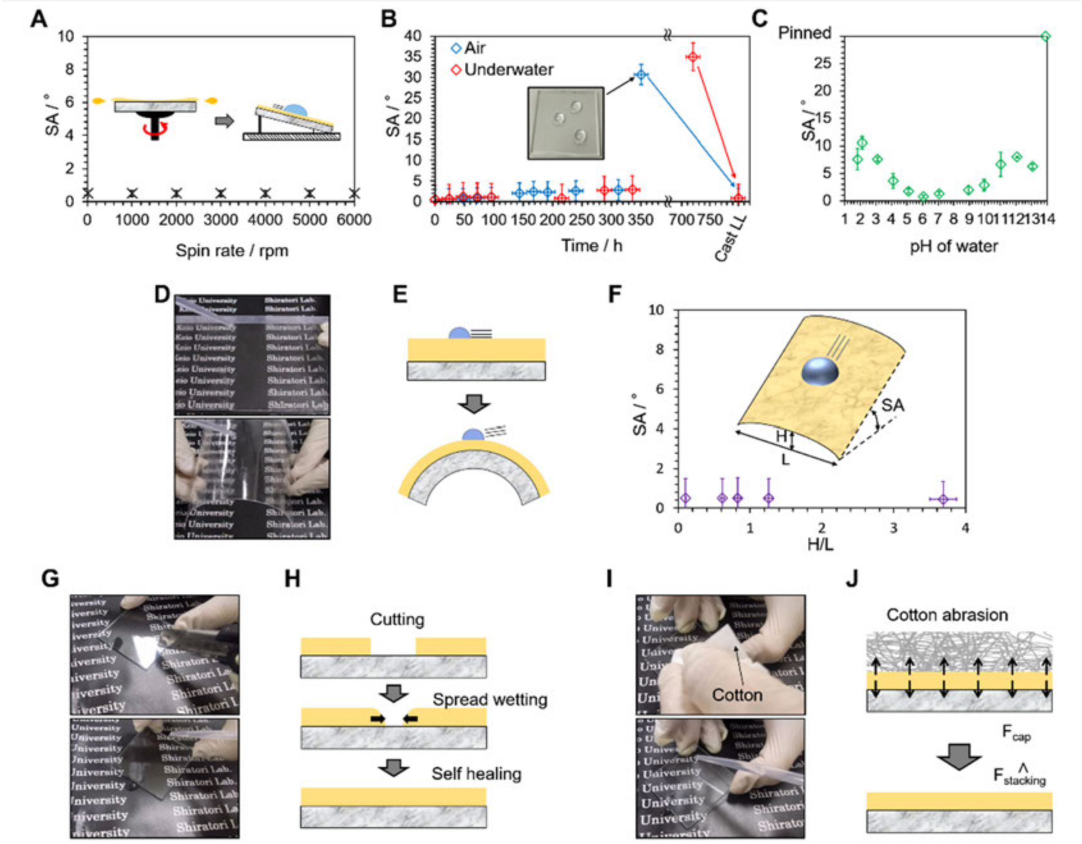

Figure 4-15. Assessment of SPLASH stability. (A) Sliding angle of deionized water after adding shearing stress from 0 to 6000 rpm by a spin coater for 30 s. (B) Long-term storage of glass slides covered with the SPLASH under air conditions (20°C, blue dots) and under water (red dots). Even though DTMS can possibly react on water or evaporate under air condition, the 0.08 μL cm^{-2} of DTMS casted SiO$_2$–Ph on glass slides (25 mm × 25 mm) kept the sliding angle low (<5°) for about 2 weeks under both conditions. Although the sliding angle decreased after long time, re-cast of LL have regenerated the sliding property. (C) Stability of the SPLASH against various pH conditions of water droplet ranging from 1.82 to 13.88. The sliding properties was stable in pH conditions ranging 1.82-13.06. In the case of pH 13.88, the water droplet was soaked into the SPLASH. (D-F) Flexibility of the SPLASH coated on PET film. (D) Photographs of the flexible SPLASH and (E) Schematic illustrations of water slides on the bent surface. Even though the thickness of the LL decrease, the hydrophobicity of the SPLASH does not change. That’s because of the smoothness of the BL. (F) Quantification of the flexible SPLASH hydrophobic property by changing the ratio of H/L. (G, H) Self-healing property of SPLASH. (G) Photographs of the cut SPLASH maintaining the hydrophobicity and (H) schematic illustrations showing why the SPLASH retains the hydrophobicity after cutting. (I, J) Mechanical durability against cotton abrasion. (I) Photographs of the SPLASH after

cotton abrasion showing that the hydrophobicity is retained and (J) schematic illustrations showing why the SPLASH retains the hydrophobicity after cotton abrasion.

4.2.4 Conclusions

In conclusion, we have reported controllable liquid-adsorption and transportation on smooth surfaces using π interactions as the next generation of liquid-infused surfaces. This technology can change the solid coating technology into liquid coating technology to add fluidic properties to coatings and can also realize controllable liquid-state materials at room temperature, which would be useful in a wide range of fields.

In this Chapter, we introduced the SPLASH as an example of a multifunctional coating using pi-interacted wetting control. The SPLASH is prepared by casting hydrophobic organic liquid on a phenyl-group-modified smooth base coating. The SPLASH showed not only extraordinary hydrophobicity but also high transparency, flexibility, self-healing and strong mechanical robustness that are independent of the change of LL thickness. In addition, the method to prepare the SPLASH is easy, cost-effective, fluorine free and available on various substrates. These properties are caused by the smoothness of the BL and the strongly adsorbed LL. The technology will be useful in industrial and medical fields, including the familiar applications such as anti-fouling windows, anti-adhesive containers or biomedical instruments.

References

[4-1] Wong, T. S., Kang, S. H., Tang, S. K., Smythe, E. J., Hatton, B. D., Grinthal, A., & Aizenberg, J. (2011). Bioinspired self-repairing slippery surfaces with pressure-stable omniphobicity. Nature, 477(7365), 443-447.

[4-2] Kim, P., Wong, T. S., Alvarenga, J., Kreder, M. J., Adorno-Martinez, W. E., & Aizenberg, J. (2012). Liquid-infused nanostructured surfaces with extreme anti-ice and anti-frost performance. ACS nano, 6(8), 6569-6577.

[4-3] Leslie, D. C., Waterhouse, A., Berthet, J. B., Valentin, T. M., Watters, A. L., Jain, A., ... & Super, E. H. (2014). A bioinspired omniphobic surface coating on medical devices prevents thrombosis and biofouling. Nature biotechnology, 32(11), 1134-1140.

[4-4] Hou, X., Hu, Y., Grinthal, A., Khan, M., & Aizenberg, J. (2015). Liquid-based gating mechanism with tunable multiphase selectivity and antifouling behaviour. Nature, 519(7541), 70-73.

[4-5] Park, K. C., Kim, P., Grinthal, A., He, N., Fox, D., Weaver, J. C., & Aizenberg, J. (2016). Condensation on slippery asymmetric bumps. Nature, 531(7592), 78-82.

[4-6] Yao, X., Hu, Y., Grinthal, A., Wong, T. S., Mahadevan, L., & Aizenberg, J. (2013). Adaptive fluid-infused porous films with tunable transparency and wettability. Nature materials, 12(6), 529-534.

[4-7] Okada, I., & Shiratori, S. (2014). High-transparency, self-standable Gel-SLIPS fabricated by a facile nanoscale phase separation. ACS applied materials & interfaces, 6(3), 1502-1508.

[4-8] Manabe, K., Nishizawa, S., Kyung, K. H., & Shiratori, S. (2014). Optical phenomena and antifrosting property on biomimetics slippery fluid-infused antireflective films via layer-by-layer comparison with superhydrophobic and antireflective films. ACS applied materials & interfaces, 6(16), 13985-13993.

[4-9] Nishioka, S., Tenjimbayashi, M., Manabe, K., Matsubayashi, T., Suwabe, K., Tsukada, K., & Shiratori, S. (2016). Facile design of plant-oil-infused fine surface asperity for transparent blood-repelling endoscope lens. RSC Advances, 6(53), 47579-47587.

[4-10] Abe, J., Tenjimbayashi, M., & Shiratori, S. (2016). Electrospun nanofiber SLIPS exhibiting high total transparency and scattering. RSC Advances, 6(44), 38018-38023.

[4-11] Manabe, K., Matsubayashi, T., Tenjimbayashi, M., Moriya, T., Tsuge, Y., Kyung, K. H., & Shiratori, S. (2016). Controllable Broadband Optical Transparency and

Wettability Switching of Temperature-Activated Solid/Liquid-Infused Nanofibrous Membranes. ACS nano, 10(10), 9387-9396.

[4-12] Tenjimbayashi, M., Togasawa, R., Manabe, K., Matsubayashi, T., Moriya, T., Komine, M., & Shiratori, S. (2016). Liquid-Infused Smooth Coating with Transparency, Super-Durability, and Extraordinary Hydrophobicity. Advanced Functional Materials, 26(37), 6693-6702.

[4-13] Kota, A. K., Kwon, G., Choi, W., Mabry, J. M., & Tuteja, A. (2012). Hygro-responsive membranes for effective oil–water separation. Nature communications, 3, 1025.

[4-14] Si, Y., Fu, Q., Wang, X., Zhu, J., Yu, J., Sun, G., & Ding, B. (2015). Superelastic and superhydrophobic nanofiber-assembled cellular aerogels for effective separation of oil/water emulsions. ACS nano, 9(4), 3791-3799.

[4-15] Feng, X. J., & Jiang, L. (2006). Design and creation of superwetting/antiwetting surfaces. Advanced Materials, 18(23), 3063-3078.

[4-16] Yokoi, N., Manabe, K., Tenjimbayashi, M., & Shiratori, S. (2015). Optically transparent superhydrophobic surfaces with enhanced mechanical abrasion resistance enabled by mesh structure. ACS applied materials & interfaces, 7(8), 4809-4816.

[4-17] Tenjimbayashi, M., & Shiratori, S. (2014). Highly durable superhydrophobic coatings with gradient density by movable spray method. Journal of Applied Physics, 116(11), 114310.

[4-18] Wang, L., & McCarthy, T. J. (2016). Covalently attached liquids: instant omniphobic surfaces with unprecedented repellency. Angewandte Chemie, 128(1), 252-256.

[4-19] Yang, S., Du, J., Cao, M., Yao, X., Ju, J., Jin, X., ... & Jiang, L. (2015). Direct Insight into the Three-Dimensional Internal Morphology of Solid–Liquid–Vapor Interfaces at Microscale. Angewandte Chemie International Edition, 54(16), 4792-4795.

[4-20] Vogel, N., Belisle, R. A., Hatton, B., Wong, T. S., & Aizenberg, J. (2013). Transparency and damage tolerance of patternable omniphobic lubricated surfaces based on inverse colloidal monolayers. Nature communications, 4, 2176.

[4-21] Cui, J., Daniel, D., Grinthal, A., Lin, K., & Aizenberg, J. (2015). Dynamic polymer systems with self-regulated secretion for the control of surface properties and material healing. Nature materials, 14(8), 790-795.

[4-22] Urata, C., Dunderdale, G. J., England, M. W., & Hozumi, A. (2015). Self-lubricating organogels (SLUGs) with exceptional syneresis-induced anti-sticking

properties against viscous emulsions and ices. Journal of Materials Chemistry A, 3(24), 12626-12630.

[4-23] Yu, L., Chen, G. Y., Xu, H., & Liu, X. (2016). Substrate-independent, transparent oil-repellent coatings with self-healing and persistent easy-sliding oil repellency. ACS nano, 10(1), 1076-1085.

[4-24] Rabnawaz, M., & Liu, G. (2015). Graft-Copolymer-Based Approach to Clear, Durable, and Anti-Smudge Polyurethane Coatings. Angewandte Chemie International Edition, 54(22), 6516-6520.

[4-25] Kamei, J., & Yabu, H. (2015). On-Demand Liquid Transportation Using Bioinspired Omniphobic Lubricated Surfaces Based on Self-Organized Honeycomb and Pincushion Films. Advanced Functional Materials, 25(27), 4195-4201.

[4-26] Smith, J. D., Dhiman, R., Anand, S., Reza-Garduno, E., Cohen, R. E., McKinley, G. H., & Varanasi, K. K. (2013). Droplet mobility on lubricant-impregnated surfaces. Soft Matter, 9(6), 1772-1780.

[4-27] Ariga, K., Vinu, A., Ji, Q., Ohmori, O., Hill, J. P., Acharya, S., ... & Shiratori, S. (2008). A Layered Mesoporous Carbon Sensor Based on Nanopore-Filling Cooperative Adsorption in the Liquid Phase. Angewandte Chemie International Edition, 47(38), 7254-7257.

[4-28] Kosaki, Y., Izawa, H., Ishihara, S., Kawakami, K., Sumita, M., Tateyama, Y., ... & Hill, J. P. (2013). Nanoporous carbon sensor with cage-in-fiber structure: Highly selective aniline adsorbent toward cancer risk management. ACS applied materials & interfaces, 5(8), 2930-2934.

[4-29] Manna, U., & Lynn, D. M. (2015). Fabrication of Liquid-Infused Surfaces Using Reactive Polymer Multilayers: Principles for Manipulating the Behaviors and Mobilities of Aqueous Fluids on Slippery Liquid Interfaces. Advanced Materials, 27(19), 3007-3012.

[4-30] Wang, C., Wu, H., Chen, Z., McDowell, M. T., Cui, Y., & Bao, Z. (2013). Self-healing chemistry enables the stable operation of silicon microparticle anodes for high-energy lithium-ion batteries. Nature chemistry, 5(12), 1042-1048.

[4-31] Khalil, K. S., Mahmoudi, S. R., Abu-Dheir, N., & Varanasi, K. K. (2014). Active surfaces: Ferrofluid-impregnated surfaces for active manipulation of droplets. Applied Physics Letters, 105(4), 041604.

[4-32] Li, S., Chen, N., Gaddes, E. R., Zhang, X., Dong, C., & Wang, Y. (2014). A Drosera-bioinspired hydrogel for catching and killing cancer cells. Scientific reports, 5, 14297-14297.

[4-33] Ariga, K., Yamauchi, Y., Rydzek, G., Ji, Q., Yonamine, Y., Wu, K. C. W., & Hill,

J. P. (2013). Layer-by-layer nanoarchitectonics: invention, innovation, and evolution. Chemistry Letters, 43(1), 36-68.

[4-34] Hao, C., Li, J., Liu, Y., Zhou, X., Liu, Y., Liu, R., ... & Xu, L. (2015). Superhydrophobic-like tunable droplet bouncing on slippery liquid interfaces. Nature communications, 6, 7986.

[4-35] Van Oss, C. J., Ju, L., Chaudhury, M. K., & Good, R. J. (1989). Estimation of the polar parameters of the surface tension of liquids by contact angle measurements on gels. Journal of Colloid and Interface Science, 128(2), 313-319.

[4-36] Mecozzi, S., West, A. P., & Dougherty, D. A. (1996). Cation-pi interactions in aromatics of biological and medicinal interest: electrostatic potential surfaces as a useful qualitative guide. Proceedings of the National Academy of Sciences, 93(20), 10566-10571.

[4-37] Fowkes, F. M. (1963). Additivity of intermolecular forces at interfaces. i. determination of the contribution to surface and interfacial tensions of dispersion forces in various liquids. The Journal of Physical Chemistry, 67(12), 2538-2541.

[4-38] Young, T. (1805). An essay on the cohesion of fluids. Philosophical Transactions of the Royal Society of London, 95, 65-87.

[4-39] Jenner, E., & D'Urso, B. (2013). Wetting states on structured immiscible liquid coated surfaces. Applied Physics Letters, 103(25), 251606.

[4-40] Solomon, B. R., Khalil, K. S., & Varanasi, K. K. (2014). Drag reduction using lubricant-impregnated surfaces in viscous laminar flow. Langmuir, 30(36), 10970-10976.

[4-41] Paxson, A. T., Yagüe, J. L., Gleason, K. K., & Varanasi, K. K. (2014). Stable dropwise condensation for enhancing heat transfer via the initiated chemical vapor deposition (iCVD) of grafted polymer films. Advanced Materials, 26(3), 418-423.

[4-42] Cao, M., Guo, D., Yu, C., Li, K., Liu, M., & Jiang, L. (2015). Water-repellent properties of superhydrophobic and lubricant-infused “slippery” surfaces: A brief study on the functions and applications. ACS applied materials & interfaces, 8(6), 3615-3623.

[4-43] Lv, J., Song, Y., Jiang, L., & Wang, J. (2014). Bio-inspired strategies for anti-icing. ACS nano, 8(4), 3152-3169.

[4-44] Howell, C., Vu, T. L., Lin, J. J., Kolle, S., Juthani, N., Watson, E., ... & Aizenberg, J. (2014). Self-replenishing vascularized fouling-release surfaces. ACS applied materials & interfaces, 6(15), 13299-13307.

Chapter 5 Anisotropic-wetting materials learned by water harvesting method of cactus *Cactaceae*

This chapter is based on [Tenjimbayashi, M., Higashi, M., Yamazaki, T., Takenaka, I., Matsubayashi, T., Moriya, T., ... & Shiratori, S. (2017). Droplet Motion Control on Dynamically Hydrophobic Patterned Surfaces as Multifunctional Liquid Manipulators. ACS applied materials & interfaces, 9(12), 10371-10377.]

5.1 Anisotropic wetting properties

Previous observation of wetting behavior has been done by static wetting analysis; For instance, (super)hydrophobicity and (super)hydrophilicity were classified according to static contact angle values. [1] Recently, the concept of dynamic wetting behaviors: continuous liquid wetting motions as a function of time are unavoidable to measure special wetting behaviors including anisotropic wetting (: droplet wets, spreads or moves directionally on materials). [2, 3] Anisotropic wetting behaviors has been researched because of their potential application such as fluidic system, [4, 5] water harvesting, [6, 7] heat transfer condensation, [8, 9] and patternable liquid layer formation. [10] Cactus *Cactaceae* spine in nature offered an idea to obtain anisotropic wetting materials. Cactus collects water droplet on tips of spine to the body using anisotropic wetting. Here, the chemical or morphological patterning or gradient surface gives an asymmetric droplet a directional driving force as shown in **Figure 5-1**. [11] Surface chemistry driven force ($F_{\text{chemistry}}$) can be described as $F_{\text{chemistry}} \sim \pi R_0 \gamma_{LV} (\cos\theta_B - \cos\theta_A)$, where R_0 and γ_{LV} are droplet radius, and the surface tension, θ_B and θ_A are contact angles on each area (**Figure 5-1A**). Morphology driven force ($F_{\text{morphology}}$) with spine model (**Figure 5-**

1B) is given by $F_{\text{morphology}} \sim -\int_{R_S}^{R_L} \frac{2\gamma}{(R(z)+R_0)^2} \sin\alpha \, dz$, where $R(z)$ is the local radius of the spine structured object; R_S, R_L are the spine radius contacting on two opposite sides of the droplet; and α is the half apex angle of the spine, dz is the minute incremental radius along the spine. In both cases of forces working toward droplets, droplets become asymmetric and a resistance force driven (F_{resist}) by droplet asymmetry works as like a friction yielding; $F_{\text{resist}} \sim \pi R_0 \gamma_{LV} (\cos\theta_{\text{rec}} - \cos\theta_{\text{adv}})$ where θ_{adv} and θ_{rec} are advancing/receding contact angles. It means the lower contact angle hysteresis ($\Delta\theta = \theta_{\text{adv}} - \theta_{\text{rec}}$) liquids get, the more easily liquids can move on the surface.

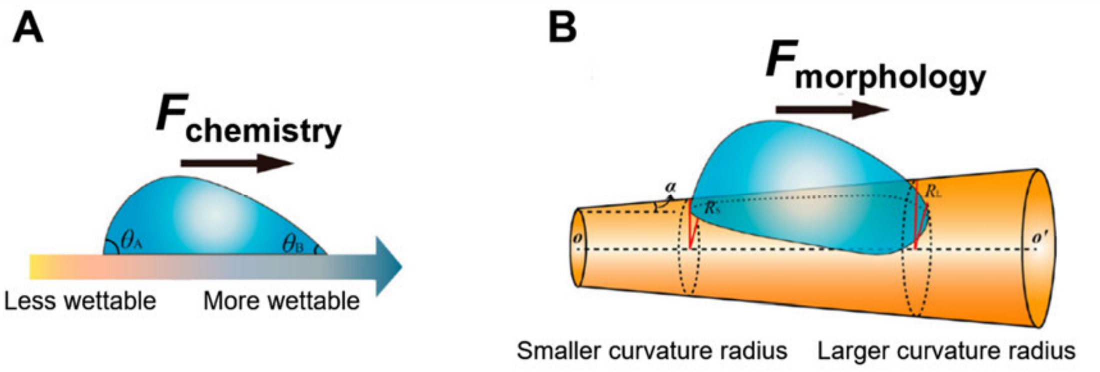

Figure 5-1. Schematic illustration of anisotropic wetting approaches. (A) surface chemistry driven force ($F_{\text{chemistry}}$) and (B) morphology driven force ($F_{\text{morphology}}$) work toward droplets on surfaces, respectively. The scheme is reproduced with the permissions. Copyright 2015, American Chemical Society [11].

Above mentioned approaches rely on adding directional force to the droplet. On the other hand, droplet motions can also be controlled by making use of pinning of the droplet (*i.e.* limiting specific directional movement) as shown in **Figure 5-2.** [12, 13] The droplet pinning works by morphological and/or chemical patterning as same as the Cactus spine dialogues. One way to restrict droplet motion is to design slope structure (**Figure 5-2A**). When a droplet comes on the slope surface (tilting angle: α), it cannot wet the slope area until its advancing contact angle gets larger than sum of slope angle and static contact angle (θ_s). The other way is to design patterning of surfaces with different wettability (**Figure 5-2B**). When a droplet comes on the surface 1, it cannot wet the surface 2 till its advancing contact angle on the surface 1 becomes higher than its static contact angle on the surface 2. The control of pinning of droplets (e.g. hydrophobic/hydrophilic patterning) enabled designs of various types of anisotropic wetting materials. [14-17]

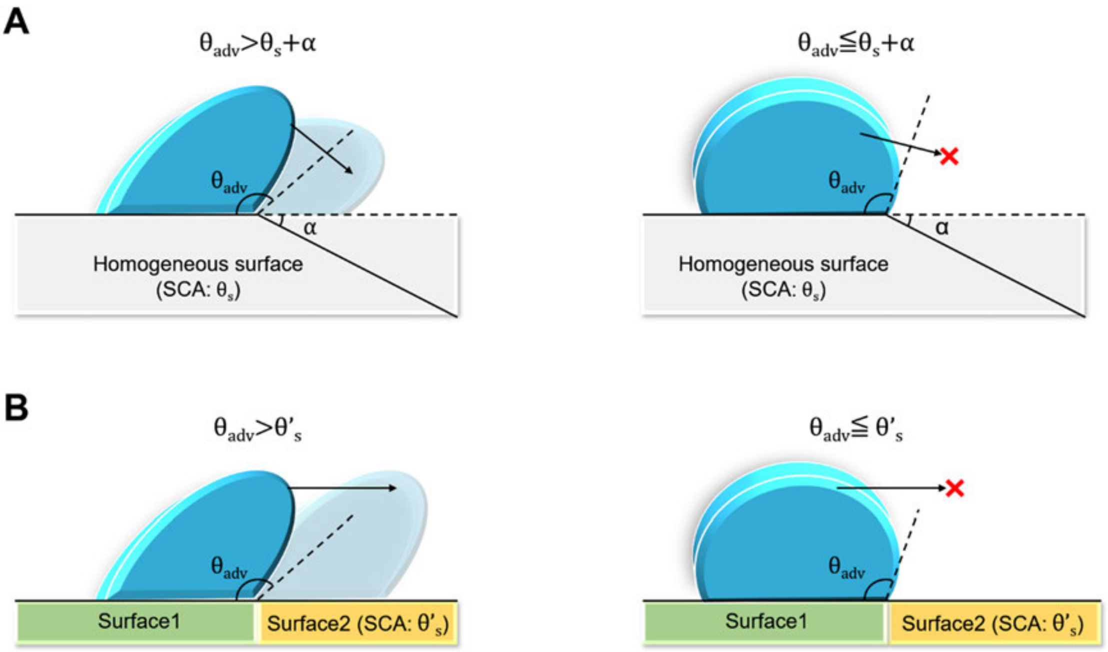

Figure 5-2. Schematic illustration of droplet motion is restricted by (A) morphological or (B) chemical heterogeneity of the surface. (A) When a droplet comes on the slope surface, it cannot wet the slope area until its advancing contact angle gets larger than sum of slope angle and static contact angle. (B) When a droplet comes on the surface 1, it cannot wet the surface 2 till its advancing contact angle on the surface 1 becomes higher than its static contact angle on the surface 2.

Despite the development of bioinspired anisotropic wetting materials, their droplet manipulations are usually based on the localized adhesion or pinning of droplets on materials surface and it is unavoidable that small droplets remains on the sticky area to decrease transport efficiency (see **Figure 4-5C** in Chapter 4). [12, 18] Thus in section 5.2, we introduce dynamically hydrophobic and statically hydrophobic/hydrophilic patterned surfaces, which can guide droplet motion whereas droplet not remain on surfaces; Thus, droplets can directionally wet on surfaces without losing their volume. We applied this technique to 100% yield micro-droplet reactor. This propose will be helpful to develop anisotropic wetting materials for practical use.

5.2 Droplet motion control on dynamically hydrophobic and statically hydrophobic/hydrophilic patterned surface

5.2.1 Introduction

Active surfaces having unique solid-liquid interactions are of both scientific and technological interest. In particular, anti-wetting surfaces that control liquid motion are attracting extensive attention because of their potential in industrial applications as fluidic devices and micro-reactors, [19] in addition to fundamental studies in areas such as, liquid transportation, [5, 20] controlled deposition [21] and as patterned devices. [22, 23] Such liquid manipulation techniques require composite hydrophobic/hydrophilic surfaces, where a patterned hydrophilic, high-adhesion area guides a droplet on a hydrophobic surface. Lai and co-workers reported a super-hydrophobic/hydrophilic patterned surface with photocatalytic TiO_2 nanotubes. [12] Manna and Lynn designed slippery liquid-infused porous surfaces (SLIPS) with a hydrophilic sticky area. [18] If applying hydrophobic/hydrophilic patterning surfaces to specific applications, for example, as the surface of a micro-reactor, then care must be taken to ensure that the surface can suitably guide a droplet over the hydrophobic area and to limit the contact of the droplet with the hydrophilic area so as not to decrease the transport efficiency. [24] Furthermore, challenges remain to improve liquid manipulative surface properties such as, transparency and mechanical durability, in addition to developing new routes to identify facile fabrication methods. [25–27]

Recently, dynamically hydrophobic surfaces have been introduced as third-generation anti-wetting surfaces, fabricated by covalently fixing flexible hydrophobic molecular chains on smooth surfaces to prevent the penetration of liquid into the coating. [28-30] These surfaces have shown the possibility to design statically hydrophilic but dynamically hydrophobic surfaces to control the adhesion of droplets so as not to deviate away from the hydrophobic path.

Herein, we introduce a novel liquid manipulation strategy to design dynamically hydrophobic and statically hydrophobic/hydrophilic patterned surfaces: two different hydrophobic molecular chains covalently fix to a smooth surface using an 'omniphobicity'-based patterning technique (details given below) *via* silane chemistry.[31, 32] The surfaces guide the sliding direction of a droplet in the presence of a statically hydrophilic area and simultaneously prevents the droplet from sticking on the transportation path. Furthermore, the smooth structure and chemical stability of the patterned surfaces provide high transparency and mechanical robustness to the surface. The concept of liquid manipulation by dynamically hydrophobic and statically hydrophobic/hydrophilic patterned surfaces have not been advanced; and hitherto is still a subject of intense investigation. Furthermore, for practical use, designing hydrophobic liquid manipulative surfaces *via* facile wet processes that study properties such as, transparency and durability, play an important role in optimizing structure-controlling methods that employ multi-step chemical modification.[33, 34] We believe that the omniphobic patterning concept when applied to designing a multi-functional, dynamically hydrophobic and statically hydrophobic/hydrophilic patterned surface offers potential in both fluidic applications and for the future development of materials engineering. [35]

5.2.2 Experimental

Materials. Decyltrimethoxysilane (DTMS, $(CH_3O)_3Si(CH_2)_9CH_3$), phenyltriethoxysilane (PTES, $(CH_3CH_2O)_3Si$-Ph) and hexyltrimethoxysilane (HTMS, $(CH_3O)_3Si(CH_2)_5CH_3$) were purchased from Shin-Etsu Chemical Co., Ltd. (Tokyo, Japan). Tetramethyl orthosilicate (TMOS, $Si(OCH_3)_4$) was purchased from Junsei Chemical Co., Ltd. (Tokyo, Japan). Tetraethyl orthosilicate (TEOS, $Si(OC_2H_5)_4$) was purchased from Wako Pure Chemical Industries, Ltd. (Osaka, Japan). Ethanol (CH_3CH_2OH, purity; 99.5 wt.%), hydrochloric acid aqueous (HCl, 35–37 wt.%), sodium hydroxide aqueous (NaOH, 5mol/L), potassium hydroxide (KOH), acetone (CH_3COCH_3), toluene (Ph-CH_3), thymol blue (TB) ($C_{27}H_{30}O_5S$) and bromothymol blue (BPB) ($C_{19}H_{10}Br_4O_5S$) were purchased from Kanto Chemical Co., Inc. (Tokyo, Japan). Hexadecane ($C_{16}H_{34}$), and isopropanol ($CH_3CH(OH)CH_3$) were purchased from Tokyo Chemical Industry Co., Ltd. (Tokyo, Japan). An Aquarius GS-500.CPW (Advantec Co., Saijo, Japan) purifier was used to generate deionized water (resistance ~18.2 MΩ). Glass substrates (76 × 26 mm) with a thickness of 1.0 mm and refractive index of 1.52 were purchased from Matsunami Glass Ind. Ltd. (Kishiwada, Japan).

Cocktail preparation. Ph- precursor solution, and C_{10}- precursor solution were prepared along with our previous work. [36] C_6- precursor was prepared by substituting the DTMS in the C_{10}- precursor with 0.3710 g of HTMS. TB solution and BPB solutions for reactor applications were prepared by dissolving 2 mg of TB or 1 mg of BPB, respectively, in 5 mL of deionized water. The pH values of the aqueous systems were adjusted by HCl and NaOH. An aqueous KOH solution for alkaline treatment was prepared by dissolving 1 wt.% KOH in IPA/deionized water (= 2: 3 w: w) mixture.

Fabrication of patterned smooth surfaces. Patterned smooth surfaces were fabricated by a two-step wet coating process as shown in **Figure 5-3**. In short, Ph and C_{10} terminated group patterned surfaces were designed by the following procedure:

First, a glass substrate was hydrophilized by KOH alkaline treatment (sonicated for 3 minutes, rinsed, sonicated for a further 3 minutes, rinsed for 1 minute before repeating) or UV-O_3 treatment with NL-UV253 (Shoko Scientific Co., Ltd., (formerly Japan Laser Electron), Kanagawa, Japan). Thereafter, a section of the glass was masked using PVC masking tape (N-380 PVC masking tape, Nitto Denko, Tokyo, Japan) and the C_{10}- precursor was spin coated onto the substrate at a speed of 1000 rpm for 5 s and then at 2000 rpm for 10 s so as to produce a patterned coating. After drying for 24 hours, the mask was peeled off and the Ph- precursor was spin coated onto the substrate at a speed of 1000 rpm for 5 s and then at 2000 rpm for 10 s using a K-359S1 instrument (Kyowa Riken Co., Ltd., Tokyo, Japan). Because of the omniphobicity of the C_{10}- tethered area, the location of the Ph- tethering to the substrate was only in the area where the masking tape had previously been, *i.e.* the Ph- precursor did not attach to the C_{10} tethered area. After drying for 24 hours, the patterned sample was washed with acetone or ethanol. The

C_6 and C_{10} terminated group patterned surfaces were designed following the same procedure, except for the replacement of the Ph- precursor with a C_6 precursor.

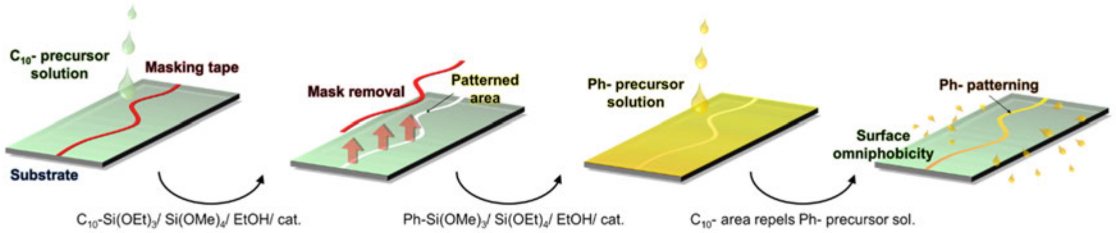

Figure 5-3. Schematic illustration of ‘omniphobicity’-based patterning to obtain an anisotropic wetting surface.

Characterization. SCA and SA were measured using a commercial contact angle (CA) system (FACE; Kyowa Interface Science Co., Ltd., Niiza, Japan). Dynamic contact angle (DCA) was measured by a tilted plate method using a high-speed camera (HAS-D3, Ditect, Tokyo, Japan). Each measurement was performed using 20 μL liquid droplets at room temperature (20 °C). Surface chemical contaminations were analyzed by EDX (QUANTAX 70; Bruker Nano GmbH, Berlin, Germany). The surface smoothness and the border of the patterned area was observed using a 3D laser scanning microscope (VK-9710, Keyence, Osaka, Japan) and a digital microscope (Dino-Lite AM2111 Series, AnMo Electronics Corporation, New Taipei, Taiwan). Optical measurements were performed using a spectrophotometer (UVmini-1240, Shimadzu, Kyoto, Japan) and a haze meter (NDH-5000, Nippon Denshoku Industries, Tokyo, Japan) with a white-light-emitting diode (5 V, 3 W) as the optical source. Mechanical durability was measured using an abrasion device (Tribogear Type 18L, Shinto Scientific Co., Ltd., Tokyo, Japan) under a pressure of 1 kPa. Cotton fabrics were used as the abrasive material. Flexibility was also measured by use of the same abrasion device.

5.2.3 Results and Discussion

Surface design and assessment of surface morphology. We designed a patterned hydrophobic functional tethered smooth surface comprising decyl (C_{10}-) and phenyl (Ph-) groups. C_{10}- and Ph- surfaces display statically hydrophobic and hydrophilic properties, respectively (i.e. static contact angle (SCA) θ_S = 96.93° on the surface of C_{10}-, 73.59° on the Ph- surface) whereas, the functional groups are dynamically hydrophobic having differences in their dynamic wettability to liquids that enables liquid manipulation through the Ph- tethered area. [12] The design procedure is shown in **Figure 5-3**. The transportation path of a liquid droplet is programmed by our proposed masking and coating method. A partially masked surface is coated by the C_{10}- precursor forming a partially C_{10}- tethered surface. Thereafter, the Ph- precursor is coated onto the surface. Here, the ‘omniphobicity’ of the C_{10}- tethered area prevents the Ph- precursor from reacting on the C_{10}- tethered area resulting in a ~1 μm thick tailored chemical modification layer having limited roughness and a near seamless patterned surface. This method allows facile fabrication of hydrophobic/hydrophilic patterned surfaces without the need for energy-consuming UV-O_3 or plasma treatments, whereby limitations exist as a result of precursor solution surface tension (**Figure 5-4A**). Surface morphologies of the C_{10}/Ph patterned surfaces are analyzed using a Dektak profilometer for thickness information (**Figure 5-4B**) and Laser microscopy for surface uniformity (**Figure 5-4C**).

Although the thickness of the patterned surface is ~1 µm on average, compared with the C_{10} area the thickness of the Ph area is ~0.1 µm higher. Furthermore, the height distribution over the Ph area forms curvatures similar to oleophilic wetting precursors having become a gel as in **Figure 5-4C**. These results show the possibility that the height gap between patterned areas can be controlled by liquid surface tension because it is possible to adjust the shape of the patterned area by varying the micro contact angle between the 'Ph precursor-C_{10} area-air' interfacial three-contact line as in **Figure 5-4A**. Such a novel coating strategy has potential in the design of micro-scale height controllable patterning methods. However further investigations into the effect of morphology as a function of surface tension are required.

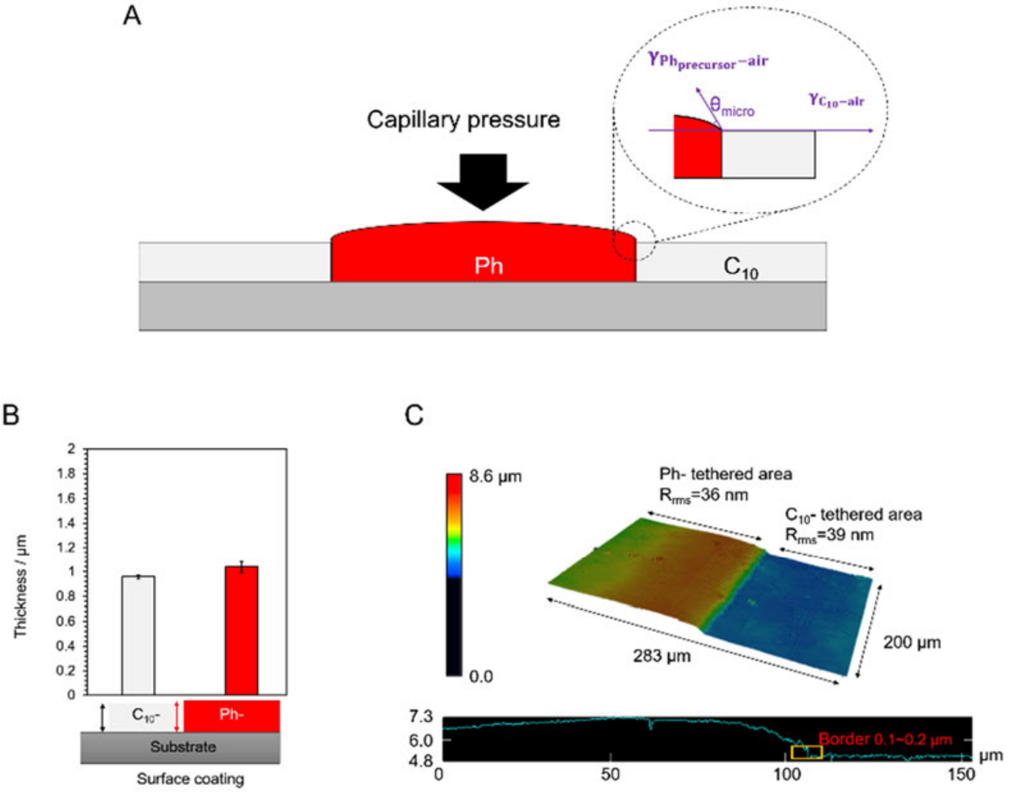

Figure 5-4. (A) Schematic images of the C_{10}/Ph patterned surface. The height gap is thought to be controlled by the surface energies of the precursor solution and omniphobic area. (B) Thickness of the C_{10} and Ph coating on the C_{10}/Ph patterned surface using a

Dektak profilometer over a scanning area of 0.5 mm employing 3000 plots per modified area. (C) Surface uniformity and height distribution measured by Laser microscopy.

Assessment of surface wettability. The difference in dynamic wettability is a result of the flexibility of the tethered molecules: the C_{10}- group is more flexible than the corresponding Ph- group because mobility of the Ph group is restricted by inter-π-π interactions. i.e. The XPS analysis (**Figure 4-2** in Chapter 4) revealed the presence of π electrons derived from satellite peaks on the Ph coating, which means that the flexibility of the hydrophobic molecules are limited by π-π interactions resulting in a decrease in the contact line movement—at least being more static than C_{10}). The surface has both C_{10}- and Ph- tethered areas, each of which possesses a different interfacial energy against a liquid droplet. Thus, the difference in wettability in each area of the patterned surface changes the water droplet asymmetry when moving over a solid-liquid contact line. The water droplet transport behavior and surface manipulation are shown in **Figure 5-5A–C**. While both the C_{10}- and Ph- tethered areas are hydrophobic, their dynamic contact angles (DCAs) are different: advancing/receding contact angles (CAs) and sliding angles (SAs) ($\theta_{adv}/\theta_{rec}/\alpha_S$) are (101.77°/93.91°/28.73°) on C_{10}- and (92.96°/62.89°/51.48°) on Ph-tethered areas, respectively (**Figure 5-5A**). Comparing CA hysteresis (=θ_{rec}-θ_{adv}) values and SA, the droplet adhesion force on the Ph- tethered area is found to be stronger than the corresponding C_{10}- tethered area. Thus, a water droplet crossing from the Ph- surface to the C_{10}- tethered area, requires energy driven by the curvature change of the droplet. Here, the net resistance force (mainly by frictional dissipation) for a moving contact line (F_{resist}) is given by:

$$F_{resist} = F_{gravity} + F_{\gamma} - F_{inertia} \qquad (1)$$

where $\mathrm{F_{gravity}}$ is the gravity derived force, $\mathrm{F_{\gamma}}$ is a surface tension derived force by asymmetry of the droplet shape, and $\mathrm{F_{inertia}}$ is the inertial force. Thus, under a state of equilibrium, the surface tilting angle (TA) is equal to SA ($\alpha = \alpha_S$),

$$\begin{aligned} \mathrm{F_{resist}} &= \mathrm{F_{gravity}} + \mathrm{F_{\gamma}} \\ &= \rho V g \sin\alpha_S + 2R\,\gamma_{LV}(\cos\theta_{rec} - \cos\theta_{adv}) \end{aligned} \tag{2}$$

where ρ and V are density and volume of a droplet, respectively. g is the gravitational acceleration constant. R is the liquid droplet radius in contact with the surface, and γ is interfacial tension. When a droplet is water, $\mathrm{F_{resist}}$ for C_{10}- and Ph- are obtained as 0.149 and 0.395 mN, respectively (**Figure 5-5A**). Therefore, a droplet is more stable on Ph- tethered areas with liquid motion restricted by the difference of $\mathrm{F_{resist}}$. **Figure 5-5B** shows the change in SA values as a function of the Ph- tethered path rotating angle (φ), resulting in a controlled droplet S-shape sliding direction along the Ph- tethered area as in **Figure 5-5C,** without contamination, even though the whole surface is dynamically hydrophobic **Figure 5-5D**. Here, the droplet transportation weight ratio was only slightly below 100% (see **Table 5-1**, **Figure 5-6**), and the average controlled water droplet sliding speed was 107.6 mm s^{-1}, which is significantly (at least 10 times) higher than recent representative liquid manipulation reports, even when considering variations in liquid volume and TA.[18,36] This is thought to result as conventional liquid manipulation has been performed by both statically and dynamically hydrophilic/hydrophobic patterning to limit droplet mobility.

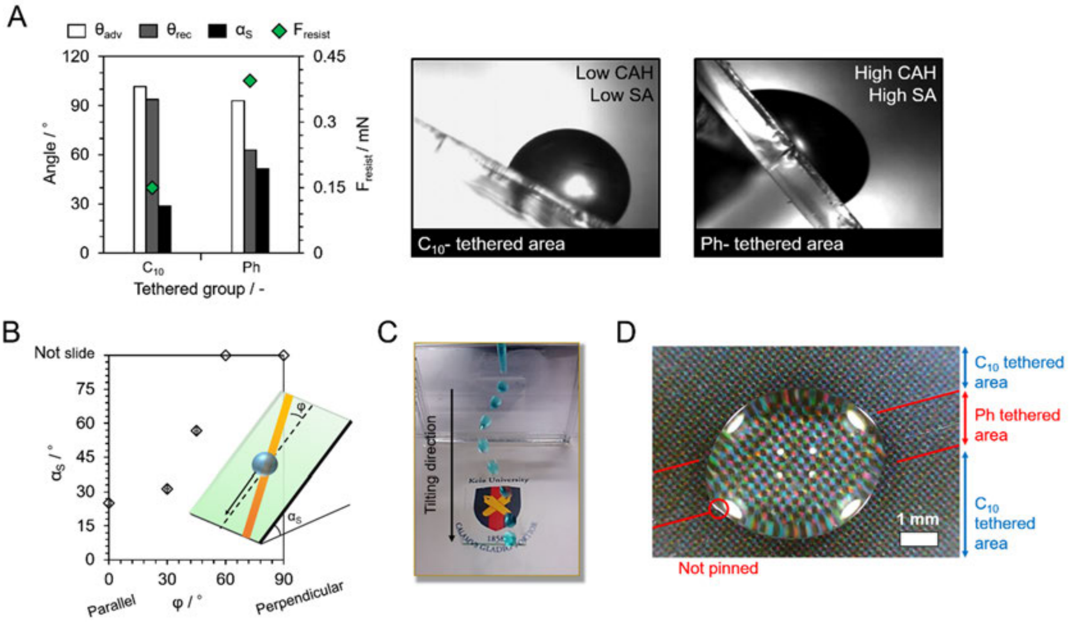

Figure 5-5. (A) Dynamic contact angles (DCAs) and sliding angles (SAs) of 10 μL water droplets with photographic images. These values were measured by a tilted plate method together with resistance force for a moving contact line. (B) Water SA on a 2 mm wide Ph- tethered path (yellow line in scheme) and C10- tethered remaining area, rotating the sliding direction from 0–90°. When the rotating angle (φ) is 0° (or 90°), droplet transportation on the Ph- tethered path follows a parallel (or perpendicular) direction. (C) Droplet motion control on Ph-/C10- patterned surface. (D) Photo image of a 20 μL water droplet on a Ph-/C10- patterned surface measured using a digital microscope.

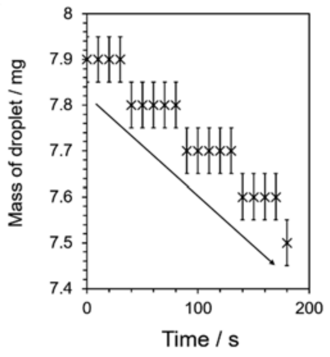

Figure 5-6. Change to the water droplet mass as a function of transportation time measured using an electronic balance with 0.1 mg accuracy at 28.3 °C, 49% relative humidity.

Table 5-1. Changes to water droplet masses before and after transportation over an 8 mm patterned surface for ~40 seconds. The mass of droplets and substrates were measured using an electronic balance (GR-200, A&D Co., Ltd., Tokyo, Japan) with 0.1 mg accuracy. Droplet yield was calculated by [Mass of droplet before manipulation] / [Mass of droplet after manipulation] × 100 [%]. Although, in theory, the material balance should be 100%, partial evaporation of a droplet decreases the yield as shown in **Figure 5-6**.

#	Mass substrate (g)	substrate + droplet (g)	droplet before manipulation (g)	remained droplet (g)	droplet after manipulation (g)	Yield (%)	MEAN (%)
1	3.3477	3.4367	0.0890	0.0006	0.0884	99.3258	99.2544
2	3.3475	3.4368	0.0893	0.0006	0.0887	99.3281	SD (%)
3	3.3476	3.4374	0.0898	0.0008	0.0890	99.1091	0.1258

Driven force analysis. We further studied the driving force change when droplet transportation overlaps the border from the Ph- tethered area to the C_{10}- tethered area (**Figure 5-7A**) to obtain the limitation of the liquid trapping force on the patterned surface as a function of droplet volume. Total force working on a stable droplet ($\mathrm{F_{total}}$) is calculated by:

$$\mathrm{F_{total}} = \mathrm{F_{gravity}} + \mathrm{F_{\gamma}} + \mathrm{F_{resist}} \qquad (3)$$

with the condition of $\mathrm{F_{inertia}} = 0$. Here, $\mathrm{F_{total}}$ depends on the composition of the patterned area that the drop is in contact with and changes to $\mathrm{F_{total}}$ are calculated as shown in **Figure 5-7B** (Calculation details for each force change are shown in next paragraph). Droplet transportation within the Ph- tethered area (dx<0, dx: the vertical overlapping distance of a droplet across the border on a patterned smooth surface), results in a constant $\mathrm{F_{total}}$ because of surface homogeneity. However, when a droplet overlaps the border of the Ph- and C_{10}- tethered areas (0<dx<2R ($\mathrm{R_{C_{10}}}$)), $\mathrm{F_{total}}$ suddenly decreases as the values of $\mathrm{F_{\gamma}}$ and $\mathrm{F_{resist}}$ change. When a droplet slides beyond the border (dx>2R) F_{total} recovers because the droplet contact area becomes homogeneous again. The graph in **Figure 5-7B** indicates that the F_{total} value can increase as a function of liquid volume and the maximum F_{total} value in the range of 0<dx<2R becomes positive when V = 80 μL, which is a critical droplet size between overlapping the C_{10}- and Ph- border and remaining in the desired area under this condition. We conducted further experiments to support this calculation to statically cast water droplets of various volumes on the tilted surface as shown in **Figure 5-7C**. As droplets cross the Ph- and C_{10}-tethered area border, 10–80 μL-sized droplets stop on the border (**Figure 5-7D**), whereas droplets ranging between 90–100 μL overlap beyond the border (**Figure 5-7E**).

Here, calculation details for each force change are shown as follows. In the case that the water droplet is in contact with the complex Ph-/C_{10}- surface, the total force applied to the droplet is given as follows in the equilibrium state:

$$F_{tot} = F_{gravity} + F_{\gamma} + F_{resist} \quad (\, F_{inertia} \approx 0 \text{ to be controlled}\,) \tag{4}$$

Where, $F_{gravity}$, F_{γ} and F_{resist} are written as:

$$F_{gravity} = \rho V g \sin\alpha \tag{5}$$

$$F_{\gamma} = \int \gamma_{SV} \cos\varphi R d\varphi + \int \gamma_{SL} \cos\varphi R d\varphi + \int \gamma_{LV} \cos\varphi \cos\theta R d\varphi \tag{6}$$

$$F_{resist} = \mu_{C_{10}} N_{C_{10}} + \mu_{Ph} N_{Ph} \tag{7}$$

The values of F_{γ} and F_{resist} depend on the area where the droplet is located. μ is the dynamic friction coefficient.

(i) When the droplet, as a whole, is located on the Ph-area, which means $dx < 0$, F_{γ} is obtained by:

$$\begin{aligned} F_{\gamma} &= \int \gamma_{SV} \cos\varphi R d\varphi + \int \gamma_{SL} \cos\varphi R d\varphi + \int \gamma_{LV} \cos\varphi \cos\theta R d\varphi \\ &= 2R_{Ph}\gamma_{LV}\left(\cos\theta_{rec}^{Ph} - \cos\theta_{adv}^{Ph}\right) \end{aligned} \tag{8}$$

Here, $R = R(\theta_S, V)$ is equal to

$$R(\theta_S, V) = \sin\theta_s \sqrt[3]{\frac{4V}{2\theta_S - \sin 2\theta_S}} \tag{9}$$

From the Young's equation, F_γ is given by equation (10) in the case that the droplet is in contact with both areas, which is equal to: $0 \le dx < 2R_{C_{10}}$.

(ii) When the droplets are in contact with both areas ($0 \le dx < 2R_{C_{10}}$), F_γ is given by the Young's equation as follows:

$$\begin{aligned} F_\gamma &= \int \gamma_{SV} \cos\varphi R d\varphi + \int \gamma_{SL} \cos\varphi R d\varphi + \int \gamma_{LV} \cos\varphi \cos\theta R d\varphi \\ &= 2R_{C_{10}}\left(\gamma_{SV}^{C_{10}} - \gamma_{SL}^{C_{10}} - \gamma_{LV}\cos\theta_{adv}^{C_{10}}\right) \\ &\qquad - 2R_{Ph}\left(\gamma_{SV}^{Ph} - \gamma_{SL}^{Ph} - \gamma_{LV}\cos\theta_{rec}^{Ph}\right) \\ &= 2R_{C_{10}}\gamma_{LV}(\cos\theta_S^{C_{10}} - \cos\theta_{adv}^{C_{10}}) - 2R_{Ph}\gamma_{LV}\left(\cos\theta_S^{Ph} - \cos\theta_{rec}^{Ph}\right) \end{aligned} \tag{10}$$

(iii) When the whole droplet is located on the C_{10}-area ($2R_{C_{10}} < dx$), we can calculate F_γ by the following equation.

$$\begin{aligned} F_\gamma &= \int \gamma_{SV} \cos\varphi R d\varphi + \int \gamma_{SL} \cos\varphi R d\varphi + \int \gamma_{LV} \cos\varphi \cos\theta R d\varphi \\ &= 2R_{C_{10}}\gamma_{LV}\left(\cos\theta_{rec}^{C_{10}} - \cos\theta_{adv}^{C_{10}}\right) \end{aligned} \tag{11}$$

To summarize equations (8) ~ (11), F_γ can be obtained by

$$F_\gamma = \begin{cases} 2R_{Ph}\gamma_{LV}\left(\cos\theta_{rec}^{Ph} - \cos\theta_{adv}^{Ph}\right) & dx < 0 \\ 2R_{C_{10}}\gamma_{LV}(\cos\theta_S^{C_{10}} - \cos\theta_{adv}^{C_{10}}) - 2R_{Ph}\gamma_{LV}\left(\cos\theta_S^{Ph} - \cos\theta_{rec}^{Ph}\right) & 0 \le dx < 2R_{C_{10}} \\ 2R_{C_{10}}\gamma_{LV}\left(\cos\theta_{rec}^{C_{10}} - \cos\theta_{adv}^{C_{10}}\right) & 2R_{C_{10}} \le dx \end{cases}$$

Conversely, F_{resist} is the frictional force of the complex surface of the Ph- and C_{10}-areas, which is given as:

$$F_{resist} = \mu_{C_{10}} N_{C_{10}} + \mu_{Ph} N_{Ph} \tag{12}$$

where μ is written as

$$\mu = \frac{F_{resist}^{eq}}{N_{resist}^{eq}} = \frac{\rho V g \sin\alpha_S + 2R\gamma_{LV}(\cos\theta_{rec} - \cos\theta_{adv})}{\rho V g \cos\theta_S - 4R\gamma_{LV}(\sin\theta_{rec} + \sin\theta_{adv})} \tag{13}$$

By applying equation (13) to both the Ph-area and C_{10}-areas, we calculated both $\mu_{C_{10}}$ and μ_{Ph}. $N_{C_{10}}$ and N_{Ph} can be expressed by both the gravity force and the interfacial forces between the contact line of the water droplet and the surface of the coating. Therefore, when the droplet moves over both areas: overlapping dx on the C_{10}- tethered area and overlapping dy on the Ph tethered area ($0 \leq dx < 2R_{C_{10}}$ and $0 \leq dy < 2R_{Ph}$), $N_{C_{10}}$ and N_{Ph} are given by equations (14) and (15) respectively.

$$N_{C_{10}}(\varphi_B) = \rho V_{C_{10}} g\cos\alpha_S - 2\left(R_{C_{10}} + dx\right)\gamma_{LV}\sin\theta_{adv}^{C_{10}} \tag{14}$$

$$N_{Ph}(\varphi_B) = \rho V_{Ph} g\cos\alpha_S - 2(R_{Ph} + dy)\gamma_{LV}\sin\theta_{adv}^{Ph} \tag{15}$$

However, the relationship between dy and dx is given by:

$$dy = \frac{V - \frac{2R^2}{\sin\theta_S^{C_{10}}}\left(1 - \cos\theta_S^{C_{10}}\right)dx}{\frac{2R^2}{\sin\theta_S^{Ph}}\left(1 - \cos\theta_S^{Ph}\right)} \tag{16}$$

Additionally, $V_{C_{10}}$ and V_{Ph} are given using similar equations as followings:

$$V_{C_{10}} + V_{Ph} = V \tag{17}$$

$$\begin{aligned} V_{C_{10}} : V_{Ph} &= 2R_{C_{10}}\int_0^{\theta_S} \frac{\sin\theta}{\sin\theta_S} R d\theta dx : \ 2R_{Ph}\int_0^{\theta_S} \frac{\sin\theta}{\sin\theta_S} R d\theta dy \\ &= \frac{2R_{C_{10}}^2(1 - \cos\theta_S)dx}{\sin\theta_S} : \frac{2R_{Ph}^2(1 - \cos\theta_S)dy}{\sin\theta_S} = R_{C_{10}}^2 dx : R_{Ph}^2 dy \end{aligned} \tag{18}$$

$$V_{C_{10}} = \frac{R_{C_{10}}^2 dx}{R_{C_{10}}^2 dx + R_{Ph}^2 dy} \times V \tag{19}$$

$$V_{Ph} = \frac{R_{Ph}^2 dy}{R_{C_{10}}^2 dx + R_{Ph}^2 dy} \times V \tag{20}$$

When all of the droplet is located on the Ph-area ($dx < 0$)F_{resist} is written as equation (21) with vertical components of interfacial tension.

$$\begin{aligned} F_{resist} &= \mu_{C_{10}} N_{C_{10}} + \mu_{Ph} N_{Ph} \\ &= \mu_{Ph}\{\rho V g \cos\alpha_S - 2R_{Ph}\gamma_{LV}(\sin\theta_{adv}^{Ph} + \sin\theta_{rec}^{Ph})\} \end{aligned} \tag{21}$$

When the droplet is in contact with both areas ($0 \leq dx < 2R_{C_{10}}$ and $0 < dy \leq 2R_{Ph}$), F_{γ} is given by:

$$\begin{aligned} F_{resist} &= \mu_{C_{10}} N_{C_{10}} + \mu_{Ph} N_{Ph} \\ &= \mu_{C_{10}}\left\{\rho\left(\frac{R_{C_{10}}^2 dx}{R_{C_{10}}^2 dx + R_{Ph}^2 dy} \times V\right) g\cos\alpha_S \right. \\ &\qquad \left. - 2\left(R_{C_{10}} + dx\right)\gamma_{LV}\sin\theta_{adv}^{C_{10}}\right\} \\ &\quad + \mu_{Ph}\left\{\rho\left(\frac{R_{Ph}^2 dy}{R_{C_{10}}^2 dx + R_{Ph}^2 dy} \times V\right) g\cos\alpha_S \right. \\ &\qquad \left. - 2(R_{Ph} + dy)\gamma_{LV}\sin\theta_{adv}^{Ph}\right\} \end{aligned} \tag{22}$$

Additionally, if the whole of the droplet is located on the C_{10}-area only, ($2R_{C_{10}} < dx$), we can calculate F_{resist} as in equation (23):

$$\begin{aligned} F_{resist} &= \mu_{C_{10}} N_{C_{10}} + \mu_{Ph} N_{Ph} \\ &= \mu_{C_{10}}\{\rho V g \cos\alpha_S - 2R_{C_{10}}\gamma_{LV}(\sin\theta_{adv}^{C_{10}} + \sin\theta_{rec}^{C_{10}})\} \end{aligned} \tag{23}$$

To summarize equations (21) ~ (23), F_{resist} is written as:

$$F_{resist} = \begin{cases} \mu_{Ph}\{\rho V g\cos\alpha_S - 2R_{Ph}\gamma_{LV}(\sin\theta_{adv}^{Ph} + \sin\theta_{rec}^{Ph})\} & dx < 0 \\ \mu_{C_{10}}\{\rho V_{C_{10}} g\cos\alpha_S - 2\left(R_{C_{10}} + dx\right)\gamma_{LV}\sin\theta_{adv}^{C_{10}}\} & \\ \quad + \mu_{Ph}\{\rho V_{Ph} g\cos\alpha_S - 2(R_{Ph} + dy)\gamma_{LV}\sin\theta_{adv}^{Ph}\} & 0 \leq dx < 2R_{C_{10}} \\ \mu_{C_{10}}\{\rho V g\cos\alpha_S - 2R_{C_{10}}\gamma_{LV}(\sin\theta_{adv}^{C_{10}} + \sin\theta_{rec}^{C_{10}})\} & 2R_{C_{10}} \leq dx \end{cases}$$

The calculated values for each force change with volume as a function of dx are shown in **Figure 5-7F-I**. It is apparent that $F_{gravity}$ increases with droplet volume, and the values are constant regardless of dx and in whole positive to the tilting direction (**Figure 5-7F**). F_{γ} increases with droplet volume because of an increase of liquid-vapor-solid contact line, and they decrease to almost 0 when droplet across the border ($0 \leq dx < 2R_{C_{10}}$); When droplets lie on homogeneous surface, F_{γ} is in theory constant (**Figure 5-7G**). The friction by F_{resist} in whole negative with any droplet volume and position. Effect of friction is getting larger as the increase of volume along with the droplet-surface contacting area, and the strongest friction occurs when a droplet comes across the border (**Figure 5-7H**). Hence, the total force becomes positive when surface homogeneous to increase the kinetic energy and the energy is dissipated and droplet stops in the border. Therefore, the condition that governs if droplets do not overlap beyond the potential is given by:

$$E_W < \int_0^{2R} F_{total} dx \tag{24}$$

Where E_W is the kinetic energy of a droplet in the area of dx = 0. This equation also indicates that a droplet stops overlapping when x' satisfies $E_W = \int_0^{x'} F_{total} dx$. Interestingly, 10–80 µL-sized droplets refrain from crossing the border area rather than remaining in contact with it (see **Figure 5-7C**). This is a new discovery. The patterned smooth surfaces herein do not obey the classical pinning theory law: liquid is pinned as the droplet head reaches the border with the condition: $\theta_{adv}^{Ph}(dx = 0) < \theta_{S}^{C_{10}}$.[37] In fact, our analysis considers not only θ_{adv}^{Ph} and $\theta_{S}^{C_{10}}$ but also $\theta_{adv}^{C_{10}}$, $\theta_{S}^{C_{10}}$, θ_{rec}^{Ph}, and θ_{S}^{Ph} as follows:

$$\begin{aligned} F_{\gamma} = {} & 2R_{C_{10}}\gamma_{LV}\left(\cos\theta_{S}^{C_{10}} - \cos\theta_{adv}^{C_{10}}\right) \\ & - 2R_{Ph}\gamma_{LV}\left(\cos\theta_{S}^{Ph} - \cos\theta_{rec}^{Ph}\right) \end{aligned} \tag{25}$$

Therefore, E_W depends on various parameters such as, transportation path width, φ, TA and liquid volume, which can be optimized depending on the path design.

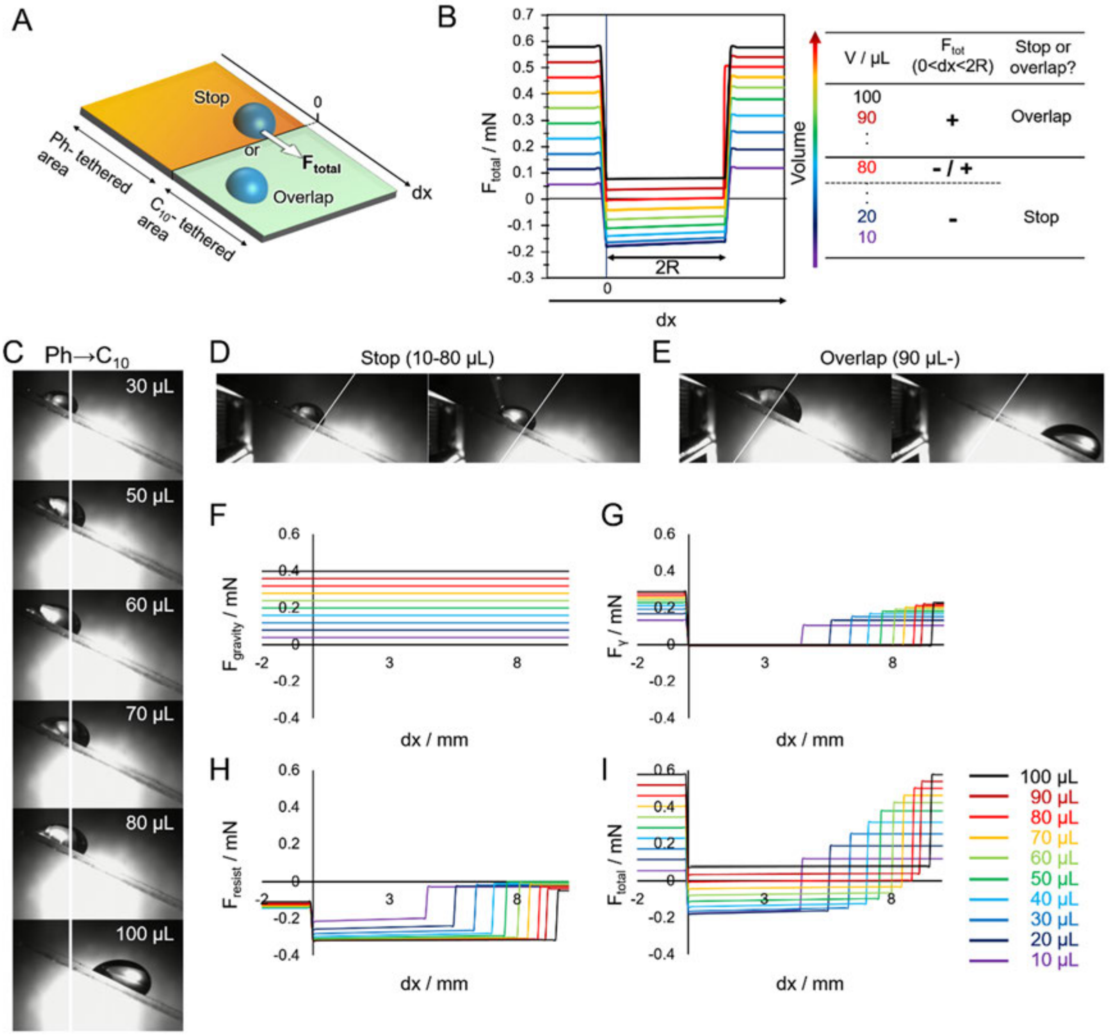

Figure 5-7. Total force, F_{total}, analysis between the water droplet and the C_{10}- and Ph-tethered border area (see scheme in (A)). (B) graph showing total liquid droplet force as a function of volume when the head of a droplet overlaps, dx, on the border oriented perpendicular to the trajectory tilting at 24° with photographic images in (C). When V is greater (less) than 80 μL as in (D), F_{total} on the border becomes positive (negative) and the droplets larger than 80 μL overlap beyond the border as in (E), whereas droplet sizes under this threshold level stop on the border. (F)-(I) Driven force analysis between the water droplet and the C_{10}- and Ph- tethered border area as a function of liquid droplet volume when a tip of a droplet overlaps, dx, on the border oriented perpendicular to the trajectory tilting at 24°.

Application of liquid remaining-free micro-reactor system. We applied this liquid manipulation system to a micro-fluid reactor. When two micro-volume droplets slide on two separate non-parallel paths, the coalescence of droplets, if miscible, can occur at the intersection. **Figure 5-8A** shows SAs of various micro-volume water droplets on the patterned surface as a function of path width parallel to the sliding direction. Here, the condition of TA for droplet transportation is $\alpha_S < \alpha$ as long as the droplets do not completely overlap the border. For practical use, the droplet volume can be modified by its use, whereas the TA value is usually fixed. Notably, when the droplet volume range lies between 0–40 μL, the liquid-manipulating surfaces herein show controllable SAs with respect to φ and path width (see **Figure 5-5B**). The liquid manipulation studies have shown that the optimized V-patterned path (see **Figure 5-8B**) works as a micro-reactor as shown in **Figure 5-8C**, **D**. As the patterned smooth surface is durable to both acidic and basic liquids (see **Figure 5-8E, F**), the acidic aqueous (pH = 2.13) reaction with bromophenol blue (BPB) succeeded as the droplet transportation remained on the hydrophobic patterned surface (**Figure 5-8C**), and the basic aqueous (pH = 13.06) reaction with thymol blue (TB) also succeeded in a similar manner (**Figure 5-8D**). Surface contaminations after the reaction were confirmed by energy-dispersive x-ray (EDX) spectroscopy and compared with the dynamically hydrophilic surface (**Figure 5-9A, B**), indicating no observed contamination on the dynamically hydrophobic surfaces.

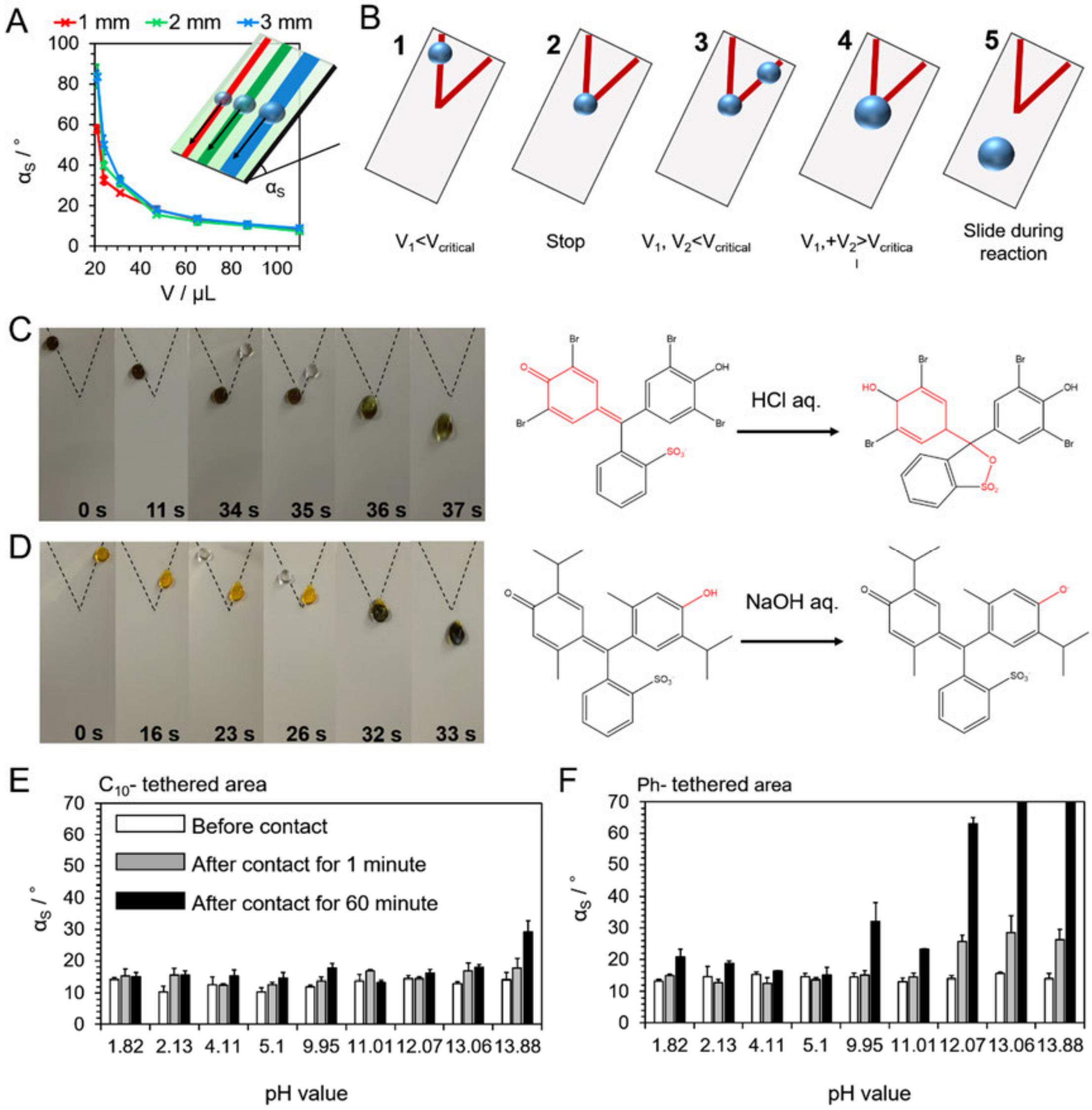

Figure 5-8. (A) Study of various volume water droplet sliding on patterned surfaces with the width of the Ph- tethered area ranging between 1–3 mm. When the volume of the droplet is <40 µL, the SA of the micro-droplet can be controlled by the width of the Ph-tethered area. (B) Reaction procedure on V shape patterned surfaces. Based on its volume, a reactant is transported in a downward motion, is captured, and not until coalescing with another reactant is the downward motion continued under the conditions of: V_1, V_2<$V_{critical}$ and V_1+V_2>$V_{critical}$. (C-D) Time-elapsed photo images of a micro-reactor application under acidic and basic conditions: (C) Bromophenol blue (BPB) protonation by hydrochloric acid aqueous solution with a pH value of 2.13 (V = 25 µL, TA = 40°, φ = 18°, path width = 1 mm (right), 2 mm (left)) and (D) Thymol blue (TB) deprotonation by sodium hydroxide aqueous solution with a pH value of 13.06 (V = 35 µL, TA = 60°, φ

= 18°, path width = 1 mm (right), 2 mm (left)). (E-F) Surface durability under acidic or basic conditions of the (E) C_{10}- and (F) Ph- tethered area. SAs of 10 µL aqueous droplets as a function of pH are measured on each surface after contacting for 0, 1 or 60 minutes. When the surfaces are applied to a micro-reactor, the liquid-solid contact time must be <1 min. Thus, the surfaces are sufficiently durable for the application.

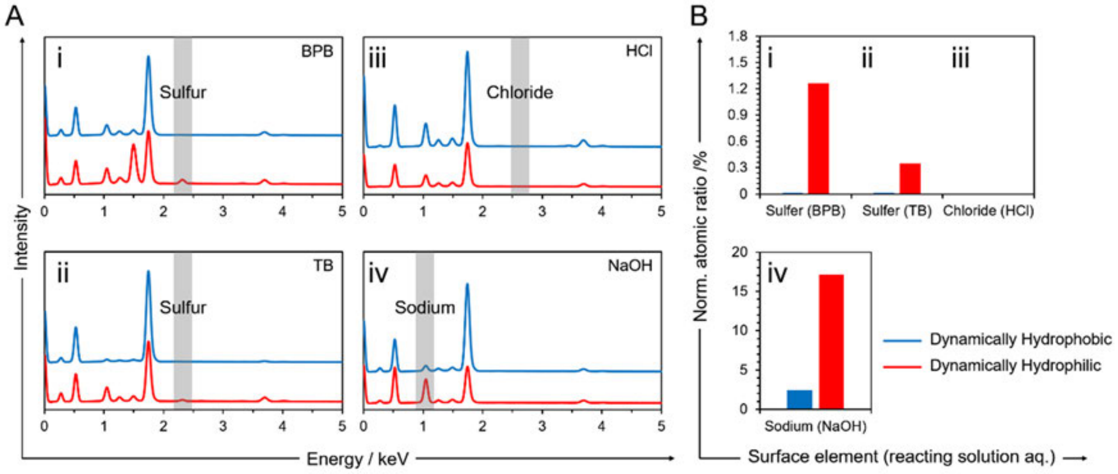

Figure 5-9. (A) EDX spectra and (B) Elemental contamination presented by normalized atomic ratios of a dynamically hydrophobic patterned surface (blue) and a dynamically hydrophilic surface (-OH tethered surface, red) after casting aqueous droplets of BPB (i), TB (ii), HCl (iii) and NaOH (iv), respectively. Because of the volatility of aqueous HCl, the chloride peaks were not observed after aqueous HCl contamination. Although sodium peaks were observed on both surfaces, the peaks were derived from Na_2O in the substrate.

Furthermore, we demonstrate omniphobic liquid manipulation—controlling not only water but also organic solvents by replacing the Ph- tethered smooth surface with a C_6- tethered counterpart (**Figure 5-10A**). **Figure 5-10B** shows FT-IR spectrum whose doublet peaks of C_6 and C_{10} coatings around 2850 cm^{-1} and 2930 cm^{-1} are shifted by Δ = 6 cm^{-1} and Δ = 3 cm^{-1}, respectively, signifying a difference for each alkyl chain movement. Additionally, the intensity of the C_{10} doublet peak ratio around 2930 cm^{-1} is clearly higher than that of C_6, indicating enhanced mobility of the C_{10} molecules compared with C_6 molecules. Thus, they exhibit a suitable difference of DCAs against a wider range of target liquids (see **Figure 5-11A-H**). As a result, diagonal sliding of three solvent types are realized on the surface as shown in **Figure 5-11I–K**. This technique can be utilized across a wider variety of micro-fluidic applications. For more versatile use of liquid manipulation, we measured the transport range of aqueous droplets having different viscosities by adjusting the water/sodium alginate mixture ratio, resulting in droplet viscosities in the range of <28 cP (see **Figure 5-12**).

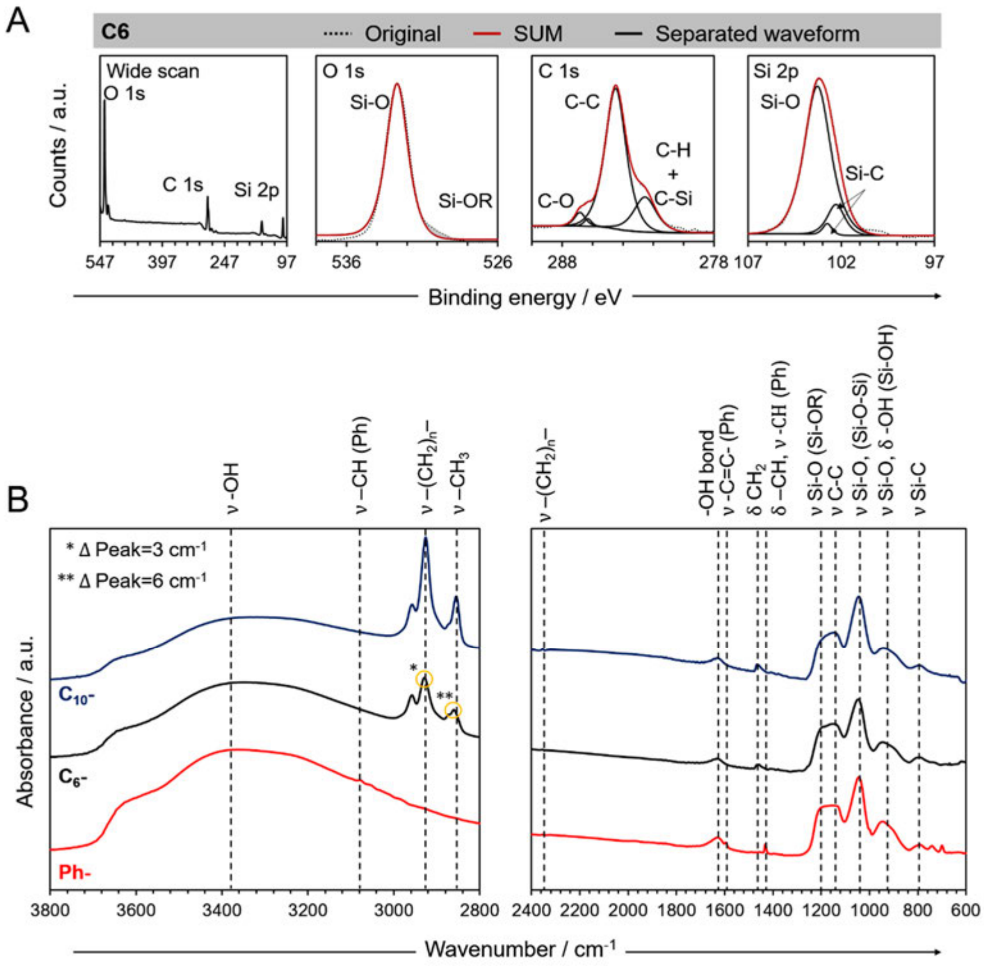

Figure 5-10. (A) Wide-range x-ray photoelectron spectroscopy (XPS) analysis of the C_6-coatings showing the O_{1s}, C_{1s}, and Si_{2p} spectra employing an MgKα laser (see **Figure 4-2** in Chapter 4 for XPS analysis of the Ph-, C_{10}- area). (B) FTIR attenuated total reflection spectra of C_{10} (blue), C_6 (Black), and Ph (red) modified Si-wafer surfaces. The peak shifts * and ** (circled yellow) are based on the C_{10} spectra.

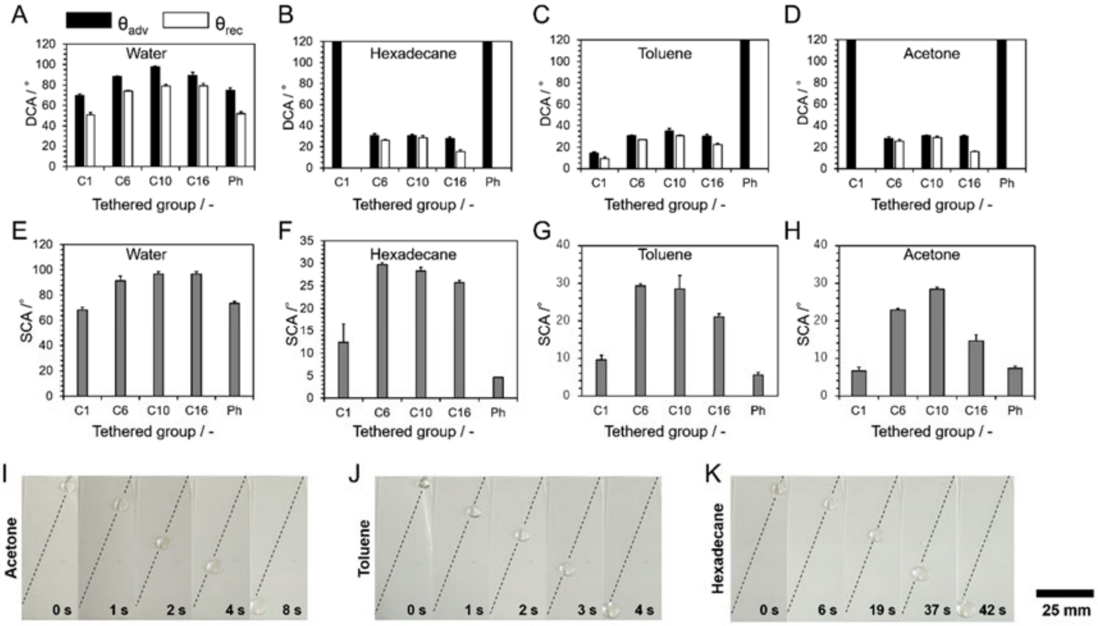

Figure 5-11. Solvent droplets motion control. (A-D) Dynamic contact angles and (E-H) static CAs of various liquids on various functional tethered smooth surfaces. Based on this study, we adapted C_6-/C_{10}- patterning for solvent manipulation. (I–K) Time-elapsed photo images of omniphobic liquid manipulation by replacing the Ph- tethered area with a C_6- tethered area to realize diagonal sliding of (I) acetone, (J) toluene, and (K) hexadecane (V = 10 μL, TA = 8°, φ = 20°, path width = 1 mm).

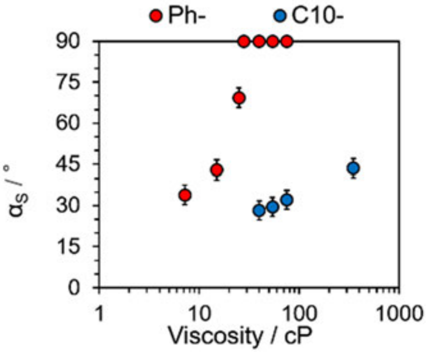

Figure 5-12. SAs of 10 μL aqueous droplets as a function of aqueous liquid viscosity adjusted by mixing sodium alginate with water.

Transparency and mechanical robustness of patterned surface. Liquid manipulative techniques have been developed to improve surface smoothness while simultaneously adding mechanical robustness and a transparency to the surface, offering advantages over conventional liquid manipulation techniques. The relief structure normally consists of a nano-micro scale roughened surface, whose high surface roughness causes a transmittance decrease by increasing scattering, as predicted by the optical theory:

$$\mathrm{In}(\mathrm{T}/\mathrm{T}_0) \propto (\sigma/\lambda)^2 \qquad (7)$$

where T and T_0 are transmittance of the surface with and without surface roughness, respectively. σ is the root mean square surface roughness (R_{rms}), and λ is the wavelength. Thus, the smoothness of the patterned surface prevents surface scattering and maintains high transmittance as shown in **Figure 5-13A–D**. Additionally, the patterned structure retains wettability even after being subjected to an abrasion test over 1000 times (**Figure 5-14A**) and 100 cycles of bending-stretching (**Figure 5-14B**) because of the structural robustness. [29] Liquid manipulative behaviors on complex bent coatings were also confirmed as shown in **Figure 5-14C**.

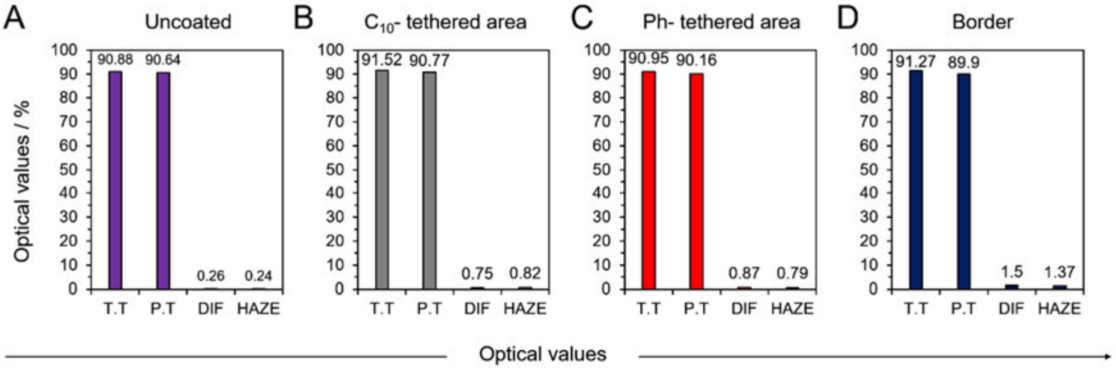

Figure 5-13. Optical analysis of (A) uncoated area, (B) C_{10}- tethered area, (C) Ph-tethered area, and (D) the interfacial border on the patterned smooth surface measured by total transmittance (TT), parallel transmittance (PT), haze (HAZE), and diffusion (DIF). PT means the degree of light that passes through a sample within a small angle range (<15°). The HAZE value is given by haze (%) = DIF/TT × 100.

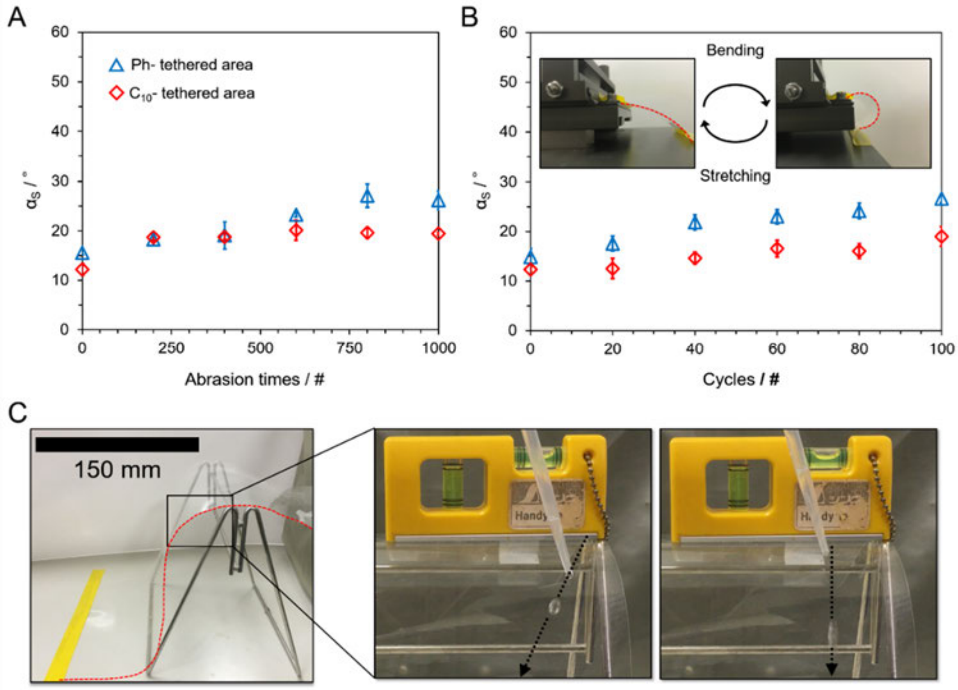

Figure 5-14. (A) Mechanical durability analysis measured by abrasion time versus SA of a 10 μL water droplet. (B-C) Flexibility of the patterned smooth surface coated on a polyethylene terephthalate (PET) film. (B) Quantification of bending resistance measured by bending times versus SA of a 10 μL water droplet. (C) Photographic images indicating that the water droplet can diagonally slide on the bent patterned smooth surface while the water droplet can perpendicularly slide on the C_{10}- tethered area.

5.2.4 Conclusions

In summary, our dynamically hydrophobic and statically hydrophobic/hydrophilic patterned transparent smooth surfaces are capable of high speed water manipulation with tunable and anisotropic sliding, durable against both acidic and basic conditions, and even show the potential for omniphobic manipulation. Furthermore, the smoothness of the patterned surface displays excellent transparency and flexibility properties, and performed well against durability testing of abrasion and bending, which extends these materials across a wide range of applications. Additionally, we also observed that the mechanism of liquid trapping on the border is different to conventional understandings:

the droplet transport stops as the droplet is pinned to its path even as the droplet head reaches the border, which indicates a droplet kinetic energy of zero, which can improve the interfacial dynamics. This new strategy of liquid manipulation displaying a near 100% yield as a multi-functional fluidic device can help future scientific development and expand into new industrial applications.

References

[5-1] Good, R. J. (1992). Contact angle, wetting, and adhesion: a critical review. Journal of adhesion science and technology, 6(12), 1269-1302.

[5-2] Gleiche, M., Chi, L. F., & Fuchs, H. (2000). Nanoscopic channel lattices with controlled anisotropic wetting. Nature, 403(6766), 173-175.

[5-3] Xia, D., & Brueck, S. R. J. (2008). Strongly anisotropic wetting on one-dimensional nanopatterned surfaces. Nano letters, 8(9), 2819-2824.

[5-4] Hou, Y. P., Feng, S. L., Dai, L. M., & Zheng, Y. M. (2016). Droplet Manipulation on Wettable Gradient Surfaces with Micro-/Nano-Hierarchical Structure. Chem. Mater, 28, 3625-3629.

[5-5] Guo, T., Che, P., Heng, L., Fan, L., & Jiang, L. (2016). Anisotropic Slippery Surfaces: Electric-Driven Smart Control of a Drop's Slide. Advanced Materials, 28(32), 6999-7007.

[5-6] Zhang, S., Huang, J., Chen, Z., & Lai, Y. (2016). Bioinspired Special Wettability Surfaces: From Fundamental Research to Water Harvesting Applications. Small, 13(3), 1602992.

[5-7] Xu, T., Lin, Y., Zhang, M., Shi, W., & Zheng, Y. (2016). High-Efficiency Fog Collector: Water Unidirectional Transport on Heterogeneous Rough Conical Wires. ACS nano, 10(12), 10681-10688.

[5-8] Sharma, C. S., Combe, J., Giger, M., Emmerich, T., & Poulikakos, D. (2017). Growth Rates and Spontaneous Navigation of Condensate Droplets Through Randomly Structured Textures. ACS nano, 11(2), 1673-1682.

[5-9] Chu, F., Wu, X., Zhu, B., & Zhang, X. (2016). Self-propelled droplet behavior during condensation on superhydrophobic surfaces. Applied Physics Letters, 108(19), 194103.

[5-10] Fang, C. K., Ko, H. C., Yang, C. W., Lu, Y. H., & Hwang, S. (2016). Nucleation processes of nanobubbles at a solid/water interface. Scientific reports, 6, 24651.

[5-11] Ju, J., Zheng, Y., & Jiang, L. (2014). Bioinspired one-dimensional materials for directional liquid transport. Accounts of chemical research, 47(8), 2342-2352.

[5-12] Lai, Y., Pan, F., Xu, C., Fuchs, H., & Chi, L. (2013). In Situ Surface-Modification-Induced Superhydrophobic Patterns with Reversible Wettability and Adhesion. Advanced Materials, 25(12), 1682-1686.

[5-13] Ghosh, S., Lagraauw, R., Otten, S., Pit, A., Berendsen, C., Zeegers, J., ... & Mugele, F. (2014). Trapping of drops by wetting defects. Nature communications, 5, 3559.

[5-14] Chung, J. Y., Youngblood, J. P., & Stafford, C. M. (2007). Anisotropic wetting on tunable micro-wrinkled surfaces. Soft Matter, 3(9), 1163-1169.

[5-15] Chen, Y., He, B., Lee, J., & Patankar, N. A. (2005). Anisotropy in the wetting of rough surfaces. Journal of colloid and interface science, 281(2), 458-464.

[5-16] Malvadkar, N. A., Hancock, M. J., Sekeroglu, K., Dressick, W. J., & Demirel, M. C. (2010). An engineered anisotropic nanofilm with unidirectional wetting properties. Nature materials, 9(12), 1023-1028.

[5-17] Kwak, M. K., Jeong, H. E., Kim, T. I., Yoon, H., & Suh, K. Y. (2010). Bio-inspired slanted polymer nanohairs for anisotropic wetting and directional dry adhesion. Soft Matter, 6(9), 1849-1857.

[5-18] Manna, U., & Lynn, D. M. (2015). Fabrication of Liquid-Infused Surfaces Using Reactive Polymer Multilayers: Principles for Manipulating the Behaviors and Mobilities of Aqueous Fluids on Slippery Liquid Interfaces. Advanced Materials, 27(19), 3007-3012.

[5-19] Xue, Y., Wang, H., Zhao, Y., Dai, L., Feng, L., Wang, X., & Lin, T. (2010). Magnetic liquid marbles: a “precise” miniature reactor. Advanced materials, 22(43), 4814-4818.

[5-20] Chen, H., Zhang, P., Zhang, L., Liu, H., Jiang, Y., Zhang, D., ... & Jiang, L. (2016). Continuous directional water transport on the peristome surface of Nepenthes alata. Nature, 532(7597), 85-89.

[5-21] Golovin, K., Lee, D. H., Mabry, J. M., & Tuteja, A. (2013). Transparent, Flexible, Superomniphobic Surfaces with Ultra-Low Contact Angle Hysteresis. Angewandte Chemie, 125(49), 13245-13249.

[5-22] Yamada, K., Henares, T. G., Suzuki, K., & Citterio, D. (2015). Paper-Based Inkjet-Printed Microfluidic Analytical Devices. Angewandte Chemie International Edition, 54(18), 5294-5310.

[5-23] Burgess, I. B., Mishchenko, L., Hatton, B. D., Kolle, M., Loncar, M., & Aizenberg, J. (2011). Encoding complex wettability patterns in chemically functionalized 3D photonic crystals. Journal of the American Chemical Society, 133(32), 12430-12432.

[5-24] Watts, P., & Haswell, S. J. (2005). The application of micro reactors for organic synthesis. Chemical Society Reviews, 34(3), 235-246.

[5-25] You, I., Lee, T. G., Nam, Y. S., & Lee, H. (2014). Fabrication of a micro-omnifluidic device by omniphilic/omniphobic patterning on nanostructured surfaces. ACS nano, 8(9), 9016-9024.

[5-26] Tian, D., Zhang, N., Zheng, X., Hou, G., Tian, Y., Du, Y., ... & Dou, S. X. (2016).

Fast responsive and controllable liquid transport on a magnetic fluid/nanoarray composite interface. ACS nano, 10(6), 6220-6226.

[5-27] Verho, T., Bower, C., Andrew, P., Franssila, S., Ikkala, O., & Ras, R. H. (2011). Mechanically durable superhydrophobic surfaces. Advanced Materials, 23(5), 673-678.

[5-28] Rabnawaz, M., Liu, G., & Hu, H. (2015). Fluorine-Free Anti-Smudge Polyurethane Coatings. Angewandte Chemie, 127(43), 12913-12918.

[5-29] Wang, L., & McCarthy, T. J. (2016). Covalently attached liquids: instant omniphobic surfaces with unprecedented repellency. Angewandte Chemie, 128(1), 252-256.

[5-30] Cheng, D. F., Urata, C., Yagihashi, M., & Hozumi, A. (2012). A statically oleophilic but dynamically oleophobic smooth nonperfluorinated surface. Angewandte Chemie International Edition, 51(12), 2956-2959.

[5-31] Urata, C., Masheder, B., Cheng, D. F., & Hozumi, A. (2012). How to reduce resistance to movement of alkane liquid drops across tilted surfaces without relying on surface roughening and perfluorination. Langmuir, 28(51), 17681-17689.

[5-32] Vogel, N., Belisle, R. A., Hatton, B., Wong, T. S., & Aizenberg, J. (2013). Transparency and damage tolerance of patternable omniphobic lubricated surfaces based on inverse colloidal monolayers. Nature communications, 4, 2176.

[5-33] Tian, X., Shaw, S., Lind, K. R., & Cademartiri, L. (2016). Thermal processing of silicones for green, scalable, and healable superhydrophobic coatings. Advanced Materials, 28(19), 3677-3682.

[5-34] Tenjimbayashi, M., Sasaki, K., Matsubayashi, T., Abe, J., Manabe, K., Nishioka, S., & Shiratori, S. (2016). A biologically inspired attachable, self-standing nanofibrous membrane for versatile use in oil–water separation. Nanoscale, 8(21), 10922-10927.

[5-35] Ariga, K., Li, J., Fei, J., Ji, Q., & Hill, J. P. (2016). Nanoarchitectonics for Dynamic Functional Materials from Atomic-/Molecular-Level Manipulation to Macroscopic Action. Advanced Materials, 28(6), 1251-1286.

[5-36] Kamei, J., & Yabu, H. (2015). On-Demand Liquid Transportation Using Bioinspired Omniphobic Lubricated Surfaces Based on Self-Organized Honeycomb and Pincushion Films. Advanced Functional Materials, 25(27), 4195-4201.

[5-37] Ghosh, S., Lagraauw, R., Otten, S., Pit, A., Berendsen, C., Zeegers, J., ... & Mugele, F. (2014). Trapping of drops by wetting defects. Nature communications, 5, 3559.

Chapter 6 Summary

6.1 Summary and outlook

In this thesis, biomimetic approaches to design functional materials for practical application were studied. Especially, highly motivated by nature systems which control surface wettability, the biomimetic materials with anti-wetting (hydrophobicity), selective-wetting (hydrophobicity and superoleophilicity), slippery-wetting (slipperiness on liquid surfaces), and anisotropic-wetting (directional droplet motion) properties were designed and developed for the applications to anti-fouling coatings, biomedical sensors, oil/water separation systems, and microfluidic devices.

Firstly, how the biomimetics impact on materials engineering field was overviewed for the research motivation. A number of peer-reviewed publications including the keyword of biomimetics had been exponentially increased with years, indicating the strong demands of biomimetic approaches for designing the materials and/or systems. Thus, learned by a lotus *Nymphaea* leaf, a spider *Uloborus Walckenaerius*, a pitcher plant *Nepenthes rafflesiana Jack*, a cactus *Cactaceae*, the functional wettable materials were designed by controlling surface chemistry, molecular- and nano-scale structure.

Secondly, anti-wetting coatings inspired by lotus *Nymphaea* leaf were designed using self-assembly of hydrophobic SiO_2 nanoparticles (NPs), and their mechanical durability was enhanced by the addition of Ethyl-alpha-Cyanoacrylate (Et-CA) as an adhesive resin. We considered 4 types of structures by NPs/Et-CA composite: (1) single layer NPs coating by a single step spray method, (2) NPs/Resin composite coating by spraying NPs/Resin mixture, (3) NPs and resin double layer coating by double steps spray method, and (4) the NPs/Resin gradient coating by newly proposed single step movable spray method, respectively. The comparison revealed the best composite structure in terms of mechanical durability had been the NPs/Resin gradient coating. The proposed structured surface performed the strongest abrasion resistance in lotus inspired materials. In addition, the facile process (one step spray method), substrate selectivity (available to woods, glasses, and metals) contribute to the development in industry.

Lotus also offered an idea of developing biosensors. Optical electrode, which determinates ion level in liquids by color changes has developed as a visually available diagnosis kit. However, the dirty sample determination must interfere the accurate determination. Thus, potassium ion sensor in blood with blood contamination resistance are designed as rarely reported examples of application which combines anti-fouling surface function with the optical sensor. While in most previous reports adapted poly(vinyl chloride) (PVC) as based polymer, the fluorinated co-polymer: poly(vinylidene fluoride-co-hexafluoropropylene) (PVDF-HFP) have been used owing to its low surface energy over PVC. Even though surface anti-wetting properties has been enhanced by the change of base polymer, the sensing ability did not deteriorate whereas the blood fouling resistance improved. This PVDF-HFP based optical electrode contributes to the development of sensing materials targeting contaminated samples thanks to its hydrophobicity.

Thirdly, selective-wetting hydrophobic and superoleophilic materials were designed to help a solution of environmentally serious oil spill accidents in a sea. Inspired by an impeding mechanism of a spider *Uloborus Walckenaerius*, whose web can capture any insect using electrostatic force, electrostatically attachable self-standing nanofiber sheet (NF-S) with selective wettability were designed by electrospinning PVDF-HFP and Et-CA mixture. The merit of NF-S is scalable, low cost, and attachable to both 2D and 3D materials, whereas the conventional approach to this required chemical interaction or physical cross-linking between the supporting material and the functional material; thus, such type of versatile attachment has been difficult. NF-S performed over 99% separation efficiency to various oil/water mixtures including emulsified oil. In addition, the NF-S covered with melamine sponge made it possible to collect and extract an oil from an oil-water mixture. Thus, this work will contribute to solving oil spill accident. Furthermore, from the viewpoint of materials engineering insight, that is, the possibility of designing advanced materials by combining different functional materials; In this work, the high absorption capacity by the melamine sponge and the selective wettability by NF-Ss are combined to be an oil-absorbent.

Fourthly, slippery wetting surfaces were designed from the inspiration that a pitcher plant *Nepenthes rafflesiana Jack* wet their leaves with lubricating oil to make insects slide down into their digestive juices. Here, SPLASH (surface with π-interaction liquid adsorption, smoothness, and hydrophobicity) was designed using silane technology as an advanced slippery surface. Conventional slippery surfaces relied on a aporous base layer (BL) for immobilization of lubricating liquid; thus, the hydrophobicity, durability, and transparency were deteriorated due to the roughness exposure with the decrease of the liquid layer (LL) by evaporation or contact. However, thanks to the smoothness of BL, SPLASH kept the hydrophobicity, transparency, and durability regardless of the LL thickness. Moreover, since the smoothness of the BL enhanced the fluidity of LL, SPLASH performed the advantage over conventional surfaces in terms of hydrophobic properties. I’m sure that SPLASH: next age hydrophobic fluidic surface will offer big effect not only on industry but on whole materials engineering.

Fifthly, inspired by directional liquid transportation on a spine of cactus *Cactaceae*, anisotropic-wetting surfaces were designed by dynamically hydrophobic and statically hydrophobic/hydrophilic patterned surfaces using silane technology. The patterned surfaces performed high speed water manipulation with tunable and anisotropic sliding, durable against both acidic and basic conditions, and even performed the potential for omniphobic manipulation. In addition to the wettability, the surface performed transparency and mechanical robustness, and was available on a flexible substrate. Such multi-functional droplet transportation system will contribute to a design of advanced fluidic materials. It also will be helpful to design liquid replenishing system to SPLASH forming long-term stable slippery coatings.

Finally, the future prospect of biomimetic functional materials is discussed as a conclusion of this thesis. On one hand, studies of biomimetic functional materials rely on new discovery and development of nature systems. As our technology of molecular and nanoscale science develops, nature systems also advance through fierce struggles for survival. Therefore, we must develop materials not only for practical use but also strongly contribute to the advancement of materials chemistry and physics so as not to get a late start than nature evolution as well as the struggles. On the other hand, recently biomimetic approaches to design multi-functional materials have been developed via the rational integration of nature unique properties. For example, Aizenberg group developed highly efficient vapor condensation system by integrating three natural examples, i.e. water harvesting of desert beetle, anisotropic wetting of cactus spine, and slipperiness of pitcher plant. [1] Jiang group developed magnetic force driven morphological change of butterfly wing inspired structure to nepenthes surface. [2] In our case, the integration of pitcher plant inspired SPLASH technique (see Chapter 4) with cactus spine inspired liquid manipulation technique (see Chapter 5) will develop long-term stable SPLASH coating by self-replenishing liquid layer. To be summarized, advance of biomimetics depends on discovery of raveled nature system, development of nano- molecular science, and integration of nature species.

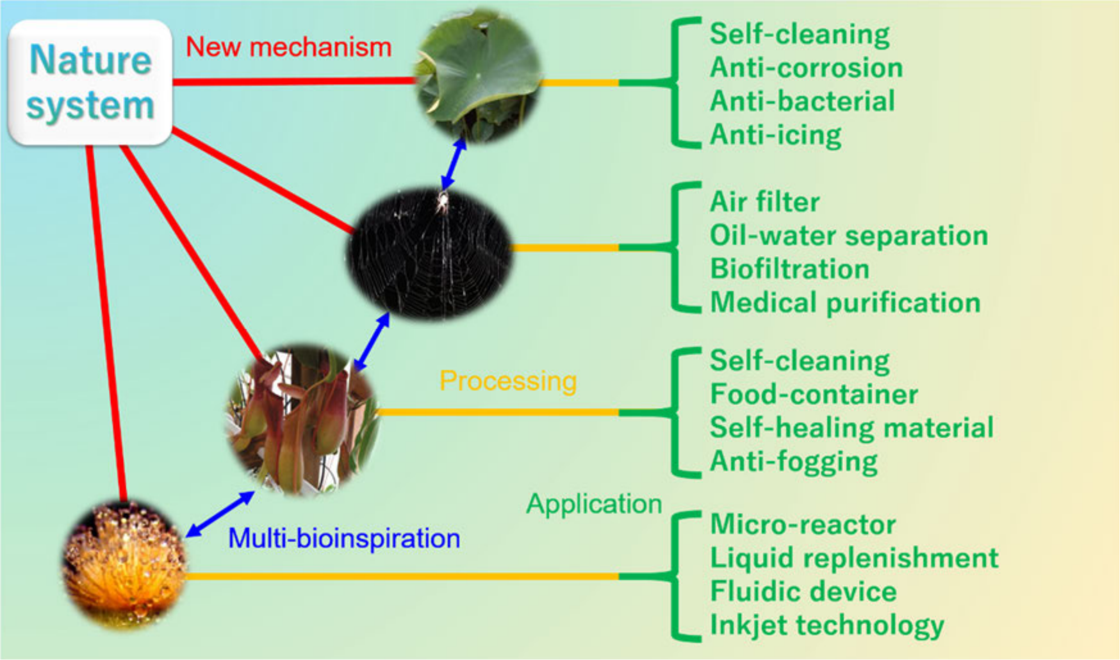

Figure 6-1. Summary of conclusion. The inserted pictures are reproduced with the permissions. Copyright 2015, American Chemical Society [3]. Copyright 2015, American Chemical Society [4]. Copyright 2016, American Chemical Society [5]. Copyright 2014, American Chemical Society [6].

References

[6-1] Park, K. C., Kim, P., He, N., & Aizenberg, J. (2015). Condensation on slippery asymmetric bumps. Nature, 531(7592), 78-82.

[6-2] Cao, M., Jin, X., Peng, Y., Yu, C., Li, K., Liu, K., & Jiang, L. (2017). Unidirectional Wetting Properties on Multi-Bioinspired Magnetocontrollable Slippery Microcilia. Advanced Materials.

[6-3] Yamamoto, M., Nishikawa, N., Mayama, H., Nonomura, Y., Yokojima, S., Nakamura, S., & Uchida, K. (2015). Theoretical explanation of the lotus effect: superhydrophobic property changes by removal of nanostructures from the surface of a lotus leaf. Langmuir, 31(26), 7355-7363.

[6-4] Singh, N., Mondal, D., Sharma, M., Devkar, R. V., Dubey, S., & Prasad, K. (2015). Sustainable Processing and Synthesis of Nontoxic and Antibacterial Magnetic Nanocomposite from Spider Silk in Neoteric Solvents. ACS Sustainable Chemistry & Engineering, 3(10), 2575-2581.

[6-5] Lee, L., Zhang, Y., Ozar, B., Sensen, C. W., & Schriemer, D. C. (2016). Carnivorous nutrition in pitcher plants (Nepenthes spp.) via an unusual complement of endogenous enzymes. Journal of proteome research, 15(9), 3108-3117.

[6-6] Ju, J., Zheng, Y., & Jiang, L. (2014). Bioinspired one-dimensional materials for directional liquid transport. Accounts of chemical research, 47(8), 2342-2352.

Appendix

Main Publications

(1) Mizuki Tenjimbayashi, Sachiko Nishioka, Yuta Kobayashi, Koki Kawase, Jiatu Li, Jyunichiro Abe, Seimei Shiratori, A Lubricant-Sandwiched Coating with Long-Term Stable Anticorrosion Performance, (Under review).

(2) Mizuki Tenjimbayashi, Takeshi Matsubayashi, Takeo Moriya, Seimei Shiratori, Bioinspired Hand-operated Smart-wetting Systems Using Smooth Thin Liquid Coatings, Langmuir, American Chemical Society (2017, In press).

(3) Mizuki Tenjimbayashi, Masaki Higashi, Taku Yamazaki, Issei Takenaka, Takeshi Matsubayashi, Takeo Moriya, Masatsugu Komine, Ryohei Yoshikawa, Kengo Manabe, and Seimei Shiratori, Droplet Motion Control on Dynamically Hydrophobic Patterned Surfaces as Multifunctional Liquid Manipulators, ACS Applied Materials & Interfaces, American Chemical Society 9, 10371-10377 (2017).

(4) Mizuki Tenjimbayashi, Ryo Togasawa, Kengo Manabe, Takeshi Matsubayashi, Takeo Moriya, Masatsugu Komine, and Seimei Shiratori, Liquid-infused smooth coating with transparency, super-durability, and extraordinary hydrophobicity, Advanced Functional Materials, Wiley-VCH Verlag GmbH & Co. KGaA, 26, 6693-6702 (2016).

(5) Mizuki Tenjimbayashi, Kaichi Sasaki, Takeshi Matsubayashi, Jyunichiro Abe, Kengo Manabe, Sachiko Nishioka, and Seimei Shiratori, A biologically inspired attachable, self-standing nanofibrous membrane for versatile use in oil–water separation, Nanoscale, Royal Society of Chemistry, 8, 10922-10927 (2016).

(6) Mizuki Tenjimbayashi, Hirokazu Komatsu, Masaaki Akamatsu, Waka Nakanishi, Koji Suzuki, Jonathan P. Hill, Seimei Shiratori, and Katsuhiko Ariga, Determination of blood potassium using a fouling-resistant PVDF-HFP-based optode, RSC advances, Royal Society of Chemistry, 6, 14261-14265 (2016).

(7) Mizuki Tenjimbayashi, and Seimei Shiratori, High durability superhydrophobic coatings with gradient density by one-step spraying, Journal of Applied Physics, American Institute of Physics, 116, 114310 (2014).

Other Publications

(1) Jun Muto, Jun-Yong Park, Mizuki Tenjimbayashi, Seimei Shiratori, Coagulation Performance of Bipolar Forceps with Superhydrophobic Coating, (submitted).

(2) Hirotaka Tsuchiya, Mizuki Tenjimbayashi, Ryohei Yoshikawa, Kaichi Sasaki, Ryo Togasawa, Takeo Moriya, Taku Yamazaki, Kengo Manabe, Seimei Shiratori, Liquid-infused Smooth Surface for Improved Condensation Heat Transfer, (revised).

(3) Takeshi Matsubayashi, Mizuki Tenjimbayashi, Masatsugu Komine, Kengo Manabe, Seimei Shiratori, Bio-inspired Hydrogel-Coated Mesh with Superhydrophilicity and Underwater Superoleophobicity for Efficient and Ultrafast Oil/Water Separation in Harsh Environments, Industrial & Engineering Chemistry Research, American Chemical Society 56, 7080-7085 (2017).

(4) Taichi Nakashima, Mizuki Tenjimbayashi, Takeshi Matsubayashi, Kengo Manabe, Masato Fujita, Takeshi Kamiya, Tsunetoshi Honda, Seimei Shiratori, Oleophobic/Adhesive Janus Self-Standing Films Modified with Bifurcated Short Fluorocarbon Chains as Transparent Oil Stain-free Coating with Attachability, Industrial & Engineering Chemistry Research, American Chemical Society 56, 3928-3936 (2017).

(５) Hirotaka Tsuchiya, Kengo Manabe, Thomas Gaudelet, Takeo Moriya, Ken Suwabe, Mizuki Tenjimbayashi, Kyu-Hong Kyung, Frèdèric Gillot, and Seimei Shiratori, Improvement of heat transfer by promoting dropwise condensation using electrospun polytetrafluoroethylene thin films, New Journal of Chemistry, Royal Society of Chemistry, 41, 982-991 (2017).

(６) Kengo Manabe, Chie Tanaka, Yukari Moriyama, Mizuki Tenjimbayashi, Chiaki Nakamura, Yuki Tokura, Takeshi Matsubayashi, Kyu-Hong Kyung, and Seimei Shiratori, Chitin-Nanofibers Extracted from Crab Shells in Broadband Visible Anti-Reflection Coatings with Controlling Layer-by-Layer Deposition and the Application for Durable Anti-Fog Surfaces, ACS Applied Materials & Interfaces, American Chemical Society, 8, 31951–31958 (2016).

(７) Takeo Moriya, Kengo Manabe, Mizuki Tenjimbayashi, Ken Suwabe, Hirotaka Tsuchiya, Takeshi Matsubayashi, Walter Navarrini, and Seimei Shiratori, A superrepellent coating with dynamic fluorine chains for frosting suppression: effects of polarity, coalescence and ice nucleation free energy barrier, RSC advances, Royal Society of Chemistry, 6, 92197-92205 (2016).

(８) Kengo Manabe, Takeshi Matsubayashi, Mizuki Tenjimbayashi, Takeo Moriya, Yousuke Tsuge, Kyu-Hong Kyung, and Seimei Shiratori, Controllable Broadband Optical Transparency and Wettability Switching of Temperature-Activated Solid/Liquid-Infused Nanofibrous Membranes, ACS Nano American Chemical Society, 10, 9387-9396 (2016).

(９) Takeshi Matsubayashi, Mizuki Tenjimbayashi, Kengo Manabe, Masatsugu Komine, Walter Navarrini, and Seimei Shiratori, Integrated Anti-icing Property of Super-repellency and Electrothermogenesis Exhibited by PEDOT:PSS/Cyanoacrylate Composite Nanoparticles, ACS Applied Materials & Interfaces, American Chemical Society, 8, 24212-24220 (2016).

(１０) Sachiko Nishioka, Mizuki Tenjimbayashi, Kengo Manabe, Takeshi Matsubayashi, Ken Suwabe, and Seimei Shiratori, Facile design of plant-oil-infused fine surface asperity for transparent antifouling endoscope lens, RSC advances, Royal Society of Chemistry, 6, 47579-47587 (2016).

(１１) Jyunichiro Abe, Mizuki Tenjimbayashi, and Seimei Shiratori, Electrospun Nanofiber Gel-SLIPS Exhibiting High Total Transparency and Scattering, RSC advances, Royal Society of Chemistry, 6, 38018-38023 (2016).

(１２) Takeshi Matsubayashi, Mizuki Tenjimbayashi, Kengo Manabe, Kyu-Hong Kyung, Bin Ding, and Seimei Shiratori, A Facile Method for Synthesizing Size-controlled Hollow Cyanoacrylate Nanoparticles with Multi-phase Separation, RSC advances, Royal Society of Chemistry, 6, 15877-15883 (2016).

(１３) Kaichi Sasaki, Mizuki Tenjimbayashi, Kengo Manabe, and Seimei Shiratori, Asymmetric Superhydrophobic/Superhydrophilic Cotton Fabrics Designed by Spraying Polymer and Nanoparticles, ACS Applied Materials & Interfaces, American Chemical Society, 8, 651-659 (2015).

(１４) Naoyuki Yokoi, Kengo Manabe, Mizuki Tenjimbayashi, and Seimei Shiratori, Optically transparent superhydrophobic surfaces with enhanced mechanical abrasion resistance enabled by mesh structure, ACS Applied Materials & Interfaces, American Chemical Society, 7, 4809 (2015).

Proceedings

(1) Mizuki Tenjimbayashi, Naoyuki Yokoi, Seimei Shiratori, Highly Durable Superhydrophobic Coating with Gradient Density Polymer Structure, Asian Workshop on Polymer Processing 2014, Kenting, Taiwan, 56#1075, Nov. 18, 2014.

(2) Takeshi Matsubayashi, Mizuki Tenjimbayashi, Seimei Shiratori, Fabrication of Semi-transparent Highly Oleophobic Films with Hollow Cyanoacrylate Nanoparticles, Asian Workshop on Polymer Processing 2014, Kenting, Taiwan, 56#1088, Nov. 18, 2014.

(3) Naoyuki Yokoi, Mizuki Tenjimbayashi, Seimei Shiratori, Highly Transparent Robust Superhydrophobic Polyester Mesh, Asian Workshop on Polymer Processing 2014, Kenting, Taiwan, 56#1076, Nov. 18, 2014.

International Conference

(1) Mizuki Tenjimbayashi, Ryo Togasawa, Masaki Higashi, Seimei Shiratori, Control of dynamic wetting behaviors on smooth surface for liquid manipulator and slippery surface with multi functionality, 253rd American Chemical Society NATIONAL MEETING & EXPOSITION, San Francisco, USA, April 2, 3 (Sci-mix), 2017.

(2) Mizuki Tenjimbayashi, Kaichi Sasaki, Jyunichiro Abe, Seimei Shiratori, *Uloborus walckenaerius* bioinspired attachable self-standing nanofibrous membrane for versatile use in oil–water separation, 253rd American Chemical Society NATIONAL MEETING & EXPOSITION, San Francisco, USA, April 2, 2017.

(3) T. Yamazaki, T. Moriya, T. Matsubayashi, M. Komine, M. Tenjimbayashi, S. Shiratori, Fabrication of antifreeze infused hydrophilic polymer/nanoparticle composite anti-icing coating for solar cells via spray Layer by Layer method, 253rd American Chemical Society NATIONAL MEETING & EXPOSITION, San Francisco, USA, April 2, 2017.

(4) Jiatu Li, Mizuki Tenjimbayashi, Seimei Shiratori, Single step dipping method of fabricating Fe3O4/PVDF-HFP composite porous material for magnetically controllable oil-water separation, 253rd American Chemical Society NATIONAL MEETING & EXPOSITION, San Francisco, USA, April 2, 2017.

(5) R. Togasawa, M. Tenjimbayashi, T. Matsubayashi, T. Moriya, K. Fujimoto, S. Shiratori, Fluorine-Free Slippery Surface with Hot Water Repellency and Durability against Boiling, The Materials Research Society of Japan, Yokohama, Japan, December 20, 2016.

(6) T. Moriya, M. Tenjimbayashi, T. Yamazaki, M. Komine, S. Shiratori, Hydrophobic liquid infused smooth surface for ice adhesion resistant coating., The Materials Research Society of Japan, Yokohama, Japan, December 20, 2016.

(7) T. Yamazaki, T. Moriya, T. Matsubayashi, M. Tenjimbayashi, S. Shiratori, Fabrication of highly transparent hydrophilic anti-icing coating for solar cells, 26th The Materials Research Society of Japan, Yokohama, Japan, December 20, 2016.

（8） M. Higashi, M. Tenjimbayashi, S. Shiratori, Liquid manipulation on dynamically hydrophobic patterned surface, 26th The Materials Research Society of Japan, Yokohama, Japan, December 20, 2016.

（9） Jiatu Li, Mizuki Tenjimbayashi, Takeshi Matsubayashi, and Seimei Shiratori, Magnetic force driven remote controllable oil absorbents fabricated by one-step dipping technique, 26th The Materials Research Society of Japan, Yokohama, Japan, December 19, 2016.

（１０） Hirotaka Tsuchiya, Mizuki Tenjimbayashi, Ryo Togasawa, Takeo Moriya, Kyu-Hong Kyung, and Seimei Shiratori, Liquid-infused Smooth Surface for Improvement of Condensation Heat Transfer, 26th The Materials Research Society of Japan, Yokohama, Japan, December 19, 2016.

（１１） Kaichi Sasaki, Mizuki Tenjimbayashi, Kengo Manabe, and Seimei Shiratori, Hydrophobic liquid infused surfactant-added surfaces with anti-fouling and anti-microbial property, 26th The Materials Research Society of Japan, Yokohama, Japan, December 19, 2016.

（１２） Sachiko Nishioka, Mizuki Tenjimbayashi, and Seimei Shiratori, Double porous GEL-SLIPS films with long-term anti-corrosion property, 2016 Asian Workshop on Polymer Processing, Melbourne, Australia, November 6-9, 2016.

（１３） Seimei Shiratori, Naoyuki Yokoi, Kengo Manabe, and Mizuki Tenjimbayashi, TRANSPARENT OIL/WATER SEPARATION FILTER USING POLYESTER MESH, 2016 Asian Workshop on Polymer Processing, Melbourne, Australia, November 6-9, 2016.

（１４） Kaichi Sasaki, Mizuki Tenjimbayashi, Kengo Manabe, and Seimei Shiratori, ONE STEP FORMATION OF JANUS TEXTILES AND GRADIENT FUNCTIONAL FILMS VIA SPRAY DISTANCE CONTROL OF NANOPARTICLES/POLYMER COMPOSITE, 2016 Asian Workshop on Polymer Processing, Melbourne, Australia, November 6-9, 2016.

（１５） Takeshi Matsubayashi, Mizuki Tenjimbayashi, Kengo Manabe, Masatsugu Komine, and Seimei Shiratori, SALT-TOLERANT HYDROGEL-COATED MESH WITH SUPERHYDROPHILIC/UNDERWATER SUPEROLEOPHOBIC PROPERTY FOR EFFECTIVE OIL–WATER SEPARATION, 2016 Asian Workshop on Polymer Processing, Melbourne, Australia, November 6-9, 2016.

（１６） R. Togasawa, M. Tenjimbayashi, T. Matsubayashi, T. Moriya, K. Fujimoto, and S. Shiratori, SLIPPERY SMOOTH SURFACE WITH HOT WATER REPELLENCY FABRICATED ON EPOXY RESIN SUBSTRATE, 2016 Asian Workshop on Polymer Processing, Melbourne, Australia, November 6-9, 2016

（１７） Mizuki Tenjimbayashi, Kaichi Sasaki, Jyunichiro Abe, Seimei Shiratori, A BIOLOGICALLY INSPIRED ATTACHABLE, SELF-STANDING NANOFIBRE SHEET FOR VERSATILE USE IN OIL–WATER SEPARATION, 2016 Asian Workshop on Polymer Processing, Melbourne, Australia, November 6-9, 2016.

（１８） Seimei Shiratori, Sachiko Nishioka, Kaichi Sasaki, Mizuki Tenjimbayashi, and Kosuke Tsukada, Durable Blood-Repelling Surface Coating for Medical Application, Biomaterials International 2016, Kentiing, Taiwan, October 30-November 3, 2016.

(１９) Takeshi Matsubayashi, Mizuki Tenjimbayashi, Kengo Manabe、 Masatsugu Komine, and Seimei Shiratori, One-pot Synthesis of Conductive Polymer Nanoparticles for Defrosting Heater, 9th International Conference on Fiber and Polymer Biotechnology, Osaka, Japan, September 8, 2016.

(２０) Takeshi Matsubayashi, Mizuki Tenjimbayashi, Kengo Manabe and Seimei Shiratori, One-pot Synthesis of Cyanoacrylate/PEDOT:PSS Composite Nanoparticles for Conducting Superhydrophobic Surfaces, 2015 MRS Fall Meeting & Exhibit, Boston, USA, November 29-December 4, 2015.

(２１) R. Togasawa, M. Tenjimbayashi, K. Fujimoto, T. Matsubayashi, and S. Shiratori, Slippery surface fabricated by biocompatible material with high speed water repellency and durability against hot water, 25th The Materials Research Society of Japan, Yokohama, Japan, Dec. 8-10, 2015.

(２２) J. Abe, M. Tenjimbayashi, and S. Shiratori, High Total Transparency and Scattering Nano-Fibrous-Gel-SLIPS Fabricated by Electrospinning Method, 25th The Materials Research Society of Japan, Yokohama, Japan, Dec. 8-10, 2015.

(２３) Kaichi Sasaki, Mizuki Tenjimbayashi, Kengo Manabe, and Seimei Shiratori, Flexible cotton fabrics with reversible wettability, The International Chemical Congress of Pacific Basin Societies 2015, Hawaii, USA, Dec. 17, 2015.

(２４) Takeshi Matsubayashi, Mizuki Tenjimbayashi, Kengo Manabe, and Seimei Shiratori, Novel and facile method to synthesize hollow cyanoacrylate nanoparticles, The International Chemical Congress of Pacific Basin Societies 2015, Hawaii, USA, Dec. 17, 2015.

(２５) T. Nakashima, M. Tenjimbayashi, S. Shiratori, M. Fujita, T. Kamiya, and T. Honda, Anti-fouling flat film with transparency, self-standing and flexible property, The International Chemical Congress of Pacific Basin Societies 2015, Hawaii, USA, Dec. 17, 2015.

(２６) Sachiko Nishioka, Mizuki Tenjimbayashi, and Seimei Shiratori, Anti-biofouling surface with plant oil infused porous structure, The International Chemical Congress of Pacific Basin Societies 2015, Hawaii, USA, Dec. 17, 2015.

(２７) Mizuki Tenjimbayashi, Takeshi Matsubayashi, Kengo Manabe, and Seimei Shiratori, Transparent rapidly liquid slipping smooth surface with self-healing property, The International Chemical Congress of Pacific Basin Societies 2015, Hawaii, USA, Dec. 17, 2015.

(２８) Takeshi Matsubayashi, Mizuki Tenjimbayashi, Kengo Manabe and Seimei Shiratori, One-pot Synthesis of Size-controlled Cyanoacrylate/PEDOT: PSS Composite Hollow Conductive Nanoparticles, 2015 MRS Fall Meeting & Exhibit, Boston, USA, Dec. 2, 2015.

(２９) T. Matsubayashi, M. Tenjimbayashi, S. Shiratori, Fabrication of Hollow Cyanoacrylate Nano Particles and Application to Oleophobic Surfaces, 24th The Materials Research Society of Japan, Yokohama, Japan, Dec. 11, 2014.

(３０) K. Sasaki, M. Tenjimbayashi, S. Shiratori, Single-faced superhydrophobicity and back side superhydrophilicity combination of cellulose fibers with high durability, 24th The Materials Research Society of Japan, Yokohama, Japan, Dec. 11, 2014.

(３１) M. Tenjimbayashi, H. Komatsu, M. Akamatsu, W. Nakanishi, S. Shiratori, K. Ariga, Potassium determination-system based on PVDF-HFP optode, 24th The

Materials Research Society of Japan, Yokohama, Japan, Dec. 11, 2014.

(３２) K. Sasaki, M. Tenjimbayashi, S. Shiratori, Single-faced superhydrophobicity and back side superhydrophilicity combination of cellulose fibers with high durability, 24th The Materials Research Society of Japan, Yokohama, Japan, Dec. 11, 2014.

(３３) T. Matsubayashi, M. Tenjimbayashi, S. Shiratori, Fabrication of Hollow Cyanoacrylate Nano Particles and Application to Oleophobic Surfaces, 24th The Materials Research Society of Japan, Yokohama, Japan, Dec. 11, 2014.

(３４) Mizuki Tenjimbayashi, Kouji Fujimoto, Shingo Nishizawa, Kyu-Hong Kyung, Seimei Shiratori, Fabrication of biocompatible superhydrophobic coatings with mechanical durability by one step spraying, 23rd The Materials Research Society of Japan, Yokohama, Japan, Dec. 14, 2013.

Domestic Conference

(1) Jiatu Li, Mizuki Tenjimbayashi, Yuki Tokura, Ko Matsukawa, Kenta Homma, Aya Mizutani Akimoto and Seimei Shiratori, In Situ Monitoring of Cell Adhesion on Thermally Responsive Nanofiber Coatings Using Quartz Crystal Microbalance, The 34th sensor symposium, 広島国際会議場(広島), 2017年10/31-11/02発表予定.

(2) 天神林 瑞樹, 戸賀沢 稜, 東 昌樹, 白鳥 世明, Dynamic wettability control on smooth surface for liquid manipulator and slippery coating with multi-functionality, 日本化学会 第97回春季年会, 慶應義塾大学日吉キャンパス, 2017年3月16日発表.

(3) 西岡 紗知子, 天神林 瑞樹, 白鳥世明, 二重の多孔質膜を用いた長期防汚性能を有する滑液表面, 第26回日本MRS年次大会, 横浜開港記念会館(横浜), 2016年12月20日発表.

(4) 天神林 瑞樹, 戸賀沢 稜, 白鳥 世明, π電子相互作用により撥水液体を吸着した平坦表面, 第77回応用物理学会秋季学術講演会, 朱鷺メッセ(新潟), 2016年9月16日発表.

(5) 守谷 赳夫, 天神林 瑞樹, 松林 毅, 小峰 正嗣, 吉川 亮平, 白鳥 世明, 着雪防止性能のある透明コーティングの作製及び屋外試験による検証, 第77回応用物理学会秋季学術講演会, 朱鷺メッセ(新潟), 2016年9月16日発表.

(6) 天神林 瑞樹, 佐々木 開地, 阿部 純一郎, 真部 研吾, 白鳥 世明, エレクトロスピニング法による自立型ナノファイバーの作製と油水分離膜への応用, 第65回高分子学会年次大会, 神戸国際会議場・展示場, 2016年5月26日 発表.

(7) 松林 毅, 天神林 瑞樹, 真部 研吾, 小峰 正嗣, 白鳥 世明, 導電性高分

子複合ナノ粒子による導電超撥水膜の作製および解氷ヒーターへの応用, 第65回高分子学会年次大会, 神戸国際会議場・展示場, 2016年5月26日 発表.

(8) Takeshi Matsubayashi, Mizuki Tenjimbayashi, Kengo Manabe, Masatsugu Komine, Seimei Shiratori, Electrically Conductive Superhydrophobic Films for Flexible Defrosting Heater, 第63回応用物理学会春季学術講演会, 東京工業大学 大岡山キャンパス, 2015年3月20日発表.

(9) 守谷赳夫, 小峰正嗣, 天神林 瑞樹, 真部研吾, 白鳥世明, 塩添加による滑液性表面の防霜性能向上, 第63回応用物理学会春季学術講演会, 東京工業大学 大岡山キャンパス, 2015年3月19日発表.

(10) 天神林 瑞樹, 真部 研吾, 松林 毅,守谷 赳夫, 戸賀沢 稜, 白鳥 世明, 微小液体を弾く液体保持型フラット表面, 第 76 回応用物理学会秋季学術講演会, 名古屋国際会議場, 2015年9月14日発表.

(11) 佐々木開地, 天神林瑞樹, 真部研吾, 白鳥世明, セルロース繊維への生体適合性材料による耐摩耗性片面超撥水機能, 第 62 回応用物理学会春季学術講演会, 東海大学 湘南キャンパス, 2015年3月13日発表.

(12) S. Nishioka, M. Tenjimbayashi, K. Suwabe, S. Shiratori, Slippely surface using edible oil, 24th The Materials Research Society of Japan, Yokohama, Japan, Dec. 11, 2014.

(13) T. Nishiyama, M. Tenjimbayashi, K. Suwabe, S. Shiratori, Preparation and evaluation of biomimetic transparent film using a hollow nanosilica, 24th The Materials Research Society of Japan, Yokohama, Japan, Dec. 11, 2014.

(14) T. Nakashima, M. Tenjimbayashi, S. Shiratori, Fabrication of self-standing flexible transparent slippery film by sol-gel method, 24th The Materials Research Society of Japan, Yokohama, Japan, Dec. 11, 2014.

(15) 西岡紗知子, 天神林瑞樹, 諏訪部憲, 白鳥世明, 植物油を用いたフッ素フリー滑液面, 第 75 回応用物理学会秋季学術講演会, 北海道大学 札幌キャンパス, 2014年9月19日発表.

(16) 中島太一, 天神林瑞樹, 白鳥世明, 藤田将人, 神谷武志, 本田常俊, Sol-gel法による自立型フレキシブル透明滑水滑油膜の作製, 第75回応用物理学会秋季学術講演会, 北海道大学 札幌キャンパス, 2014年9月18日発表.

(17) 松林毅, 天神林瑞樹, 白鳥世明, 中空シアノアクリレートナノ粒子を用いた半透明高撥油膜の作製, 第75回応用物理学会秋季学術講演会, 北海道大学 札幌キャンパス, 2014年9月17日発表.

(18) 西澤真吾, 天神林瑞樹, 白鳥世明, スキージ法による透明超撥水膜の作

製, 第 61 回応用物理学会春季学術講演会, 青山学院大学 相模原キャンパス, 2014 年 3 月 18 日発表.

(１９) Atthaporn Ariyarit, 天神林瑞樹, 白鳥世明, Fabrication and Evaluation of Transparent Conductive Oxide CuAlO thin films, 第 61 回応用物理学会春季学術講演会, 青山学院大学 相模原キャンパス, 2014 年 3 月 18 日発表.

(２０) 天神林 瑞樹, 諏訪部憲, 白鳥 世明, Fluorine-free slippery surfaces with omniphobicity, 第 61 回応用物理学会春季学術講演会, 青山学院大学 相模原キャンパス, 2014 年 3 月 20 日発表.

(２１) 天神林 瑞樹, 藤本 幸司, 西澤 真吾, 慶 奎弘, 白鳥 世明, Fabrication of superhydrophobic, highly oleophobic film with highly durable function by one step spraying using SiO2 nanoparticle, 第 74 回応用物理学会秋季学術講演会, 同志社大学 京田辺キャンパス, 2013 年 9 月 17 日発表.

Patents

(１) 繊維製品、および、被膜付き物品 白鳥 世明, 天神林 瑞樹, 佐々木開地, 松川 義彦 (特願 2016-097813, H28. 5. 16)

(２) 滑液膜、その製造方法、及びそれにより被覆された表面を有する物品 白鳥 世明, 天神林 瑞樹, 戸賀沢稜 (特願 2015-231603, H27. 11. 27).

Awards & Scholarships

(１) R. Togasawa, M. Tenjimbayashi, T. Matsubayashi, T. Moriya, K. Fujimoto, S. Shiratori, 第 26 回日本 MRS 年次大会奨励賞受賞, 日本 MRS, 2016 年 12 月 20 日

(２) Takeshi Matsubayashi, Mizuki Tenjimbayashi, Kengo Manabe、Masatsugu Komine, and Seimei Shiratori, Student Poster Award, 繊維学会, 2016 年 9 月 8 日

(３) 松林 毅, 天神林 瑞樹, 真部 研吾, 小峰 正嗣, 白鳥 世明, 優秀ポスター賞, 高分子学会, 2016 年 5 月 26 日

(４) 天神林 瑞樹, 2015 年度機能創造賞, 慶應義塾大学理工学研究科総合デザイン工学専攻マテリアルデザイン科学専修, 2016 年 3 月 28 日受賞.

(５) 天神林 瑞樹, 日本学術振興会特別研究員 DC1 採用（2016 年 4 月~）

(６) 天神林 瑞樹, 2015 年度藤原奨学基金奨学生採用 2016 年 3 月 28 日.

(７) 天神林 瑞樹, 2015 年度 KLL 前期博士課程研究助成金 採用

(8)　天神林 瑞樹, 慶應義塾大学大学院奨学金給付対象者選出（2015年8月支給

(9)　天神林 瑞樹, 第15回物理情報工学科主任賞, 慶應義塾大学理工学部物理情報工学科 主任 足立修一, 2014年3月24日受賞.

（１０）　慶應義塾大学前期博士課程早期修了(2015年9月）

（１１）　慶應義塾大学後期博士課程早期修了(2017年8月）

Technical Books

(1)　天神林 瑞樹, 守谷 赳夫, 白鳥 世明, 表面技術(2016年9号）第67巻, No. 9「小特集：はっ水，はつ油，親水・親油表 面処理」題　目：オムニフォビシティ滑液表面, 461-466

(2)　天神林 瑞樹, 白鳥 世明, 「超撥水・超撥油・滑液性表面の技術」,サイエンス＆テクノロジー株式会社, 第3章 第1節「交互積層法による超撥水・超撥油表面」, 第4章　第2節　「オムニフォビシティ滑液性表面の作製」